DESIGNING REACTIVE METAL NANOLAMINATE FUELS FOR BIOAGENT DEFEAT

by
Kyle R. Overdeep

A dissertation submitted to Johns Hopkins University in conformity with the requirements for the degree of Doctor of Philosophy

Baltimore, Maryland

August, 2016

Abstract

This research focuses on developing reactive metal nanolaminates to be used as fuels in explosive formulations to destroy anthrax. The nanolaminates contain alternating nanometer-scale layers of metals that can mix exothermically to form intermetallic compounds, bringing the composite to high temperatures where combustion is enabled. The resulting combustion energy aides directly in the thermal destruction of spores, but also provides energy to decompose HIO3 particles into biocidal iodine gas for chemical destruction of spores as well.

The principal metric for assessing these fuels is their total heat generation, for which two bomb calorimeters were designed to address the unique ignition and heating concerns of reactive metallic foils and particles. The merit of adding Mg to a base Al/Zr layered structure is investigated by comparing the behavior of sputter-deposited foils with varying Mg contents. The conclusion is that Mg vaporizes during the reaction and increases the vacancy concentration within the bulk, allowing for improved combustion. In-situ XRD of combusting Al:Zr foils demonstrates a transition from interface-controlled oxidation to diffusion-limited oxidation that coincides with combustion terminating prematurely. A result of this mechanism is that combustion efficiency depends upon the volume fraction of the surface oxide, which is a function of foil thickness. Foils with Mg, however, do not exhibit this dependence, supporting the argument that the vaporization of Mg enhances diffusion, allowing for a greater extent of oxidation and nitridation within the central regions of the foil.

The final application requires that the material be in particulate form, and so reactive particles were sputtered as well as ball-milled. These particles perform better than the current state-of-the-art in explosive detonation tests performed at the Indian Head Naval Surface Warfare Center.

Readers:

Timothy P. Weihs (Advisor)

Todd C. Hufnagel

Preface & Acknowledgments

The contents of this dissertation would not have been possible without the support of many people, including undergraduate researchers, other graduate students, post docs, professors, staff, and previous research group members.

A good deal of the data collection and analysis presented was performed by my undergraduate students. Howie Joress spearheaded the in-situ XRD experiments, travelling to CHESS for the tests and preparing samples for the related microprobe and TEM work. Paul Marcello studied the ignition temperatures of various foil compositions across a wide range of bilayers, which went into the model developed by Dr. Manav Vohra. Travis Schmauss, Atman Panigrahi, Madeline Mueller, and Minzi Keem all performed many bomb calorimetry runs that went into the studies focused on the heat produced during the combustion of foils as a function of composition, geometry, and environment. Travis also prepared foil cross-sections for SEM measurements and analysis, and then continued on to a senior research project investigating the cause of microexplosions observed for reacting foils and particles. Madeline proceeded with bomb calorimetry of reactive particles, both sputter deposited and ball milled. David Gibbins was helpful in fabricating the ball milled samples.

The other graduate students in the group also offered a lot of support, most notably Mike Grapes for assistance with the sputter chamber and developing the software used for the bomb calorimeters, and Elliot Wainwright for his continued work on the DTRA project fabricating and characterizing ball milled materials. David Allen, a student of

Nick Glumac at the University of Illinois at Urbana Champaign, ran spectroscopy when we were first looking into the effects of including Mg in our composites, and both David and Dr. Glumac were very helpful in understanding the results. Rohit Jiji Jacob, a student of Michael Zachariah at the University of Maryland, offered his resources and effort to help calibrate the two-color pyrometer I built.

The two postdocs working on the DTRA project were very helpful. Dr. Shashank Vummidi Lakshman has done a lot of work ball milling new materials, and developing analysis codes and new instrumentation for future work on these nanocomposite fuels. Dr. Xuesong Jiang has also contributed greatly, investigating the biocidal capabilities of the materials we have developed. Dr. Lan Zhao ran the in-situ XRD experiments, with the assistance of Karsten Woll, Felicitee Curtis, Jennifer Kirkoff, Mike Grapes, and Howie Joress, as previously mentioned. Lan also began the analysis of the results, under the guidance of Dr. Todd Hufnagel, who has been essential in understanding and interpreting the diffraction data from those experiments.

The co-PI's on the DTRA project, Dr. Hai-quan Mao, and Dr. Omar Knio, provided crucial support for all the work that I have done. They have followed my research over the years, providing guidance and feedback every step of the way. Dr. Mao led the effort of understanding the biocidal capabilities of our materials, and Dr. Knio led the computational modeling of the reactions occurring in Al:Zr multilayers.

My gratitude also goes to Ken Livi, an excellent microscoptist who is credited with all of the microprobe and TEM work I have published. Dr. Douglas Meier of NIST was also helpful in offering his facilities and operating the instrument for the microprobe work comparing foils of varying compositions. I also had the pleasure of working with Francis Cook and Mike Franckowiak, who were exceedingly helpful in machining the bomb calorimeters and providing input regarding their designs. James J. Haycraft was also very helpful in building the pyrometer, answering countless ignorant emails throughout the construction process and providing the design and component list it was based off of.

This work would also not have been possible without the previous work of my predecessors in the Weihs lab. Greg Fritz developed the methodology for sputtering particles, measuring ignition temperatures, and igniting foils uniformly by resistive heating. Sara Barron, a former post-doc of the group, started the DTRA project by fabricating Al:Zr and Al-8Mg:Zr foils and provided training on velocity and pyrometry measurements when I first joined the lab.

Finally, I am hugely indebted to my advisor, Dr. Tim Weihs, who has been an endless source of encouragement and advice. He has always prioritized the work of his graduate students, and has made my time in the Weihs Lab an enjoyable growing experience, both professionally and personally.

This work is funded by the Defense Threat Reduction Agency (DTRA), grant HDTRAA1-11-1-0063 and HDTRA1-15-0006.

Table of Contents

List of Tables

List of Figures

1 Introduction

This body of research focuses on fabricating reactive nanolaminate foils and particles and characterizing their ignition and combustion. Conventional explosives do not have a particularly high energy density, especially in comparison to metals. TNT has a maximum combustion enthalpy of 14.5 kJ/g; less than half of the 31.0 kJ/g for aluminum [1]. Metal fuels are therefore of great interest because they have the potential to increase the energy density of explosives and propellants by 2-3×, which will enhance their effectiveness in any application, most notably in munitions for national security, but also diverse applications like mining, excavation, and rocket propulsion [2]. Metal fuel particles, especially aluminum, have therefore been used as additives to aid in combustion for decades [3–5].

The goal of this work was to design a metal fuel that will improve the heat output and extend the burn durations of explosive formulations used for bioagent defeat. Spores such as anthrax can be destroyed via thermal kill from the high temperature fireball [6–9], and spores not directly exposed to the heat can be destroyed by chemical deactivation using biocidal iodine gas [10–12]. The gas would be generated in the explosion by the thermal decomposition of an iodine precursor such as HIO_3, which also functions as an oxidizer in the formulation.

Nanolaminate metal fuels contain alternating layers of different metals, in this case aluminum and zirconium, which have a negative heat of mixing. Each bilayer is on the order of 90 nm thick, and the large interfacial area between these two metals allows the layers to intermix exothermically and form Al/Zr intermetallics with a small input energy. The sensitivity of the intermetallic formation reaction is a function of the composition and the reactant spacing (bilayer thickness) [13,14]. The heat generated within an ignition zone is enough to initiate rapid mixing in the surrounding layers, and so the reaction will self-propagate throughout the entire system, bringing the entire body to high temperature (≈1800 K) where combustion can occur, as shown schematically in **Figure 1.1**. Data for ignition temperature and propagation velocity as functions of bilayer thickness for two foil compositions of interest are provided in **Appendix 8.1**.

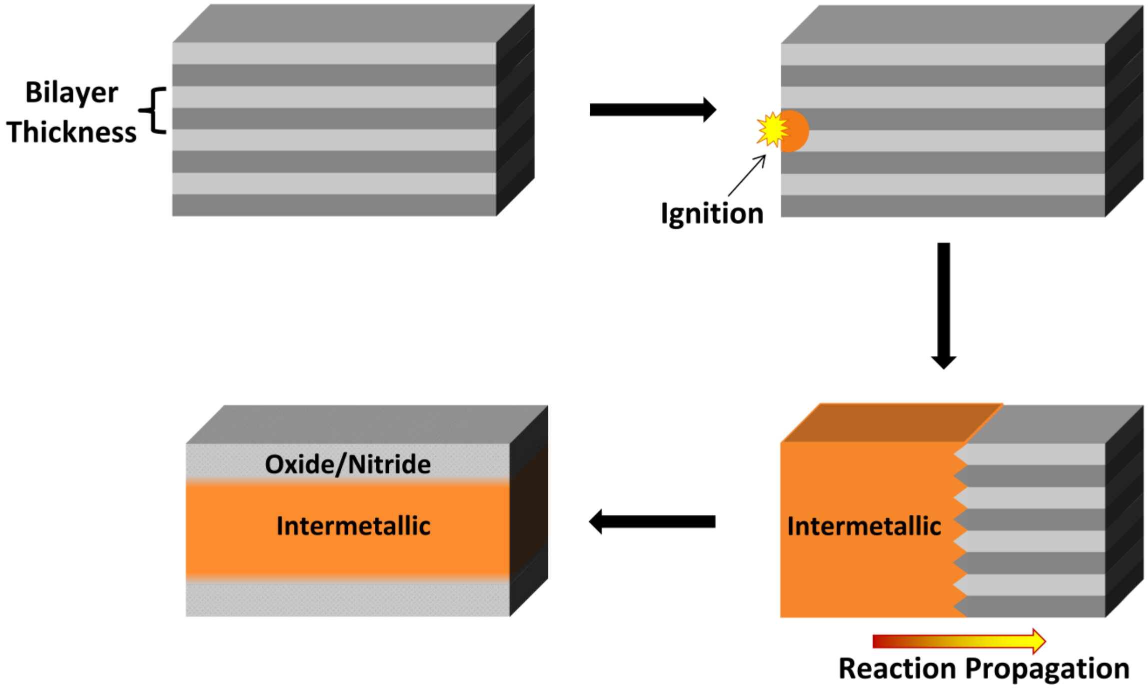

Figure 1.1: Rapid, self-propagating formation reactions occur in metallic multilayer foils after a small energy input, and can be followed by slower oxidation and/or nitridation in air. Only a small number of layers are shown; in reality, foils contain hundreds of layers.

With an effective choice of metals, the oxide and nitride formation reactions can release significantly more heat than the intermetallic formation reactions alone [15–17].

Al and Zr are used because not only do they form intermetallics with high heats of formation, but each has favorable combustion characteristics. This idea has been applied to many systems, though, with different microstructures and chemistries [1,13,18], including core-shell particles [19–23], powder compacts [24–29], mechanically activated foils and powders [30–34], and vapor-deposited laminate foils [14,18,35–42].

In this research, we first sputter-deposited macro-scale foils because the foils are highly regular and can be measured and observed easily, which allows for a more robust scientific study. Using these foils, we investigated the effect of including Mg in the Al layers in the Al/Zr multilayer structure [43]. The total heat output was measured using a highly specialized, self-designed bomb calorimeter [44] with an internal environment of 1 atm of air. We found that with a small amount of Mg, the heat of combustion improves by ≈50% in air in comparison to foils without Mg. In order to explain these findings, high-speed videography and spectroscopy were performed, and showed that Mg was vaporizing from the foils, which led to further expulsion of molten particles of all three metals. TEM-EELS showed that all ejected material oxidized completely, but we proposed that the main improvement in heat production was the result of the vaporizing Mg leading to a higher concentration of vacancies within the bulk of the foils. The vacancies improved the diffusion of oxygen and nitrogen into the unreacted centers of the foils.

In order to better understand what limits combustion in Al:Zr foils, we performed an in-situ XRD study of combusting Al:Zr foils at the Cornell High Energy Synchrotron Source (CHESS) while simultaneously measuring the temperature via pyrometry [45]. This experiment showed that while Al:Zr burned, the orthorhombic ZrO_2 phase grew linearly with time, which is evidence of interface-controlled growth. At approximately 1.2 s after ignition, the growth of the oxide began to decline, deviating from linearity as it switched to diffusion-controlled growth. The switch to diffusion-limited growth coincided with an abrupt drop in temperature and the premature termination of combustion.

A corollary of this conclusion is that the combustion energy for these foils is likely to depend upon the volume fraction of this surface oxide layer, and therefore might also depend upon the foil thickness. This hypothesis was tested by performing a study in which the heats of combustion were measured for foils of varying thicknesses [46]. We found that combustion efficiency decreased significantly for Al:Zr foils as thickness increased, but Al-8Mg:Zr foils had a nearly constant combustion efficiency for the range of thicknesses studied (10-60 μm). SEM-EDS measurements across the foil cross-sections showed that for Al:Zr foils, a distinct oxide layer forms on the external surfaces of the foils, with low levels of oxygen and nitrogen towards the foil centers. For Al-8Mg:Zr foils though, there was no dependence on foil thickness because the amount of heat generated by the gaseous reactants forming solid solutions in the central regions were able to counter the trend of decreasing heat contributions from the external oxide layers as thickness increases. This is enabled by the increased diffusion rate for Mg-containing systems leading to higher levels of oxygen and nitrogen throughout the bulk of the foil.

After establishing a firm understanding of how combustion progresses for the model foil systems, we progressed to fabricating nanolaminate particles, which could actually be used in explosive formulations. Particles were fabricated by sputtering onto nylon mesh substrates and removing the deposited material mechanically. Although particles had less regular structures than the foils had, the level of control was still high. Particles were made with the same compositions that were used for foils, and each performed significantly better than its foil counterpart. The sputtered particles were assessed on a small scale (mg) at Johns Hopkins by bomb calorimetry, spectroscopy, and high-speed videography, with and without the HIO_3 oxidizer. Larger scale tests (g) were performed at Indian Head Naval Surface Warfare Center (IH-NSWC) where mixtures of nanolaminate fuel particles and HIO_3 oxidizer were detonated with an explosive charge in an open room, as well as in a closed chamber with spore samples. The large-scale tests were performed by Dr. Demitrios Stamatis and Dr. James Lightstone. Our materials performed better than the current benchmark fuel, nano-Al.

Given the success of our materials, we have progressed to fabricating nanolaminate particles by ball milling, which is a less controlled process, but has the potential for scaling up and allowing our materials to be mass-produced for the final application. Preliminary testing shows that the ball milled materials actually perform better, due to having a wider particle size distribution than that of sputtered foils.

Using the fabricated material, small-scale biocidal tests were performed as a collaborative effort at Johns Hopkins University with Dr. Xuesong Jiang and Dr. Hai-Quan Mao [47]. We also collaborated with Dr. Manav Vohra and Dr. Omar Knio of Duke University [48] to develop a computational model of the ignition and combustion of Al:Zr nanocomposite foils.

2 Design and Functionality of a High-Sensitivity Bomb Calorimeter Specialized for Reactive Metallic Foils

2.1 Motivation for a Specialized Bomb Calorimeter

Our goal is to design high energy density metallic fuels with tailored combustion properties, such as temperature, combustion duration, and most notably, heat production. In order to understand how to maximize the heat produced during the combustion of these materials, it was necessary to characterize their reactions using bomb calorimetry. We therefore designed and built two bomb calorimeters, one for particles, and one for foils. Typical bomb calorimeters are designed to measure reactions of particles, and so this chapter will focus solely on the more unique and specialized foil calorimeter. The particle calorimeter will be described briefly in the context of the experimental setup for the particle study presented in **Chapter 6**.

Using the foil bomb calorimeter, we compared the heats of combustion for foils of varying chemistries and geometries when reacted in different environments including air, oxygen, argon, and nitrogen; all at atmospheric pressure. These conditions are abnormal for bomb calorimetry and prevent complete combustion of the sample, but were necessary for our study, whose purpose was not to obtain the total energy of combustion for the foils. The purpose was rather to gain an understanding of how the diffusion-limited kinetics of combustion can be overcome by tuning the foil's chemistry or geometry, so as to maximize the extent of combustion in these conditions. Pressurizing the calorimeter with oxygen to obtain complete combustion would therefore defeat the purpose of the experiments.

Our reactive foils were very low in mass, about 100 mg for a foil of typical dimensions (50 mm x 15 mm x 40 μm), but were as small as 4 mg for the smallest samples we worked with. The sample mass was limited because stacking foils or fabricating thicker foils would change the combustion properties, which are geometry-dependent as will be discussed in **Chapter 5**. Consequently, because we were limited to small samples and incomplete combustion, the bomb calorimeter used for this study had to be highly sensitive. Our least energetic reactions, specifically those performed in argon, released very small amounts of energy, down to tens of Joules.

Commercial bomb calorimeters, such as the "semi-micro" calorimeter manufactured by Parr Instruments, were designed to react samples on the order of grams and measure kilojoules of heat [49]. Others have made micro-bomb calorimeters in order to measure samples in the milligram range and have been very successful [50–60]. Although all of these were designed to react milligrams of material, milligrams of our reactive metal foils (with heats as low as 0.7 kJ g^{-1}) [43] are not equivalent to milligrams of benzoic acid (≈26.4 kJ g^{-1}) or salicylic acid (≈21.9 kJ g^{-1}) [56], which are commonly used standards in calorimetry. Furthermore, because these microbombs are all designed to be pressurized with oxygen and burn powders or pellets of organic compounds, even an instrument such as the one presented in reference [50], which has the sensitivity required for our application, cannot be used for reactive foils. We therefore built a bomb calorimeter specifically for reacting our metallic foils at atmospheric pressure. The design may be of interest to both the reactive material community and the calorimetry community because it is a unique, highly sensitive micro-bomb calorimeter that is relatively inexpensive to fabricate, robust, easy to use, and has a short setup and run time.

2.2 Emphasis on Instrument Sensitivity

Combustion calorimeters are generally designed to maximize accuracy, precision, and sensitivity. Accuracy in particular is critical for studies in pharmaceuticals or energy sources like oil and natural gas. One study states that a 0.1% error in the calorimetric measurement of natural gas caused a loss of $83 million in the US in the late 1980's, and similar losses for other countries [61]. Sensitivity and precision are also very important for studies of limited sample mass, usually in the field of organic synthesis, in which only milligrams of each sample exist. The calorimeter must therefore be sensitive enough to measure heat evolved during the combustion of small samples, and must also be precise enough that each sample does not require 5-10 runs to obtain an accurate result.

Our calorimeter is quite different in principle because extreme precision and accuracy are not necessary. High-precision instruments have been developed, such as in that of [50], which boasts a standard deviation of 0.0035% using calibrations with benzoic acid, but heat production from our samples deviates by up to 6%, as will be shown in **Chapter 3**, and many runs must be averaged to gain representative data, regardless of instrument precision. Similarly, operation with error in the range of 0.05- 0.1% is possible even with typical commercial instruments [62], but we are performing a comparative study, and accuracy within a few percent is acceptable in the reactive materials community. The Al:Ni foils we use to calibrate the calorimeter also have ≈2% uncertainty in their heat production [63], which is quite large compared to that of a benzoic acid standard. Therefore, the level of accuracy and precision desired for most applications is neither useful for our experiments, nor attainable using our calibration material.

Sensitivity, however, is a major concern. Our foils are fabricated by sputter-deposition, which is a thin-film fabrication technique that inherently produces very low-mass samples, ranging from 5-200 mg, because each foil sample is only tens of microns thick. Heat production from our foil samples is also size dependent, and so we cannot simply fabricate thicker foils or stack the thinner ones together. Consequently, a bomb calorimeter for reactive metal foils must be extremely sensitive, but the in-depth corrections and methods used for the extreme accuracy and precision that are essential to many applications are rendered unnecessary. Most of the corrections do not even apply to these materials, since reacting metals do not generate acids, water, or significant pressure, and are ignited with a low-energy spark rather than a heated filament and fuse.

2.3 Design of the Foil Bomb Calorimeter

The calorimeter is comprised of a vacuum flask containing silicone oil, with the specialized foil combustion bomb submerged within. An expanded view of this is shown in **Figure 2.1a**. The calorimeter temperature is measured in the oil, which is constantly stirred with a magnetic stir-bar. The reaction cylinder is affixed to the calorimeter’s lid so that the submersion depth remains consistent and so that the bomb is not in contact with any part of the jacket, nor in the way of the stir bar at the bottom.

The bomb itself has two primary components: a titanium frame that holds and ignites the foil samples (**Figure 2.1b**), and a reaction cylinder with an o-ring seal that the frame screws into (**Figure 2.1c**). The reaction cylinder has a gas inlet valve so that the environment can be controlled, allowing us to perform experiments in air, argon, nitrogen, oxygen, or low vacuum. Generally, standard bomb calorimetry conditions are 30 atm of pure oxygen in order to measure complete combustion [64], but we are more concerned with how foils will burn in our final application in a mixture of gases at 1 atm. All experiments and calibrations were therefore performed at this approximate pressure.

2.3.1 Maximizing Instrument Sensitivity

In order to make quality measurements from small quantities of energy, it is very important to minimize the calorimeter's heat capacity. We accomplished this by limiting the mass and by selecting materials with lower heat capacities. The largest thermal mass in the system is the liquid bath, and so to reduce this significantly, we used a low heat capacity, low viscosity, non-volatile silicone oil (Sigma-Aldrich, CAS# 63148-62-9) rather than water. The viscosity is listed as $5\,\mathrm{mm}^2\ \mathrm{s}^{-1}$ with a vapor pressure $<670\,\mathrm{Pa}$, both at 25°C. The literature value for the specific heat capacity of this oil is $1.59\,\mathrm{J\ g^{-1}K^{-1}}$ [65] as opposed to that of water which is $4.18\,\mathrm{J\ g^{-1}K^{-1}}$ [66]. The volumetric heat capacity is more relevant than the specific heat capacity, though, because the quantity of liquid used is volume based, as the volume required to submerge the bomb is the determining factor regardless of the associated mass. Using the density for each substance, the volumetric heat capacity of the oil was calculated to be 65% lower than that of water, which is a significant improvement. The mass of the bath is measured before each run and adjusted to be consistent with the quantity used in the calibration to within 1/10th of a gram. The minimum volume of oil required to submerge the bomb (≈100 mL) was used.

A hazard of using silicone oil rather than water is that it is flammable. This should not be a significant risk considering the reaction is well contained within the bomb. The silicone oil is much safer than alternative low heat capacity liquids that have been used

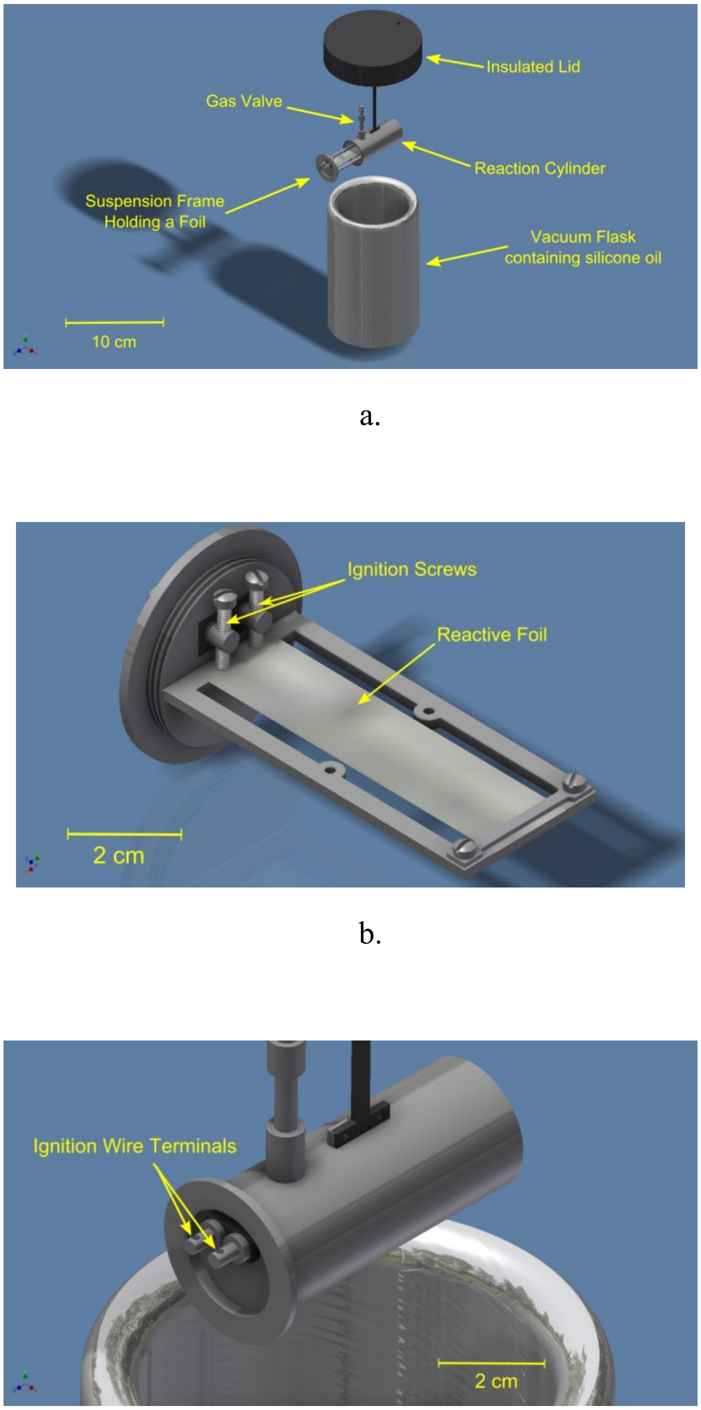

a.

b.

c.

Figure 2.1: Calorimeter components and assembly. (a) Expanded view of the calorimeter assembly, showing the suspension frame being inserted into the reaction cylinder. (b) The foil suspension frame, including the spark-ignition system. (c) The closed reaction chamber, in which the frame is sealed inside the cylinder. The two visible pins act as electrodes used for ignition.

for bomb calorimetry in the past, like carbon tetrachloride [67], which is highly toxic [68].

The next largest thermal mass in the calorimeter is that of the bomb, and so this was minimized by designing it to be as small as possible, and by using Grade 2 titanium for all metal components. The volumetric heat capacity of titanium is lower than that of steel, 2.3 kJ $L^{-1}K^{-1}$ [69] as opposed 3.8 kJ $L^{-1}K^{-1}$ [70], and titanium also offers the benefit of iodine resistance [71], which will be helpful for our particular application. Again, volumetric heat capacity is more relevant than specific heat capacity because strength and toughness depend on radius of the cylinder and wall thickness, rather than mass. The cylinder wall and the frame are only 1.5 mm thick and the shape of the bomb was designed to be as small as possible while accommodating the atypical geometry of foil samples, in order to maximize sample mass while minimizing bomb mass. Despite the relatively thin walls, rupturing is not a concern because as previously mentioned, we are interested in experiments performed at atmospheric pressure, and metals do not generate significant pressure spikes during combustion. As a result, the bomb's pressure limit is not a concern, and was calculated to be many times greater than pressures we expect.

Sensitivity also depends upon the thermal isolation in the system. Laboratory temperature fluctuations are significant when measuring very small ΔT values, and can be visible as background noise and straying baselines during runs if not controlled. These effects were significantly reduced by containing the silicone oil bath in a 150 mL vacuum flask, custom made by Pope Scientific Inc. of Saukville, WI. The flask is sealed by a Delrin lid with an inch of foam insulation, and sits in a box also constructed from foam insulation. Thermal isolation was improved further by replacing an impeller, as is typically used, with a magnetic stir-bar, which removes a source of conduction out of the system because the stir-bar is entirely contained within the oil, as opposed to an impeller where the metal shaft extends from the liquid to the environment. The stir bar also has a low heat capacity because of its small size (1.5 g) and contributes a low energy input from stirring ($<0.001\text{K min}^{-1}$).

One final determinant in instrument sensitivity is the resolution of the temperature sensor. For this, we use an ultra-precise PT100 4-wire RTD sensor with 1/10 DIN accuracy, custom made by Omega Engineering, Inc. in Stamford, CT, and calibrated for a range from 0° to 100°C. Two temperature measurements are recorded every second, acquired with a Measurement Computing USB-TEMP data acquisition device, and are plotted and recorded on the associated TracerDAQ software.

2.3.2 Minimizing Contact Area

One very important feature of the specialized bomb is that it suspends the foils, minimizing the contact area between the foil and the bomb. This is very important because the metal bomb is a very effective heat sink, and will draw energy away from the reaction during heating, thereby reducing the extent of reaction. Furthermore, most of the heat from these reactive foils is generated by oxidation and nitridation, which depend upon the ability of oxygen and nitrogen to diffuse through the foil's exposed surfaces. We therefore affix the foil to its ignition frame by clamping only a few millimeters at both ends of the foil, as shown in **Figure 2.1b**, which is sufficient to hold the sample rigidly in place with minimal contact.

2.3.3 Ignition

Many commercial bomb calorimeters achieve ignition by melting a filament, which then drips onto the sample at the bottom of the bomb, or by lighting a fuse which then burns. Resistively heating a filament to its melting point or burning a fuse would input a large amount of energy that is likely to be on the scale of the reactions that we are trying to measure. These ignition systems are also inconsistent with our other tests, like pyrometry and propagation velocity experiments, in which foils are always spark-ignited to avoid preheating. Therefore, we designed this system to ignite foils with a small electric spark from two electrodes (**Figure 2.1b**) connected to a DC power supply (MPJA model 14602PS) with a potential of ≈20 V.

While loading the sample, the electrodes, one flat and one pointed, are lowered towards the foil while measuring the resistance between them. The flat electrode is pressed against the foil for good electrical contact and the pointed electrode is lowered until the resistance between the electrodes is in the range of 5-50 Ω. This ensures reliable ignition from a spark because if the resistance is too low the electricity will conduct through the metal foil without igniting, and conversely, if the resistance is too high the circuit will effectively be open and unable to produce a spark. The pointed electrode maximizes current density at its tip for more localized heating and thereby increases the reliability of ignition.

2.4 Calibration

Benzoic acid is almost always used as the standard for calibration, and there are accepted methods for using it to calibrate the instrument and calculate its energy equivalent [72]. Benzoic acid is used because its heat of combustion is extremely well-known, and because typical combustion bomb calorimeters are designed to measure heats from similar organic substances. Our calorimeter, however, is specifically designed to measure reactions of metallic foils and so it must be calibrated with such a foil. We used 80 μm Al:Ni multilayer foils purchased from Indium Corporation (Clinton, NY) that did not contain an outer braze layer. This chemistry of reactive foil was specifically chosen because it has been studied the most extensively [36,38,63,73–77], and unlike many other multilayer foils, the complete intermetallic formation reaction occurs below 725°C, which is the limit for power-compensated Differential Scanning Calorimetry measurements. Therefore, the complete heat of the intermetallic formation reaction can be measured in a DSC and used as the known heat input for calibration reactions in the bomb calorimeter. The DSC was calibrated using well established heats of phase transformations, specifically the melting of indium, tin, and zinc. The Al:Ni foils were reacted in argon in both the DSC and the bomb calorimeter to ensure that the intermetallic formation reaction proceeded without oxidation.

Results from DSC tests, performed at 40 $K\ min^{-1}$ in a Perkin Elmer Pyris 1, are presented in **Figure 2.2a**, and show that the $\Delta H_{intermetallic}$ for Al:Ni is -1132 $J\ g^{-1}$ ±1.3%. This is a much higher uncertainty than is found for pure benzoic acid, but is acceptable for calibrating this calorimeter because it is still much smaller than the uncertainty stemming from variability of combustion properties in the experimental samples. XRD results for samples reacted in each instrument are presented in **Figure 2.2b**, showing that the same end products are formed, so we can be confident that heat produced in both instruments are equal because both result in only the AlNi intermetallic. With this method, the energy equivalent of the calorimeter was found to be 279 ±6 J K^{-1} based on eleven calibration runs.

The electrical power used for spark ignition is included in the calibration. It was measured and found to be well within the uncertainty of the measurements; only 80 mJ, which is roughly 0.02% of the heat measured from a typical foil (≈350 J). The energy is small enough to not be of concern, and consistent enough for each run to be included in the calibration rather than corrected for separately.

2.5 Data Analysis

The calorimetry community has developed various methodologies for calculating ΔT as accurately as possible, accounting for temperature drifts that may occur [78]. Our ΔT calculation is a simplified version of the extrapolation method, and we have developed a simple program in LabView to perform the analysis. The user is able to select ranges in the temperature plot corresponding to the pre- and post-reaction baselines. Each experiment lasts for about 6 minutes total: 2 minutes pre-reaction to acquire a baseline temperature, 2 minutes of temperature equilibration after the reaction takes place, and 2 minutes at the end to acquire a final baseline. This was increased for larger or more energetic samples to allow for greater equilibration time. Exponential fits are found for the initial and final baselines, and both are then extrapolated to the midpoint of the rising curve, defined by the user as the point where the integrated areas to each side are approximately equal (**Figure 2.3**). The temperature difference between the extrapolated curves at this point is ΔT for the reaction, accounting for drifts from energy gains from stirring and losses from imperfect thermal isolation. The energy input from stirring was

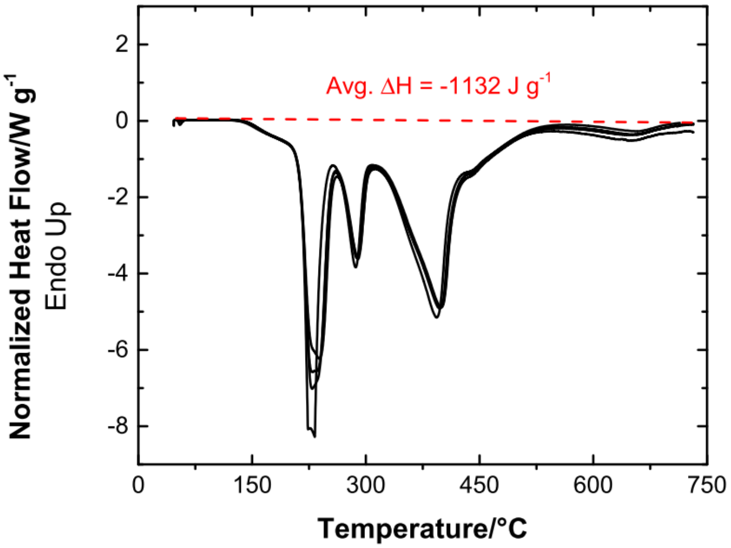

a.

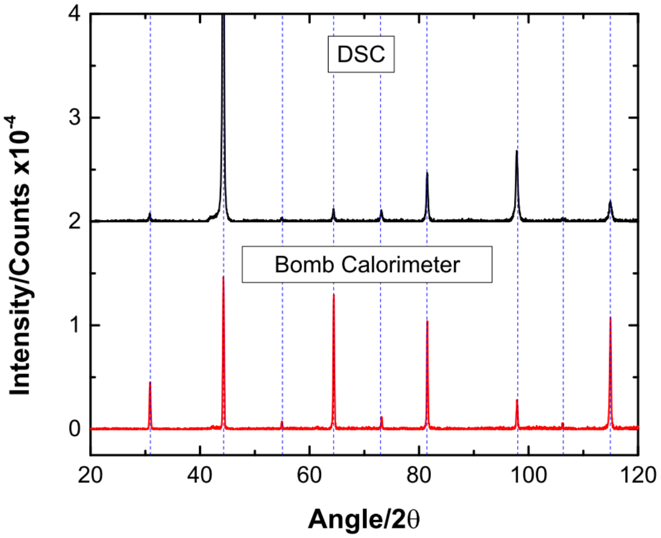

b.

Figure 2.2: (a) A series of four Al:Ni nanocomposite samples performed in the DSC to show repeatability. (b) A comparison of XRD diffraction patterns from Al:Ni foils reacted in the DSC and bomb calorimeter, to show that the same end-products are being formed in each instrument. The vertical lines indicate angles of diffraction peaks for the compound AlNi, the desired end product of the reaction. The differences in peak intensities indicate that the foils reacted in the DSC have more crystallographic texture than those reacted rapidly in the bomb. Such texture, though, should not impact the measured heats of reaction.

found to be very small, on the order of 10^{-4} K min^{-1}, as was thermal leakage, on the order of 10^{-5} K min^{-1}.

Typical results and analysis for the combustion of a reactive foil in air are shown in **Figure 2.3**. This particular sample is an Al-8Mg:Zr foil that is 59 µm thick and has a mass of 145.130 mg. Upon ignition at t=2 minutes, we see a sharp increase in temperature of nearly 1.5 K, which is very large compared to the <.01 K previously measured for the same foil using a commercial "micro-calorimeter". A sharper and larger magnitude increase is seen for samples performed in pure oxygen.

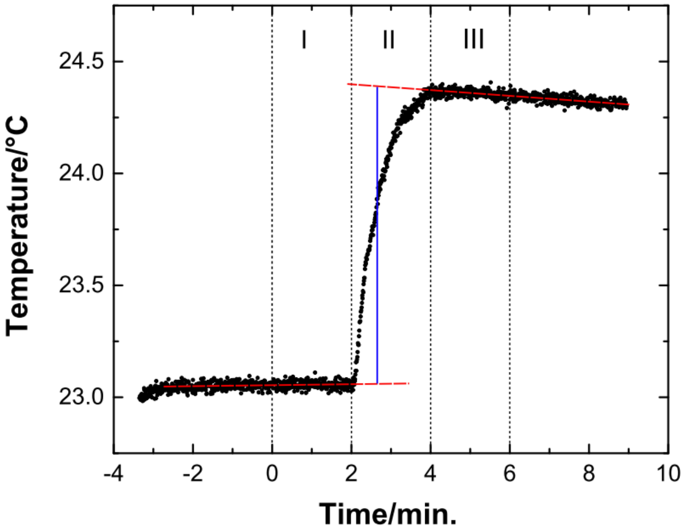

Figure 2.3: Calorimeter temperature as a function of time for a typical run. Dashed vertical lines separate the intial baseline (I), equilibration period (II), and the final baseline (III). Red lines show exponential fits for the initial and final baselines, and the blue line shows the time at which ΔT is calculated.

Also, because these metallic reactions do not produce water or acid, and do not cause significant pressure increases, typical corrections, such as the Washburn corrections, do not apply to this system. Such corrections include those for heating a filament, burning a fuse, the generation of water or acid, and pressure buildup [64,78]. Factors such as differences in sample heat capacity, which is corrected for in many analyses, are negligible in this case and can be ignored.

2.6 Functional Sensitivity

To determine the sensitivity limit of the calorimeter, we performed electrical input experiments by applying a current pulse through a filament connecting the two electrodes, with no foil. The input energy was calculated using measurements of the current and voltage applied to the filament for a given time. **Figure 2.4** shows results for decreasing input energy to sequentially lower values and measuring the error for each by comparing electrical input to the heat calculated from temperature rise. The standard deviation becomes quite large when the input is less than ≈20 J and so we consider this the sensitivity limit to gain useful data for foils within a 2% uncertainty, which is approximately equal to the standard deviation of the calibration. The smallest pulse tested, about 4 J, was still accurate to within 5% using the average of five runs, despite resulting in a temperature change of only ≈0.01 K. Such a rise is barely discernible above the level of the background noise of ±0.025 K. This suggests that despite the poor precision, the accuracy of the mean value is still in an acceptable range, considering that the experimental foils exhibit heat generation with standard deviations up to 6% due to sample variability. Note that the heats applied to demonstrate the sensitivity limits of the instrument are much smaller than the heats measured in typical experiments, which are on the order of 350 J. Thus, most measurements are well above the sensitivity limit of the instrument.

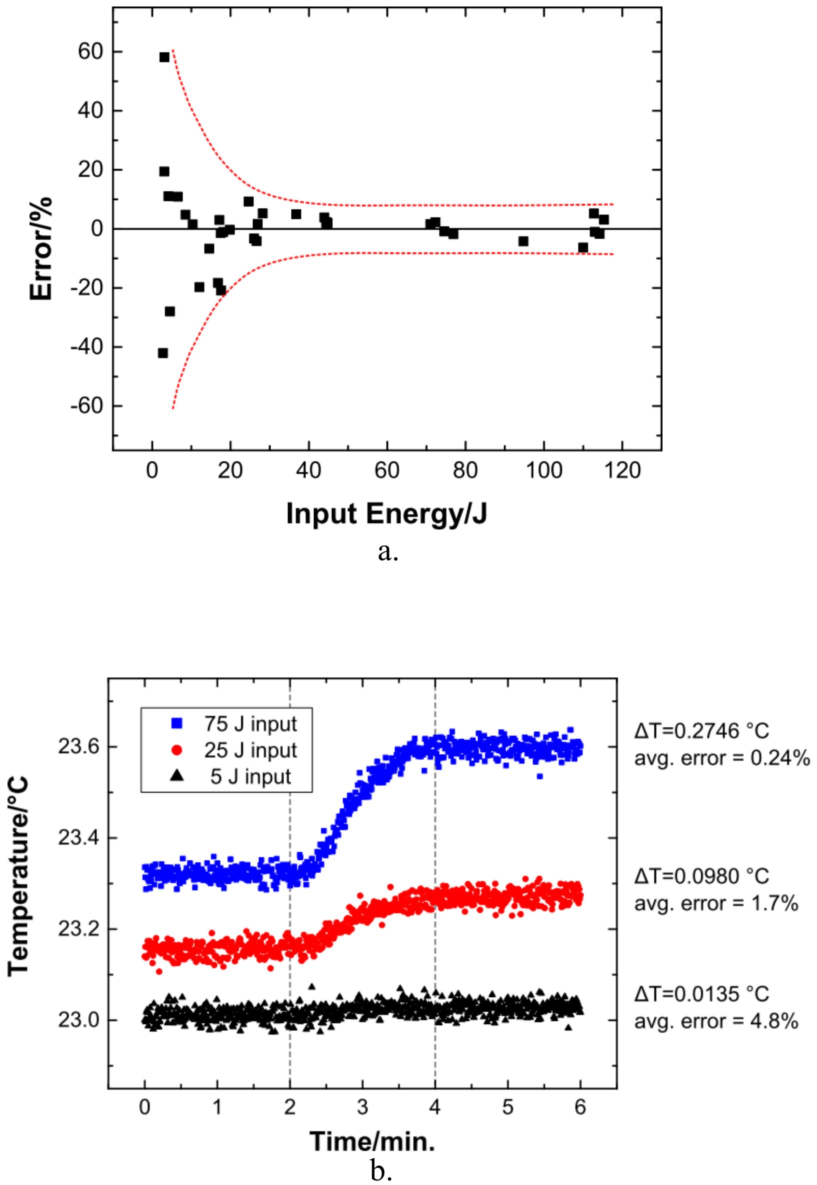

a.

b.

Figure 2.4: (a) Percent error as a function of energy input using an electrically heated filament. The dotted red lines were drawn as an estimated bound to the data spread, to emphasize how uncertainty increases drastically as input energy decreases below ≈20 J, though it does so symmetrically around zero and therefore remains accurate to about 5% when data points are averaged. (b) Raw calorimetry data for three of the data points shown in (a), to demonstrate the sensitivity of the calorimeter. The ΔT values calculated for each run are provided, along with the average error for five equivalent electrical pulses. The baseline temperatures for each were shifted for easier comparison, since only ΔT and not absolute temperature is important.

2.7 Conclusion

We have successfully designed a bomb calorimeter that measures the heat generated by reactive multilayer foils and is optimized for their unique geometry and small sample mass. Special considerations for these unique reactions include suspending the foil to reduce thermal contact area, and igniting the samples with low-energy sparks. The sensitivity of this instrument is orders of magnitude higher than that of the most sensitive commercial bomb calorimeters, with a calorimeter constant $\varepsilon_{(\mathrm{calor})} = 279 \pm 6\ \mathrm{J\ K^{-1}}$, enabling measurements for reactions as small as approximately 20 J without significant loss of precision. This high level of sensitivity is primarily accomplished by minimizing the system's heat capacity by using silicone oil for the liquid bath rather than water, and by designing the bomb to be as small as possible. The instrument was successfully utilized to gather combustion data presented in the upcoming chapters.

3 Using Magnesium to Maximize Heat Generated by Reactive Al/Zr Nanolaminates

3.1 Introduction

Previous work has shown that a multilayer system with a 1:1 atomic ratio of Al and Zr leads to longer burn times than foils with 3Al:Zr or Al:Ni chemistries, and therefore may be a good starting point for developing materials with tunable burning characteristics and the potential for significant heat production [17]. To further enhance heat generation, we then experimented with the addition of Mg to the Al layers in these Al:Zr foils.

Al-Mg alloys are frequently used in pyrotechnics [79], and can lead to more complete combustion than pure Al particles because Mg will preferentially oxidize before Al, but its oxide does not passivate the system as does Al_2O_3 [80]. Mg is also a more volatile metal, boiling at only 1091°C [81], and can potentially deform and fracture the reacting material as it boils, perhaps assisting the combustion process as a result [82]. Other groups have shown that Al-Mg particles can have more desirable ignition and combustion properties than pure Al particles [83–86]. By using Al-Mg alloys as an alternative to pure Al, we hope to leverage these advantageous properties to improve the system's extent of combustion and total heat release.

The study described in this chapter was conducted using free-standing, sputter-deposited foils with alternating nano-scale layers of Zr and either Al, Al-8at.%Mg, or Al-38at.%Mg. We characterized reaction temperatures, the ejection of vapor and particles, and the total heats of reaction in air, oxygen, and nitrogen. The compositions and morphologies of the final reaction products were examined using multiple techniques and the three reactive chemistries were compared in detail to identify the benefits of Mg within the Al layers.

3.2 Experimental Methods

3.2.1 Fabrication

Reactive multilayer foils were fabricated by DC magnetron sputtering, using targets purchased from Plasmaterials in Livermore, CA. The foils of interest were sputtered using 99.7 at.% Zr targets, in conjunction with either Al-1100 (min. 99 at.% Al), Al-8at.%Mg, or Al-38at.%Mg targets, all in atomic percent. A repeating Al/Zr or Al-Mg/Zr bilayer structure was formed by sputtering onto brass substrates fixed to a water-cooled, rotating carousel. Power to each sputtering cathode was adjusted to select a certain deposition rate (and therefore layer thickness) that corresponds to the desired atomic ratio. Each set of samples had a maximum total thickness of approximately 40 µm, and a maximum bilayer spacing of approximately 80 nm.[1] The foils were removed from the substrates mechanically as specimens measuring 10 mm wide, and 52mm long.

We sputtered multilayer foils with three different compositions for this study: Al:Zr, Al-8Mg:Zr, and Al-38Mg:Zr. The colon is used to show a stoichiometric atomic ratio, indicating that the aluminum alloy and the zirconium have a 1:1 molar ratio. This notation indicates that Al-8Mg:Zr, for example, consists of layers of zirconium alternating with layers of an alloy that is 92 at.% Al and 8 at.% Mg. These labels

---

[1] Maximum values are given because the fabrication process inherently leads to a range of thicknesses and bilayer spacings, due to the fact that the deposition rate is highest at the center of the substrate and decreases towards the outer edges. The thickness of the foils used ranged from ≈25-40 µm, with bilayers ranging from ≈50-80 nm.

therefore provide nominal compositions calculated using the sputtering parameters, but elemental analysis of the as-fabricated foils show more Al and less Zr and Mg than expected for each sample type (see **Table 3.1**). We attribute the high Al to Mg ratio to more scattering of Mg than Al in the plasma, and we attribute the higher Al to Zr ratio to consistent small errors in the calibration of the Al, Al-Mg, and Zr sputter rates.

	Measured Foil Compositions [at.%]		
	Al:Zr	**Al-8Mg:Zr**	**Al-38.5Mg:Zr**
Mg	0.0	3.8	14.7
Al	55.8	53.8	42.1
Zr	44.2	42.5	43.2

Table 3.1: Compositions of each foil in at.% based on elemental analysis by ICP-OES

The three compositions used were selected based on our goal to compare samples with no Mg (Al:Zr) against samples with a small amount of Mg (Al-8Mg:Zr) and against samples with a large amount of Mg (Al-38Mg:Zr). These two particular Al-Mg alloys were selected because they fall within a range commonly found in pyrotechnic formulations, and the Al-38Mg alloy is the first Al-rich intermetallic within the Al-Mg system. However, we note that sputtering from either target onto water-cooled substrates yielded solid solutions, as verified by XRD of the unreacted foils (**Figure 3.1**). Co-sputtering from an Al-8Mg target and an Al-38Mg target simultaneously to obtain intermediate compositions will allow for additional optimization in future efforts.

3.2.2 Reaction Heats, Temperatures, and Products

A NAC Memrecam HX-6 High Speed Camera was used to record the foils reacting at 10,000 to 50,000 frames per second. The foils were held horizontally in a metal frame, and an electrical spark from a 50 V power supply was applied at one end to initiate the reaction.

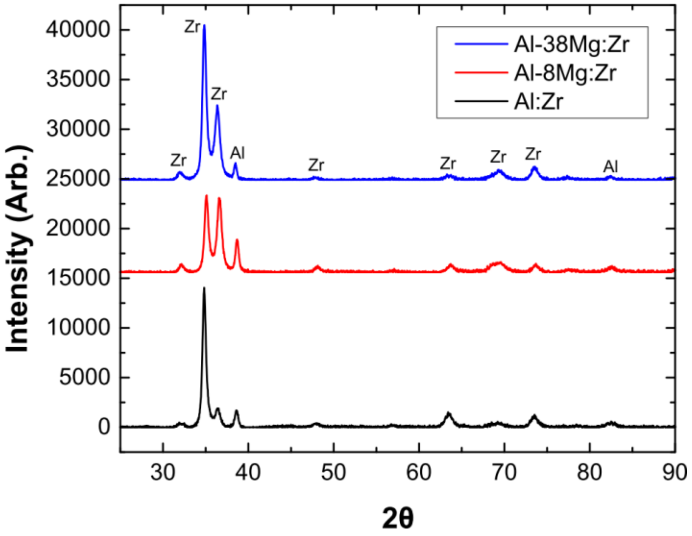

Figure 3.1: XRD results for as-deposited foils of each chemistry. Because no new peaks appear as Mg is added and the (111) Al peak at approximately 38 degrees 2θ shifts higher, we argue that the Mg is in a solid solution with the Al rather than forming intermetallics.

A two-color pyrometer, similar to one described in [87], was used to compare reaction temperatures as a function of time for the three chemistries. Samples were held vertically during these temperature measurements, with the top and bottom edges clamped between glass slides to prevent the foils from folding during the reaction, while minimizing heat-sinking effects. Ignition was achieved using an electrical spark from a power supply at ≈25 V, connected to two electrodes at the bottom of the foil's exposed surface. The pyrometer was focused on a 1mm diameter circle at the center of each foil.

The total heat generated by each sample was measured with the high-sensitivity bomb calorimeter that was described in **Chapter 2**. Experiments were conducted in air, pure oxygen, and pure nitrogen environments because an unknown mixture of these gases will be present for our final application. Tests were also performed in pure argon, in which only the intermetallic reactions can occur. An internal pressure of ≈1 atm was used for each test.

Elemental maps of reacted foil cross-sections were collected on a JEOL JXA 8500f Electron Microprobe at the National Institute of Standards and Technology. Microscopy foil samples were reacted with an electrical spark while suspended in air, then fractured along their widths or down their lengths to obtain various cross-sectional views. Samples were then mounted in epoxy, polished to 1 μm, and carbon-coated to prevent charging. Regions of interest, such as exterior surfaces, pores, or different phases towards the center of the foil, were all analyzed for chemical composition in order to identify the mechanisms at play during these reactions.

3.2.3 Characterization of Ejected Material

Foils containing Mg discharged both vapor and particles during their reactions in all environments. The chemical species of the gaseous products from Al-8Mg:Zr reactions were determined using atomic absorption and emission spectroscopy. We focused on the 8%-Mg alloy because, as presented in the results below, it produces more heat than the 38% alloy and is therefore of greater interest. Spectroscopy tests were also performed on Al:Zr samples for comparison. The foil samples were held horizontally and reacted in a small, windowed chamber. Light was passed through the reaction chamber ≈5 mm above the foil, directly through any vapor produced during the reaction. The light then continued out of the opposite window and into the spectrometer, in which a CCD camera sampled at 50 Hz for two seconds, automatically triggered at the ignition event. We used a xenon flash lamp as the broadband light source, set to flash at 50 Hz with 1200 mJ of energy per pulse, each pulse lasting 10 µs. Experiments were performed in air and argon environments, both at atmospheric pressure.

Because this technique only provides information for products in the vapor phase, TEM-EELS (Transmission Electron Microscopy- Electron Energy Loss Spectroscopy) was performed to characterize the larger particles being ejected. The particles were collected for analysis by reacting foils in air and argon under 3 mm diameter, 200 mesh Cu grids with holey-carbon support films. The collected particles were then analyzed using a Philips CM300 Field Emission Gun TEM equipped with a Gatan GIF200 EELS detector.

The combination of the above techniques tells us *what* is being ejected, but not *how much*. To quantify the composition and mass of all the material expelled during the reactions, foils of each type (Al:Zr, Al-8Mg:Zr, and Al-38Mg:Zr) were reacted in sealed glass vials, so that all of the ejected mass, whether solid, liquid, or gas, was deposited onto the inside of the vial. The reacted foil was then extracted and put into a separate glass vial so that each sample was divided into two parts: one with just the ejected mass on the walls of the vial, and one with the reacted foil. Each vial was filled with a precise volume of several acids that fully digested the metals. Next, Inductively Coupled Plasma-Optical Emission Spectroscopy (ICP-OES) was performed upon the acid solutions by Galbraith Laboratories Inc. to identify the presence of each metal down to 0.5 µg. We then used the measured concentrations to calculate the total mass of each metal discharged, as well as the mass of each metal remaining in the foil.

3.3 Results

3.3.1 Reaction Images and Temperatures

High speed video footage of reactions in air shows that Al:Zr foils do not eject material, and tend to maintain their basic morphology throughout their reactions. The intermetallic formation reaction propagates at approximately 3.1 m/s for these foils. Al-8Mg:Zr foils, however, discharge a cloud of vapor and particles as their intermetallic reaction propagates down the foil at ≈1.3 m s^{-1}, and continue to expel vapor and particles for approximately 0.06 s after the formation reaction has passed that location. The foil then burns for about a quarter of a second, with no visible particles or vapor. The particles oxidize as they are ejected and can be seen dividing into multiple smaller pieces as they are projected away from the foil. Similar behavior is observed from Al-38Mg:Zr foils, but their intermetallic reactions propagate more slowly (≈0.45 m s^{-1}), and the expulsion of material occurs over a much broader range of time. Ejection of both vapor and particles begins at the start of the formation reaction and continues until the particle ejection abruptly stops after ≈0.4 s, and the vapor gradually fades out with the oxidation reaction after an additional 0.1 s. The rate of vapor production during the intermetallic reaction is much greater than during oxidation and nitridation, but particles are ejected at a consistent rate through both reaction stages. The still images in **Figure 3.2** are taken from points in high speed videos that correspond to the end of the intermetallic reaction in order to show that there is no particle ejection from Al:Zr foils, but Mg-containing foils release a cloud of vapor and glowing hot particles. The Al-38Mg:Zr foils produce more vapor than the Al-8Mg:Zr foils.

The foils frequently roll or curl when reacted in air, and the degree of rolling or curling appears to correlate with Mg content; the behavior is typically least severe with Al:Zr foils, which experience only minor curling of the edges, as opposed to Al-38Mg:Zr samples, in which the entire middle region can roll into a cylinder. Curled regions stay hot for a greater duration, and in one extreme case, such a region on an Al-38Mg:Zr foil was observed to stay hot for 10.5 s after the rest of the foil had cooled. This severe case is atypical; the edges of most Al-38Mg:Zr foils reacted in air continue to glow for approximately 2 s longer, but the behavior for foils of all types is irregular and unpredictable, so the range is broad. This curling effect does not occur for any foil reacted in argon.

In addition to imaging the reactions, we also investigated the temperature profiles for each foil-type. Averaged curves for the temperature profiles of the three Al-Mg alloys of interest (0% Mg, 8% Mg, and 38% Mg) are shown in **Figure 3.3a**. The initial spikes in temperature to approximately 1700 K are attributed to the intermetallic reactions, and are followed by a plateau associated with the foil burning at a slightly lower temperature. When reactions are performed in argon, the same intermetallic spikes appear but with no oxidation plateau. The pyrometry results in air show that Al:Zr foils burn for approximately 2 s near 1600 K. Al-8Mg:Zr foils combust for a much shorter duration, ≈0.25 s, but at the highest temperature; about 1675 K. Al-38Mg:Zr foils have the lowest combustion temperature, at roughly 1500 K, but burn for about twice as long as the Al-8Mg:Zr foils (≈0.5 s). For each of these, the temperatures are in a range where any Al or Al-Mg phases will be molten [88], while Zr and Zr-Al phases will be solid [89]. There are no Zr-Mg phases because Mg and Zr are immiscible [90].

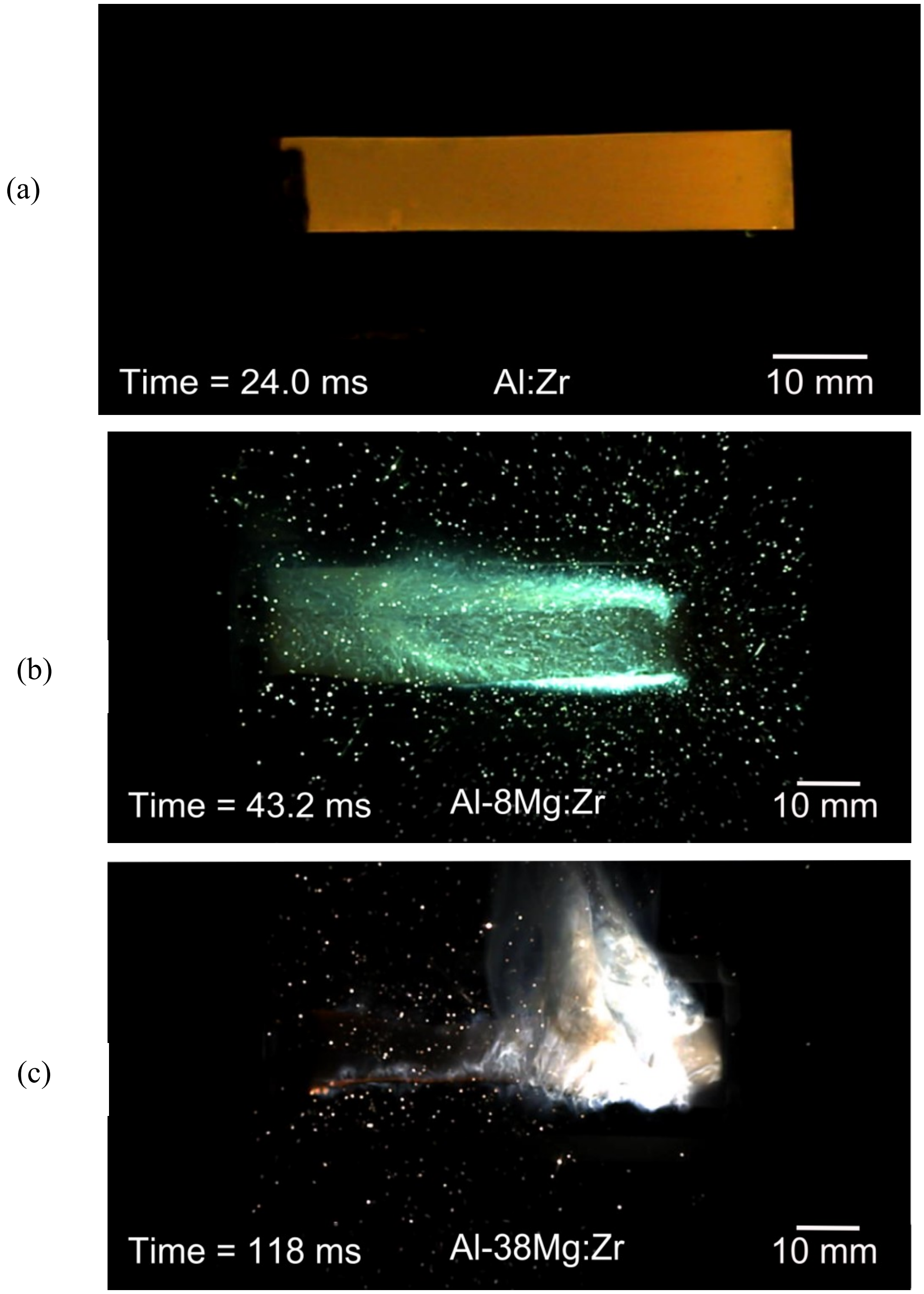

Figure 3.2: These still frames from high-speed videos show (a) Al:Zr, (b) Al-8Mg:Zr, and (c) Al-38Mg:Zr foils reacting. Each foil is reacted suspended horizontally in air, and ignited using a spark on the edge towards the left side of frame. The full lengths of all three foil types burn brightly, but the Mg-containing foils appear dark in the images because the camera aperture was closed more to prevent the much brighter Mg clouds from oversaturating the detector. The green coloration in the video of an Al-8Mg:Zr foil reacting is also the result of the camera settings and is not scientifically relevant.

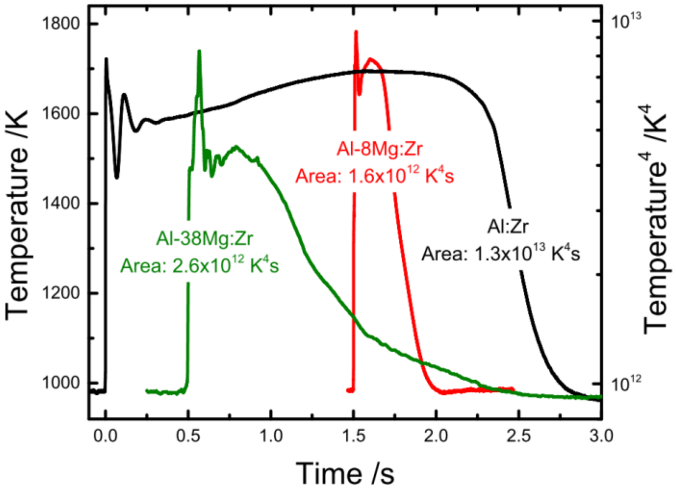

a.

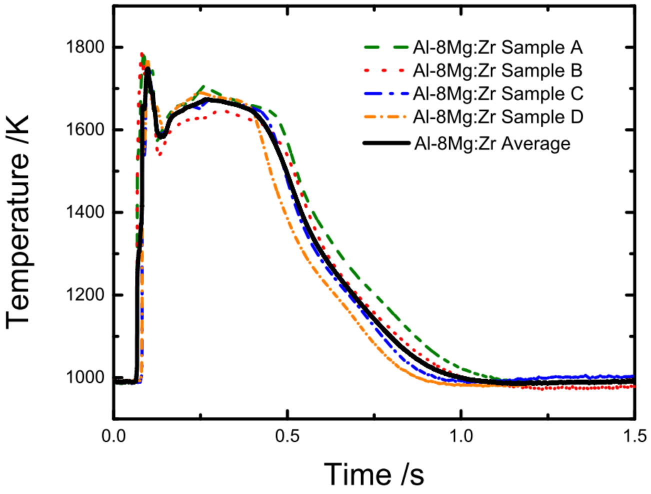

b.

Figure 3.3: (a) Temperature profiles of the three compositions reacting in air. Each sample is approximately 40 μm thick. Temperatures are given as T as well as T^4, because area under T^4 curves is thought to scale with radiative heat loss [17]. (b) The repeatability of the measurements is demonstrated with similar samples of Al-8Mg:Zr (≈40 μm thick, with a ≈56 nm bilayer spacing) reacted in air. The pyrometer is only sensitive to temperatures above 1000 K and hence the apparent baseline is misleading as it represents all temperatures below 1000 K.

Figure 3.3b shows that such measurements are repeatable, though significant variations are measured if the pyrometer is focused on a region of the foil that happens to roll, as previously discussed. Although repeatability can be attained for a single set of experiments with identical foils, we estimate that the error in the temperature calibration is ≈100 K. Also, foil composition may vary slightly between batches of foil samples, and combustion behavior is influenced by foil geometry, as will be discussed in **Chapter 5**. These factors may explain the slight discrepancy between these results and those presented previously in [17] for the Al:Zr samples.

3.3.2 Total Heats of Reaction

As our primary concern is a comparison of the total heat output between foils of each chemistry, we designed and built a highly sensitive bomb calorimeter, specialized for reacting nanocomposite foils with masses on the order of 100 mg. **Figure 3.4** shows the bomb calorimetry results for each chemistry in the four environments of interest: oxygen, air, nitrogen, and argon. The data reveals that the Al-8Mg:Zr samples produced the most heat in each environment aside from argon, and were particularly superior in nitrogen, in which they generated approximately three times more energy per gram than the other two chemistries. Experimental values were typically calculated as averages of at least three runs.[2] Every sample reacted in oxygen collapsed to form a single large bead of product,

---

[2] Only two runs were performed for Al:Zr samples in oxygen because molten globules of metal would fuse to the wall of the bomb during testing. Given the two runs were in good agreement, the third run was skipped to prevent damage to the calorimeter. Only one run was performed for Al-38Mg:Zr samples in argon because reactions in these samples typically quenched immediately after ignition. We deemed it unnecessary to modify the calorimeter to obtain more data points for these tests because heat generated in argon is of less interest, and the single value obtained for the Al-38Mg:Zr foil matched expectations.

suggesting that the foils were completely molten while reacting in this environment, and were able to reshape to minimize their surface area.

The theoretical maximum heat possible for each particular chemistry and environment was calculated by assuming complete oxidation of the foils when reacted in air and oxygen environments, and complete nitridation of the foils when reacted in nitrogen. The values were calculated by summing contributions from the literature values for standard enthalpies of formation for Al_2O_3, ZrO_2 and MgO; or for AlN, ZrN, and Mg_3N_2, based on the predicted elemental composition [91].

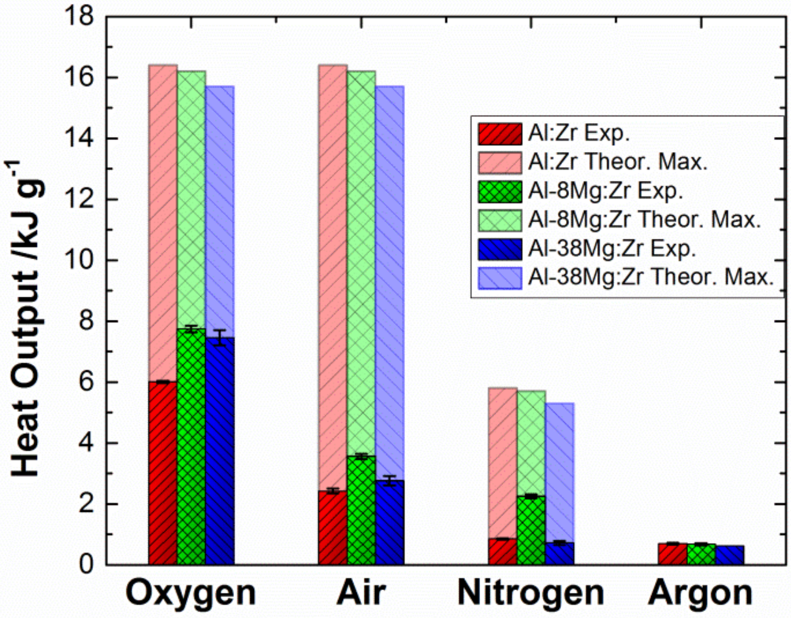

Figure 3.4: Heats of combustion, measured by bomb calorimetry. Data is reported in kJ g^{-1} for each composition and environment, showing experimental values (dark segments) as well as the theoretical maximum values calculated for 100% combustion efficiency (faded segments).

The ratio of the experimental heats to theoretical heats can be thought of as the combustion efficiency, or the extent of the oxidation or nitridation. The combustion efficiency is higher for Mg-containing samples than for Al:Zr samples, with Al-8Mg:Zr foils reaching almost 50% efficiency in oxygen and 40% in nitrogen. Al-8Mg:Zr samples produced the most heat per gram in all three reactive environments, though Al-38Mg:Zr foils perform similarly in oxygen. Theoretical maxima for samples reacted in argon are not visible because in an inert environment, only the intermetallic reactions are possible, and these all go to completion. Therefore, the measured values are approximately equal to the literature value for the heat of formation for the AlZr intermetallic [92] and decrease as Mg is added.

3.3.3 Reacted Foil Morphologies and Compositions

Figure 3.5 compares foil cross-sections taken across the width of 40 µm thick samples that were reacted in air. The binary Al:Zr samples oxidize on their outer surfaces only and are not porous, though we do see large bubbles forming between the oxide layer and the intermetallic central regions (**Figure 3.5a,b**). Al-8Mg:Zr samples have fewer large bubbles, but contain a high density of voids throughout, and show significant expansion to about 70 µm in thickness (**Figure 3.5c,d**). Analysis of the Al-8Mg:Zr foil cross-section in **Figure 3.5d** indicates that voids account for 64% of the total area, though porosity is highly variable and more dense regions of the same foil are only about 37% porous. The Al-38Mg:Zr samples (**Figure 3.5e,f**) are typically more dense, with approximately 21% porosity, mostly concentrated at the surfaces. In general, the Al-38Mg:Zr samples also have the most variability within each cross-section, as shown in **Figure 3.5e**. Some segments are reduced to about 5 µm in thickness, while other segments expand up to

100 µm. Each cross-section in **Figure 3.5** was taken across the width of the sample, approximately halfway along the foil's length, where the most significant oxidation occurs. It is evident from the mosaics of the foil widths that the severity of rolling while reacting is a function of Mg-content, since the reacted Al:Zr foil remains relatively flat while the Al-38Mg:Zr cross-section has experienced a dramatic change in shape. All foils in **Figure 3.5** were originally 10 mm wide, but the Al:Zr foil broke during the mounting process, and the Al-38Mg:Zr foil curled and shriveled to the point that it's width is greatly reduced.

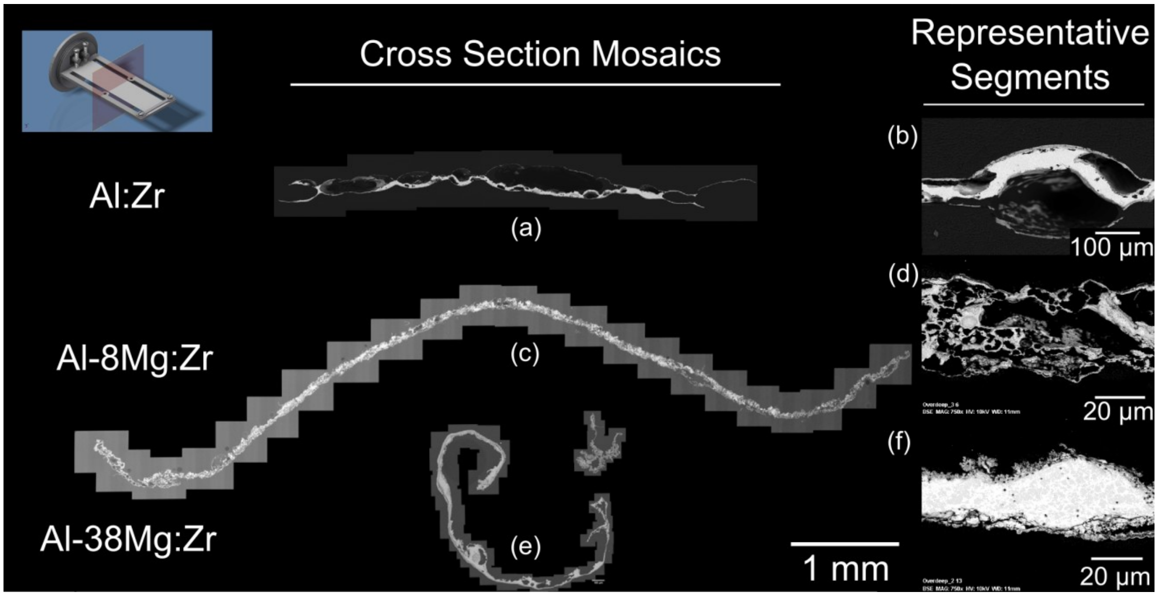

Figure 3.5: Microprobe (a,b,d,f) and SEM (c,e) cross-sections of each foil after reacting in air, with mosaics providing morphological comparisons for entire foil widths on the left, and detailed high magnification images on the right. The schematic in the top-left corner shows a foil mounted on the ignition frame, highlighting the plane at which the foils were fractured to obtain these cross-sections.

While elemental data is not shown in **Figure 3.5**, it was collected for a variety of regions across many foils that were reacted in air. The elemental maps for the Al-8Mg:Zr and Al-38Mg:Zr foil cross-sections displayed in the **Figure 3.5** can be found in **Figure 3.6** and **Figure 3.7**, and a map of an Al:Zr foil cross-section can be found in [17]. Oxygen and nitrogen are found at their highest concentrations on the exterior surfaces of each reacted foil, with lower levels throughout the central regions. The amounts of N and O in only the inner-most regions of each foil are listed in **Table 3.2**, and it is evident that much higher levels of O and N are present in the center of the Al-8Mg:Zr foils compared to the other two chemistries. The values for Al-8Mg:Zr and Al-38Mg:Zr samples are the total compositions measured in a rectangular area extending about 100 μm across the foil width and 10 μm across the center of the foil thickness. Values were observed to fluctuate severely with local morphology; for example, localized zones in Al-8Mg:Zr samples reach as high as 40 at.% N, while thicker, more dense areas of Al-38Mg:Zr foils had oxygen and nitrogen levels as low as 1 at.%. The values for Al:Zr samples, however, are from earlier experiments and are taken from the average of two points in the interior of the foil, but there is far less variability in these foils and so the values are accurate representations. The representative cross-sections used for these analyses are those provided in **Figure 3.5**.

	Average concentration at the foil center [at.%]		
	Al:Zr	**Al-8Mg:Zr**	**Al-38.5Mg:Zr**
Oxygen	4.16	14.37	5.75
Nitrogen	6.25	28.15	7.37

Table 3.2: Comparison of post-reaction nitrogen and oxygen levels (in at.%) at the interior of each foil after reacting in air.

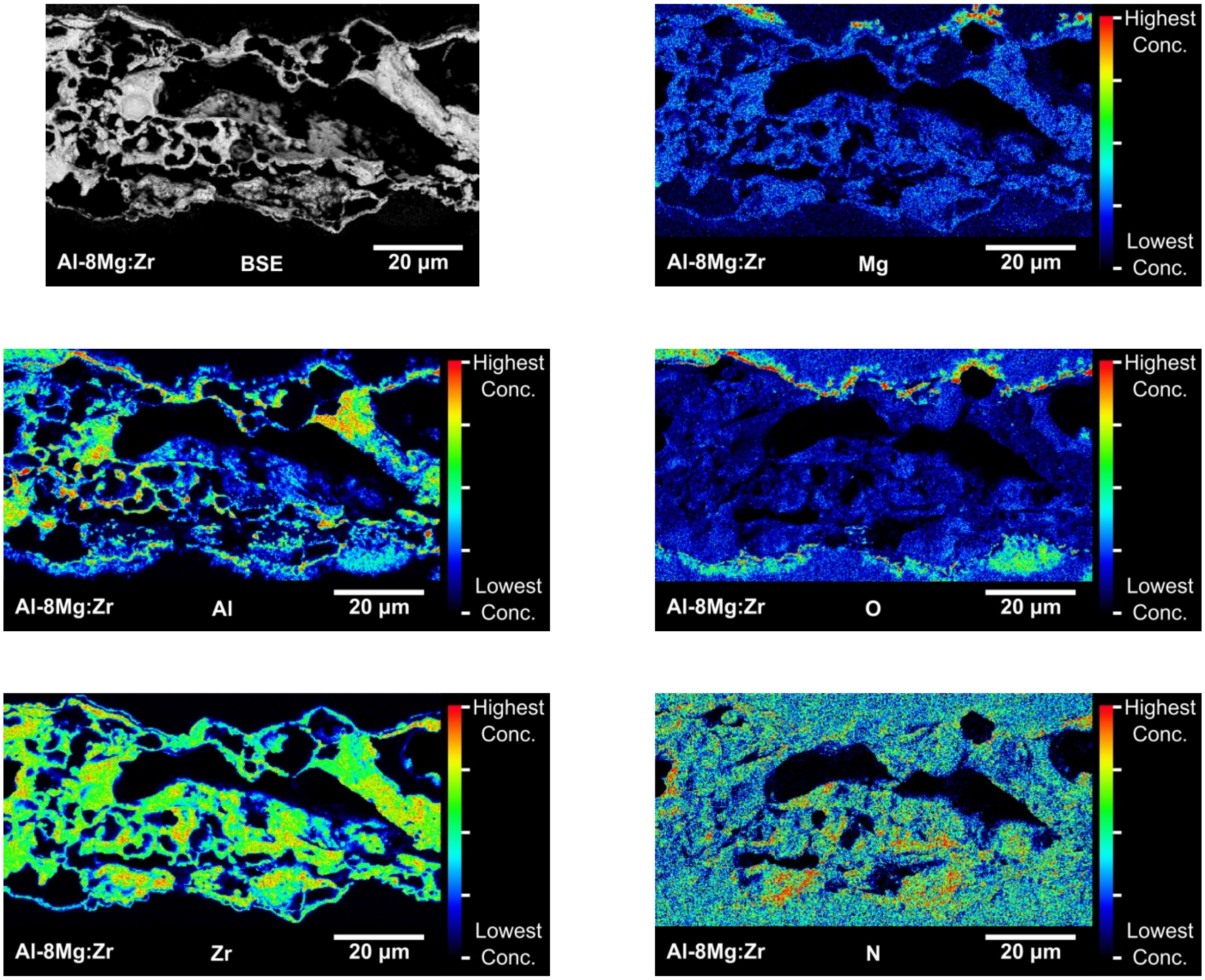

Figure 3.6: Microprobe elemental maps for a representative foil section (shown in Figure 3.5d) from an Al-8Mg:Zr foil. The coloring corresponds to relative amount of that species, where black areas have the lowest concentration and red areas, the highest. The images include (a) a back-scattered micrograph, and compositions for (b) Al, (c) Zr, (d) Mg, (e) O, and (f) N.

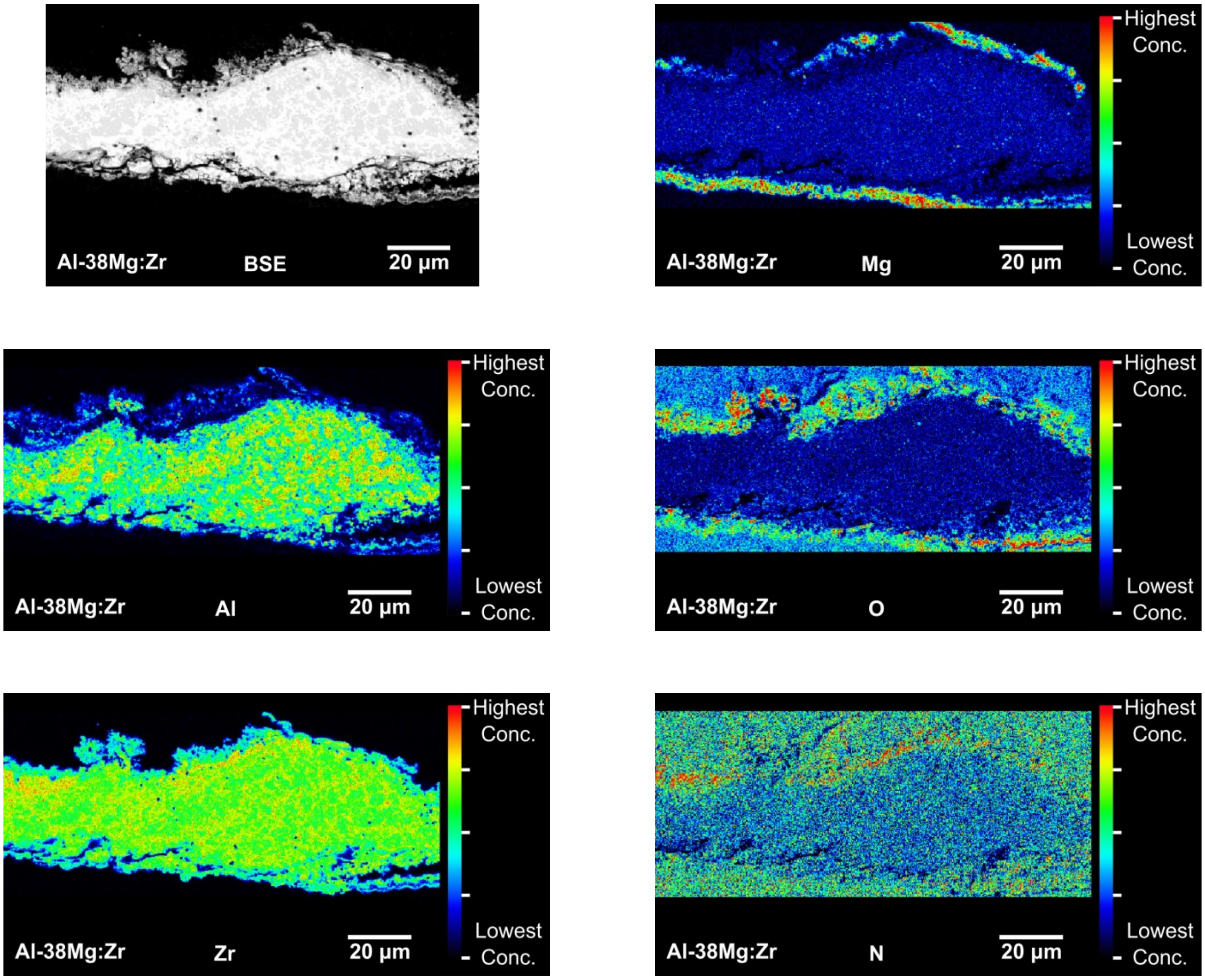

Figure 3.7: Microprobe elemental maps for a representative foil section (shown in Figure 3.5f) from an Al-38Mg:Zr foil. The coloring corresponds to relative amount of that species, where black areas have the lowest concentration and red areas, the highest. The images include (a) a back-scattered micrograph, and compositions for (b) Al, (c) Zr, (d) Mg, (e) O, and (f) N.

3.3.4 Characterization of Ejected Material

Atomic absorption and emission spectroscopy confirm that Mg vaporizes during the reaction of Al-8Mg:Zr foils in air and in argon, as indicated by the sharp Mg atomic absorption peak appearing at 285 nm [93], 0.01 s after Al-8Mg:Zr samples are reacted in either environment (**Figure 3.8a** and **b**). The characteristic peaks for the possible metal oxides are found at slightly higher wavelengths [94–98], shown in **Figure 3.8c** where we see a series of MgO emission peaks from Al-8Mg:Zr samples reacted in air. MgO peaks are already present in the earliest possible measurement at t=0.01±.01 s, alongside a set of atomic Mg emission peaks at 516-518 nm. No Al or Zr peaks were observed after reacting the Al:Zr and Al-8Mg:Zr samples in either air or argon. We can assume that the same species would vaporize from Al-38Mg:Zr foils, and so we focused on the 8%-Mg alloy because, as presented in **Section 3.3.2**, it produces more heat than the 38% alloy and is therefore of greater interest.

Although these tests show that Mg and only Mg is vaporizing, this spectroscopic technique cannot detect the larger particles we see being ejected in high speed videos of these reactions. TEM-EELS (Transmission Electron Microscopy- Electron Energy Loss Spectroscopy) was therefore performed on particles discharged in air, after collecting them on TEM grids held above reacting Al-8Mg:Zr foils. The analysis reveals that homogeneous MgO, ZrO_2, and Al_2O_3 particles are present, with a wide variety of shapes and sizes, as depicted in **Figure 3.9**. Each particle is a single metal oxide; no particles contained more than one metal, and no unoxidized metals are found on the carbon grid.

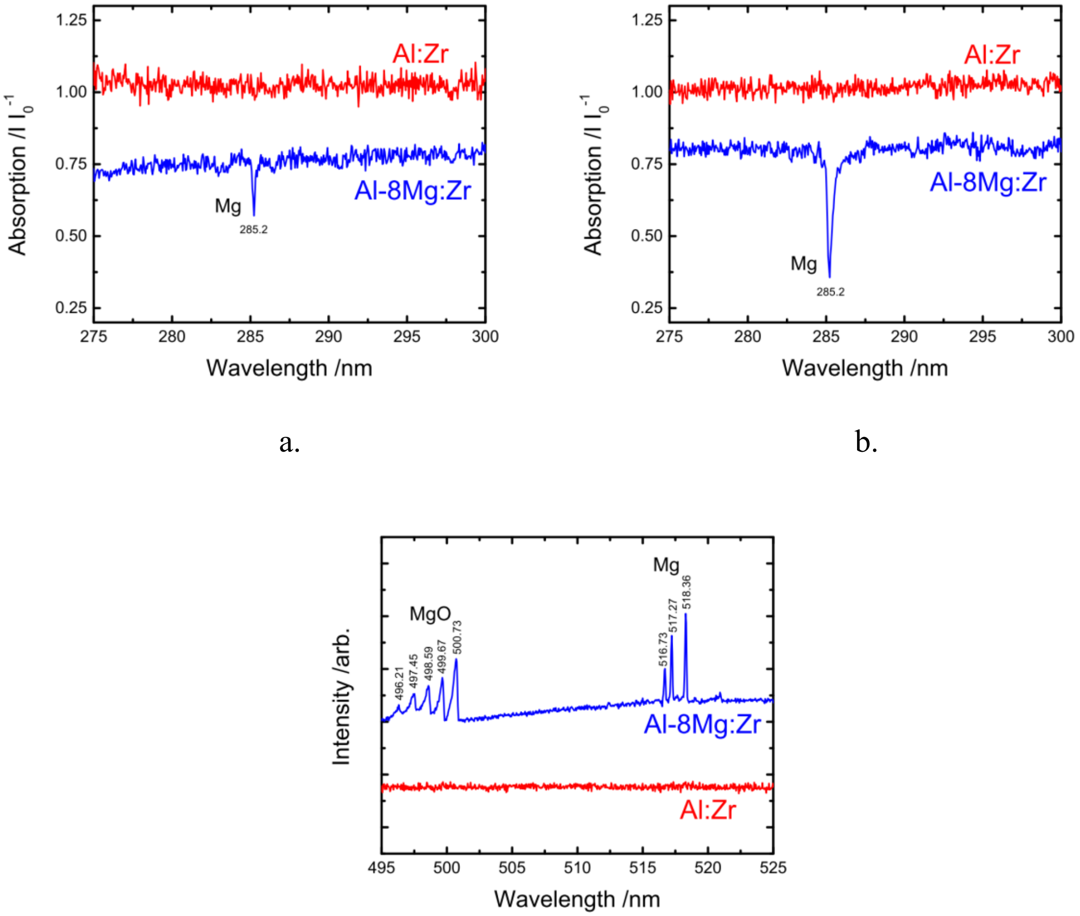

a.

b.

c.

Figure 3.8: Spectroscopic characterization of the vapor released from an Al-8Mg:Zr foil, with an Al:Zr foil shown for comparison. The reaction starts at t=0. The peaks persist for varying durations, and the particular spectra shown were selected for optimal signal to noise ratio. (a) Absorption at lower wavelengths from foils reacted in air, measured at t=0.15±.01 s. (b) Absorption at lower wavelengths from foils reacted in argon, measured at t=0.11±.01 s. (c) Emission at higher wavelengths from foils reacted in air, measured at t=0.03±.01 s.

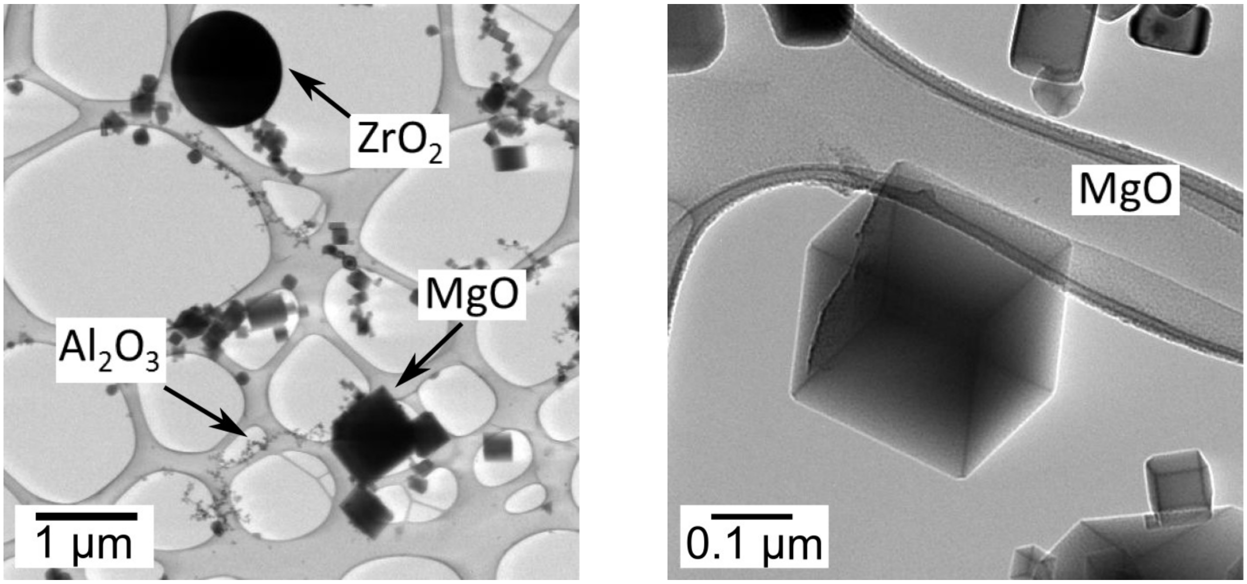

a. b.

Figure 3.9: TEM images of particles ejected in air that were analyzed for chemical composition. The particles of interest appear as dark shapes adhered to the grey, web-like structure, which is the holey-carbon support film. Lighter areas are open spaces. (a) Single metal-oxide particles with a wide range of sizes and shapes. Representative particles are labeled, though size and shape of each metal oxide varies widely. (b) A cubic MgO single crystal at higher magnification.

Spectroscopy of the vapor and TEM analysis of the particles effectively tell us *what* is being ejected from reacting foils, but neither technique provides information regarding the *quantity* of each metal being ejected. For this, ICP-OES of reacted foils and their ejected particles and vapor was performed. The results in **Figure 3.10** show that the percent of metal ejected increases with increasing Mg content, going from negligible amounts from Al:Zr samples, to 4.0 at.% for Al-38Mg:Zr samples. Most of the ejected material was Mg: 2.2% of the 2.9% discharged from Al-8Mg:Zr foils, and 3.7% of the 4.0% discharged from Al-38Mg:Zr foils. It should be noted that although more Mg was ejected from Al-38Mg:Zr samples, it was a much smaller fraction of the initial Mg content than was released from Al-8Mg:Zr samples, for which more Mg was found outside the foil (2.2%) than remaining within the foil (1.6%).

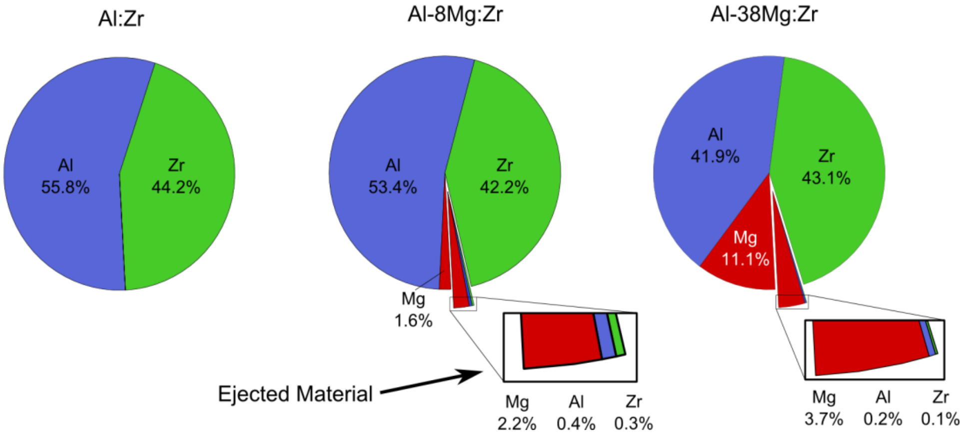

Figure 3.10: Results from ICP-OES tests detail the fate of each metal after reacting foils in air, presented in atomic percent of the initial foil content. The main area of each chart corresponds to the atomic percent of each metal remaining in the foil. The expanded segments show the atomic percent of each metal ejected. The initial concentration of each metal in the foil before reacting is the sum of the ejected and remaining mass for that metal.

3.4 Discussion

In an earlier study, temperature-time data gained from pyrometry measurements was used to estimate the heat produced by Al:Zr foils reacting in air [17]. This simple analysis, if utilized here, suggests that Al:Zr foils produce the most total heat, and Al-8Mg:Zr foils produce the least. However, the comparison has multiple shortcomings. First, it assumes that the pyrometer is completely emissivity independent and that convective and conductive heat losses are insignificant. Furthermore, the pyrometer only measures temperature at a single point approximately 1 mm in diameter on the surface of the foils, which is assumed to represent temperature across the entire sample, and gives no information regarding the temperature field surrounding the foil or for the ejected mass. These imperfect assumptions are compounded by differences in foil behavior or properties such as the degree of curling, mass ejection, and surface roughness, which we believe may be significant enough to influence the reported trends. Thus, a more direct measurement of heat production was utilized in this study, namely bomb calorimetry.

The bomb calorimetry data in **Figure 3.4** shows that Mg is a helpful addition to the Al/Zr multilayer foils and leads to increases in total heat production in all reactive environments. The heat generated by Al-8Mg:Zr and Al-38Mg:Zr foils reacted in oxygen are both about 24% higher than Al:Zr foils. The presence of Mg is even more helpful in air and nitrogen, which better represent the environments of concern for our application. The largest increase was a 2.7x improvement between Al:Zr and Al-8Mg:Zr foils reacting in nitrogen.

Increasing the ratio of Mg from Al-8Mg:Zr to Al-38Mg:Zr, though, decreases total heat output in each environment tested. In the inert argon environment, the heat production dropped by 8%, which is less than expected given that an additional 30% of the Al was replaced with Mg which is immiscible with Zr [90]. It is possible that the drop in intermetallic reaction heat was less severe than expected with the addition of Mg because that Mg vaporizes and may react with the small amount of oxygen remaining in the bomb after purging. The heat output decreases by only 4% in oxygen, but by 23% in air and by 68% in nitrogen. These large decreases in air and nitrogen cannot be attributed to Mg having a lower heat of combustion than Al, since the theoretical maximum drops by only 3.1% between Al-8Mg:Zr and Al-38Mg:Zr samples in air, and by 6.8% in nitrogen, as shown in **Figure 3.4**. One possible explanation is that higher Mg content lowers the combustion temperature due to greater evaporative cooling. Another explanation is the larger degree of curling for the Al-38Mg:Zr samples reduces the exposed surface area and might limit the rate of combustion. Either of these factors could lower the oxidation/nitridation temperature following the initial intermetallic reaction, as suggested by the temperature profiles in **Figure 3.3**. This in turn could lower heat production as reported in **Figure 3.4**.

The duration of burning seems to follow a pattern opposite to that of heat production: it drastically decreases when Mg is added, going from ≈2 s for Al:Zr foils to ≈0.25 s for Al-8Mg foils, but then increases back up to ≈0.5s for Al-38Mg:Zr foils. The duration of combustion is likely governed by the balance between heat production through oxidation and nitridation and heat losses via radiation and evaporation. Each of these factors depends upon Mg content, but their roles in determining the net impact of Mg on combustion duration are not yet known. Consider, for example, the fact that the extent of rolling and curling increases with Mg content. As noted above, greater curling should limit exposed surface areas for samples and hence combustion rates and potentially combustion duration. However, the reduced surface area will also reduce radiative cooling and therefore may extend the period of combustion. Thus, the net impact is unclear. Further still, the degree of curling varies within the high Mg-content foils, which explains their larger standard deviations (**Figure 3.4**). A more in depth analysis of the interpretation of burn temperature and duration is provided in **Chapter 5**.

Calorimetric measurements show that no foil, of any type, produced more than 49% of its theoretical maximum heat of combustion, even when reacted in pure oxygen. Thus, far more heat can be gained by increasing the extent of reaction, and so it is important to understand how Mg helps this process in order to increase heat production above 50% of the theoretical maximum. We now consider two mechanisms by which a small amount of Mg is able to increase total heat production in these foils:

First, Mg leads to the ejection of foil mass that oxidizes completely once outside of the foil, providing a boost to combustion efficiency. Mg is very volatile compared to Al and Zr [99], with a boiling point of only 1091°C, compared to 2519°C and 4409°C for Al and Zr, respectively [81]. Not only does the Mg itself vaporize and likely form the majority of the observed MgO particles, it also leads to the discharge and subsequent complete oxidation of some Al and Zr as well, in the form of micron-scale metallic particles. Particle ejection must at least be assisted by, if not enabled by, the presence of Mg, as both Mg-containing foils eject particles, while Al:Zr foils experience negligible mass loss (**Figure 3.10**) and high speed footage of their reactions shows no visible material expulsion (**Figure 3.2**). Similar behavior has been reported for Zr burning in oxygen/nitrogen environments [100–103]. The mechanism determined in these studies involves Zr taking up nitrogen early in the combustion process, but then displacing it with the thermodynamically favored oxygen after burning for longer durations. This liberates the nitrogen, causing the composition to exceed the solubility limit in the metal, resulting in pressure buildup and a subsequent explosion when the internal pressure overcomes the cohesive energy of the molten metal. This mechanism may indeed contribute to particle ejection, but we do not believe it is the primary mechanism because this would occur for Al:Zr foils as well, not just Al-8Mg:Zr and Al-38Mg:Zr foils.

The ejected particles are likely molten, given that they can reach higher combustion temperatures than the bulk foils where the temperature is being measured, and will therefore be well above the melting points for any Al-Mg phase [88]. They may also be above the melting points for some Al-Zr phases [89]. High speed videos of reactions for Al-8Mg:Zr and Al-38Mg:Zr foils show that the ejected particles explode into many smaller pieces shortly after ejection. The explosion likely occurs from a combination of the two mechanisms discussed above; the boiling of Mg and the dissolution of N, occurring in tandem within the particle's interior to cause the sudden explosion. This is currently under examination by performing the reactions in various environments to determine whether or not N is required for this behavior to occur. Preliminary results, though, indicate that explosions occur in mixtures of O_2 and Ar only, and therefore this mechanism is unlikely to fully explain the phenomenon.

TEM-EDS shows that all of the ejected material oxidizes completely in air because no pure metals were found, only their oxides. In addition, only one species of metal-oxide is present in each particle, either Al_2O_3, ZrO_2, or MgO, but never a mixture. The particles ejected in argon, however, contain all three elements, suggesting that particles are initially ejected as molten globules of mixed metals. The separation that follows ejection could occur if Al and Mg evaporate from the burning particles, resulting in Al vapor, Mg vapor, and a Zr particle, each of which oxidizes in air and remain separate as immiscible oxides [104]. Alternatively, immiscible metal oxides may form within the particles themselves, and separate into smaller particles upon the explosion event. Both of these arguments are consistent with the high-speed videos showing hot particles exploding into many smaller particles after ejection in air.

Although the driving force for the expulsion of particles and their subsequent explosions into many smaller pieces is intriguing, we are primarily concerned with how these processes affect the total heat production. The complete oxidation of all ejected mass, quantified in **Figure 3.10**, contributes 0.34 kJ g^{-1} for Al-8Mg:Zr foils, and 0.53 kJ g^{-1} for Al-38Mg:Zr foils. These values correspond to 14% and 21% increases in heat, respectively, compared to Al:Zr foils reacted in air. Although significant, these sums alone cannot fully explain the large heat gains we measured with the addition of Mg.

We therefore argue that the second and most significant impact of Mg is to enhance the diffusion of oxygen and nitrogen into and through the foil. The presence of even small amounts of Mg in the zirconia phase that forms on the outside of the foils should create oxygen vacancies in the ZrO_2. These will in turn enhance oxygen diffusion in the growing oxide [105,106]. In a similar manner, the evaporation of Mg from the foils should lead to a diffusion of Mg to foil surfaces that must be balanced by an inward flux of vacancies. This inward flux will increase the concentration of vacancies within the metallic regions of the burning foils, thereby increasing the rate of diffusion and the resulting oxidation and nitridation [107,108]. As a consequence, heat production also increases. The results provided in **Table 3.2** support this argument, showing that the central regions of the Al-8Mg:Zr foils have approximately 4x more oxygen and nitrogen in comparison to the Al:Zr foils, which would explain the large increases in heat measured by bomb calorimetry.

The Al-8Mg:Zr foil cross-sections in **Figure 3.5** show the existence of voids that are too large to result from the coalescence of excess vacancies alone. Instead, these voids likely nucleate from the vacancies and then grow as the oxides and nitrides form and force volume expansion within these foils. The associated stresses can be significant enough to promote void growth, as well as delamination between adjacent phases. The elemental maps of foil cross-sections in

Figure 3.6 and **Figure 3.7** show that oxygen, nitrogen, and magnesium are not found in higher concentrations at the internal surfaces of the voids, suggesting that they are completely enclosed and do not serve as channels for gas flow as we had originally hypothesized, and are therefore unlikely to be responsible for increasing combustion efficiency. The absence of nitrogen within these voids also suggests that it is unlikely that they result from the dissolution of N in the later stages of combustion. Fewer voids are seen in Al-38Mg:Zr samples, as we would expect based on their lower oxide and nitride contents and therefore smaller growth stresses. Stresses due to oxide growth likely generate the large voids at the outer surfaces of Al:Zr foils as well. We believe that the growing oxide buckles away from the underlying intermetallic in these locations, in order to relieve the compressive growth stresses.

Last, we address the kinetic competition between oxide growth and nitride growth when foils are reacted in air. Even though ZrO_2 is thermodynamically more stable than ZrN, XRD results for foils reacted in air, and the correlation between Zr and N concentrations in elemental maps, both show that ZrN does form in all samples. In fact, microprobe data in **Table 3.2** shows that nitrogen is more highly represented within the foils than oxygen. This suggests that kinetics are dominating instead of thermodynamics. The higher concentration of nitrogen in air (78 at.% N_2 and only 21 at.% O_2) [109] should lead to higher impingement and adsorption rates for nitrogen compared to oxygen. In addition, very thin depletion zones of oxygen may develop near the foils surface. In both cases, fewer oxygen atoms and more nitrogen atoms will diffuse into the foil, and nitride formation will be favored kinetically. While undesirable in many cases, the formation of nitrides can be beneficial in applications where oxygen may be limited.

Looking forward, the sputtered Al-Mg/Zr system serves as a prototype for a three-pronged approach to maximizing heat production by particle combustion: First, an intermetallic reaction brings the entire mass to high temperatures where oxidation occurs readily. Second, oxidation and nitridation is extended to relatively long durations via appropriate material selection. Lastly, the vaporization of at least one component enhances combustion efficiency. Using this combined strategy, we hope to investigate heat produced by other reactive nanocomposite systems that could utilize these mechanisms and potentially produce even larger quantities of heat than the Al-Mg/Zr chemistry.

3.5 Conclusion

We have shown that alloying aluminum with magnesium increases heat generation in Al/Zr multilayer foils that are reacted in air, oxygen or nitrogen. The presence of Mg leads to the evaporation of Mg and the ejection of alloyed metal particles. Both the Mg vapor and the metal particles oxidize rapidly and the particles split into single metal oxides. While the Al:Zr foils burn longer in air according to pyrometry studies, Al-8Mg:Zr and Al-38Mg:Zr foils produce more heat, as measured with a specially designed bomb calorimeter. The Al-8Mg:Zr foils generate the most heat of all three chemistries from reactions in air, oxygen and nitrogen. We propose two general mechanisms to explain the higher heat production. One is that the evaporated Mg and the ejected metal particles all oxidize completely, thereby increasing combustion efficiency. The other is that the presence of Mg enhances diffusion of oxygen and nitrogen through the foil and thereby increases combustion efficiency even further: Mg in the growing ZrO_2 layers should enhance oxygen and nitrogen diffusion by creating oxygen vacancies, and in a similar manner, as Mg evaporates from the foils, the outward flux of Mg is balanced by an inward flux of vacancies that should enhance the diffusion of oxygen and nitrogen into metallic interior of the foils. The suggested enhancement of diffusion into Mg-containing foils is supported by electron microprobe elemental maps of reacted samples that show more oxygen and nitrogen in the center of the foils, compared to Al:Zr foils with no Mg.

4 Mechanisms of Oxide Growth During the Combustion of Al:Zr Nanolaminate Foils

4.1 Introduction

We have shown in **Chapter 3** that we can improve the combustion efficiency of reactive Al/Zr nanolaminate foils by adding Mg to the Al layers. The highest heat output measured via bomb calorimetry in a pure oxygen environment, however, was less than 50% of the theoretical heat production. In order to improve combustion performance further, it is necessary to understand the reaction mechanisms, particularly for oxide growth. To this end, we have conducted in-situ X-ray diffraction tests on foils reacting in air. The benefit of this in-situ work is that it allows us to see the progression of phases and elucidate the mechanism of reaction, rather than making inferences based solely on characterizations of the final products.

These tests were performed using synchrotron radiation, which is of a higher energy, and therefore lower wavelength, than typical X-ray sources. This allows for more precise measurements, particularly at smaller d-spacings, and allows for transmission geometry diffraction. Synchrotron radiation also offers a high photon flux, and therefore is capable of collection useful quantities of data with very short exposure times, which is necessary for rapid in-situ measurements [110–112].

We propose a mechanism describing the combustion of these reactive nanolaminates by combining these preliminary XRD results with post-reaction micrographs of the foil cross-sections. Most notably, the growth of the zirconium dioxide combustion product switches from interface controlled growth to diffusion controlled growth 1.3 seconds into the reaction. At this point, the foil is unable to sustain a high, constant combustion temperature and the reaction terminates fairly rapidly. The proposed transition in combustion mechanisms is supported by earlier modelling work that was based on the temperature profiles acquired during the combustion of these Al:Zr foils [113] , and by the work of another group in which bulk Al/Zr intermetallics were oxidized at high temperatures [114].

4.2 Experimental Methods

Foils were fabricated by DC magnetron sputtering, as described in detail elsewhere **Section 3.2.1**. In short, two cathodes, one containing an Al-1100 target (>99.0% Al), the other a Zr target (99.7% pure), concurrently sputtered onto brass substrates that were secured onto a rotating, water-cooled carousel. With each full rotation of the carousel, the substrates passed each cathode in sequence to form a bilayer ≈70 nm thick. The total foil thickness was ≈40 μm after several hundred rotations, and the atomic ratio of Al and Zr was nominally 1:1, calculated based on the calibrated sputtering parameters.

In-situ XRD measurements were performed on Al:Zr foils in which reactions were initiated by uniform heating causing the foil to react homogeneously [115]. In this setup, the foils were clamped between two sets of copper blocks and a current pulse was sent through the foil, imparting the minimum amount of Joule heating required to bring the foil to its ignition temperature. The foil was held horizontally and the temperature was measured using a one-color pyrometer. The emissivity was adjusted to 0.17 in post-processing such that the peak in temperature during the intermetallic formation reaction is equal to the melting temperature (1590 °C) of the dominant intermetallic at that time, $AlZr_2$. The XRD experiments were performed at the A2 beamline at the Cornell High

Energy Synchrotron Source (CHESS) using 15 keV X-rays (0.6% energy bandpass) with an approximate x-ray flux of 10^{12} photons/second. A 1×2 mm^2 area of the sample was illuminated and scattering was measured in transmission mode. Diffraction patterns were collected during the reaction using a GE detector with a capture rate of 30 Hz that covered a wide range of scattering vectors (q) up to 80 nm^{-1}, measuring with a q step of .007813 nm^{-1}.

In order to confirm that various foils exhibit consistent reaction behavior, fourteen successful runs were completed. For each reaction, approximately 155 frames were recorded over a period of approximately 4.2 s. The 2D diffraction pattern for each frame was fitted and separated into individual Voigt peaks, and all phases were identified. The highest quality representative sample was chosen for complete analysis, in which a single distinguishing peak was identified for each phase that was present. **Table 4.1** below provides the details for each of these chosen peaks. The peak positions varied slightly throughout the reaction as a function of temperature due to thermal expansion and contraction of the lattice.

Phase appearance and subsequent growth or decline was tracked by measuring the integrated area of that peak for each frame. It is not possible to obtain quantitative data for how much of each phase is present using this method, but further analysis using Rietveld refinement is currently underway. With this more rigorous approach, theoretical diffraction patterns will be generated and fit to the experimental curves in order to obtain quantitative data for the relative amounts of each phase present.

Phase	Crystal System	Peak Position (nm^{-1})	Peak Index	Theoretical Intensity (0-100)
Al	Cubic	26.9	111	100
Zr	Hexagonal	25.6	101	100
Al_2Zr	Hexagonal	15.5	101	100
Al_3Zr_2	Orthorhombic	15.9	220	22
Al_3Zr_5	Hexagonal	17.7	200	23
Al_4Zr_5	Hexagonal	18.4	111	75
Al_2O_3	Monoclinic	45.2	512	99
ZrO_2	Orthorhombic	21.2	111	100
ZrO_2	Monoclinic	12.4	100	7
ZrN	Cubic	23.7	111	100
Amorphous	-	≈23.3	-	-

Table 4.1: Descriptions of the XRD peaks used to characterize each phase that was detected.

TEM samples were prepared by reacting foils (nominally identical to those used in the XRD) held vertically, clamped at the top and bottom by two sets of glass slides leaving 3 cm in the middle of the foil exposed for oxidation. The reaction was initiated by a small DC spark applied towards the bottom of the foil, from which point the intermetallic formation reaction self-propagated upward. A thin section of each of these foils was then embedded in epoxy and cut perpendicular to the propagation direction using a diamond saw. The cross-section surface was polished to 0.25 μm using a diamond suspension and a dual-beam FIB was used to cut and mount a thin section onto a TEM grid. The cross-section was then imaged and analyzed using a Philips CM300 Field Emission Gun TEM equipped with a Gatan GIF200 EELS detector.

4.3 Results

4.3.1 In-situ XRD

The x-ray diffraction patterns at crucial points throughout the reaction are provided in **Figure 4.1** with labels pointing out the representative peaks that were tracked to monitor the growth of each phase (details in **Table 4.1**). The integrated areas of these peaks were calculated and plotted alongside the reaction temperature in **Figure 4.2** and **Figure 4.3** as a function of time to show how each phase grew during the reaction. The times for the diffraction and temperature data were shifted such that t=0 is defined as the ignition point. The rapid reaction is thought to be enabled by the mixing of Zr into molten Al so the time at which the amorphous phase appears is defined as the ignition point in the XRD data, and a small discontinuity in the heating rate corresponding to the melting of Al is defined as the ignition point in the temperature data. It is important to note that the integrated intensities are normalized to scale from 0-100 (min to max) and therefore illustrate how each individual phase grows but do not offer a quantitative comparison between the various phases.

The development of phases during the first 135 ms of the reaction is illustrated in **Figure 4.2**. The Al_3Zr_2 intermetallic phase forms very rapidly, and is already present in the first frame at t=0 ms. The temperature quickly spikes to its maximum of 1590 °C, just 5 ms after ignition occurs. Next, the orthorhombic ZrO_2 phase appears in the second frame of the XRD data, which was collected at t=30 ms. It should be noted, though, that there is a 30 ms integration time between frames and so this phase could have developed at any point between the first frame (t=0 ms) and the second frame (t=30 ms). The

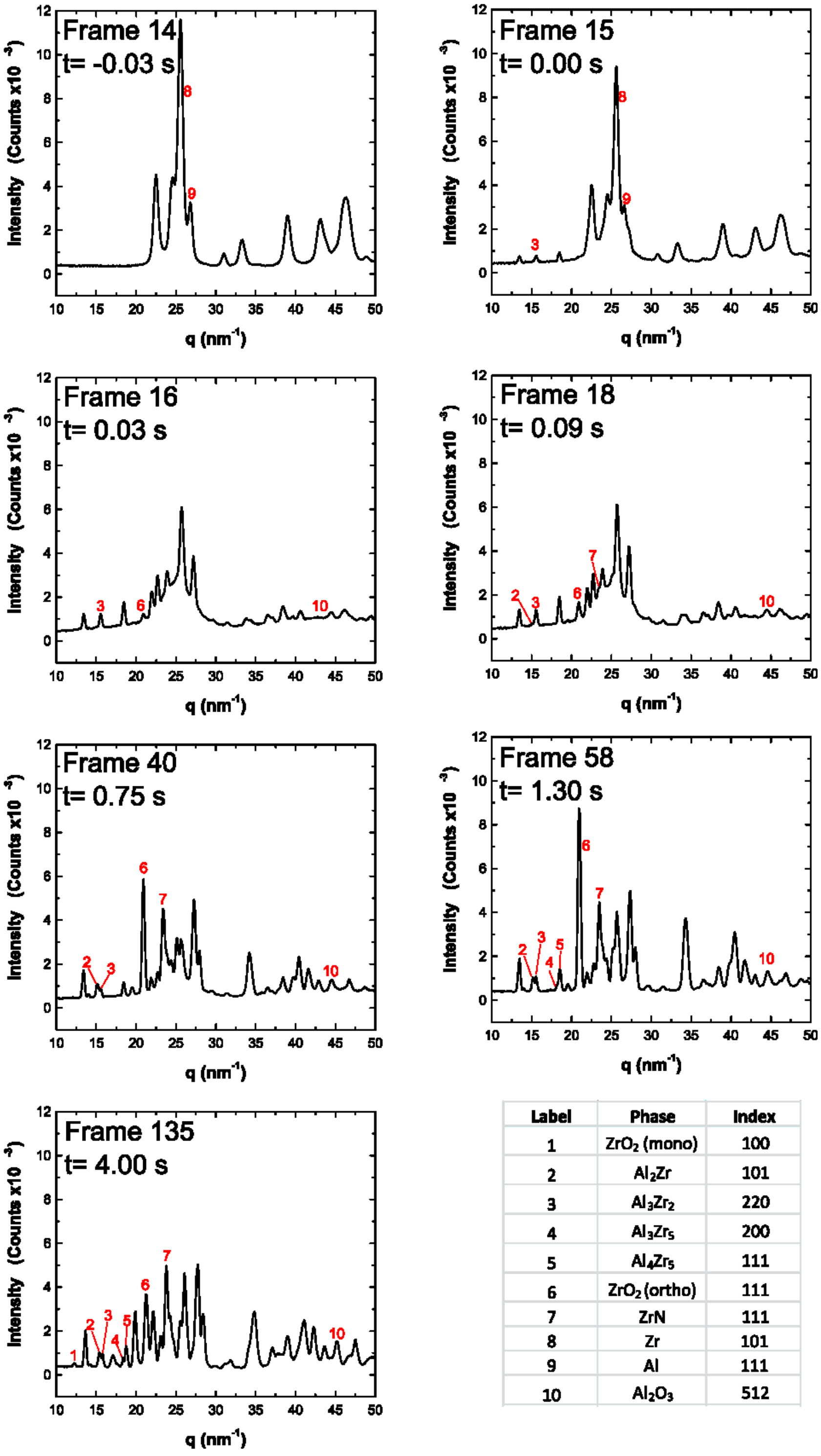

Label	Phase	Index
1	ZrO_2 (mono)	100
2	Al_2Zr	101
3	Al_3Zr_2	220
4	Al_3Zr_5	200
5	Al_4Zr_5	111
6	ZrO_2 (ortho)	111
7	ZrN	111
8	Zr	101
9	Al	111
10	Al_2O_3	512

Figure 4.1: A series of 2D diffraction patterns showing the sizes and relative positions of the peaks chosen to represent each phase.

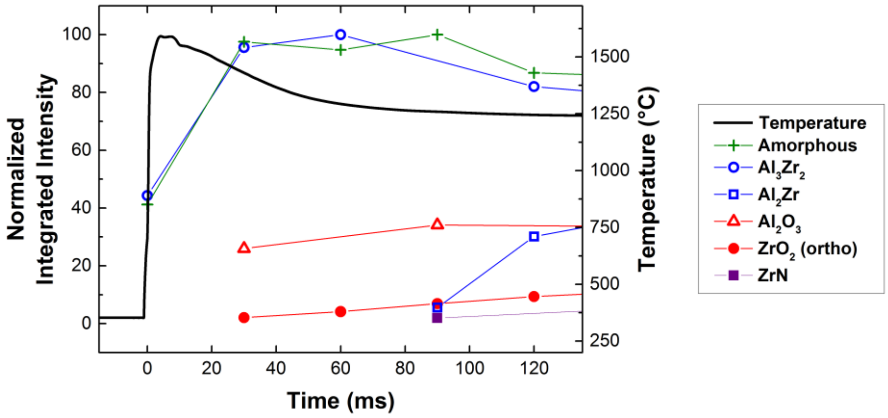

Figure 4.2: Early-time reaction progression. The ignition point is defined as t=0, corresponding to the melting of Al in the temperature data, and the appearance of an amorphous peak in the XRD data.

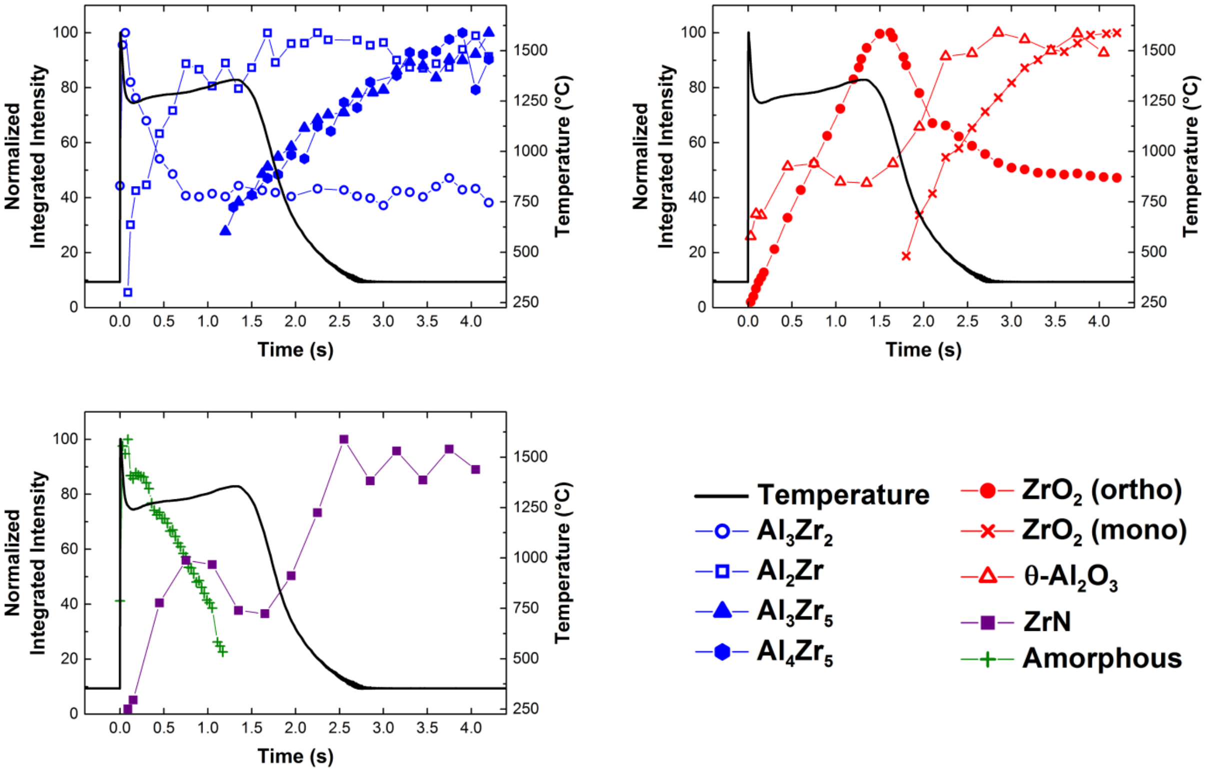

Figure 4.3: The progression of each phase throughout the reaction, shown as the normalized integrated diffraction peak area. The foil temperature, as measured by pyrometry, is included to show the correlation between reaction stage and phase development.

pyrometry data, however, is much more rapid, with a data point collected every 20 μs. The next intermetallic phase, Al_2Zr, appears at t=90 ms.

Figure 4.3 provides the overall growth for each phase observed. For clarity, the ten phases were separated into intermetallics, oxides, and then ZrN and the amorphous phases. These groups correspond to **Figure 4.3a**, **b**, and **c**, respectively. While the Al-rich intermetallics begin forming very early in the reaction, the Zr-rich intermetallics, Al_3Zr_5 and Al_4Zr_5, do not begin to form until combustion is ending at t=1.2 and t=1.3, respectively, and then continue to grow throughout the rest of the reaction. The amount of orthorhombic ZrO_2 begins to decline at t=1.6 s, and monoclinic ZrO_2 begins to form at t=1.8 s, indicating that the metastable orthorhombic phase is transforming into the more stable monoclinic polymorph. The most significant finding, however, is that the orthorhombic ZrO_2 grows linearly with time until it starts to slow at t=1.3 s, corresponding with the point at which the temperature begins its decline as the combustion stage terminates. The significance of these results, and others, will be discussed below in the context of the proposed reaction mechanism.

4.3.2 Product Analysis via Microscopy

We can begin to understand the progression of these phases by examining the elemental composition throughout a foil cross-section. This information was obtained in a previous study of the same foils, analyzed using an electron microprobe [17]. This micrograph is reproduced in **Figure 4.4** and shows that there is a thin, nearly pure ZrO_2 layer on the outer surfaces of the foil, followed by a mixed-oxide phase, and then an

Al_2Zr intermetallic region below. The center of the foil contains large crystals of the Al-rich phase, Al_3Zr_2, within a matrix of two Zr-rich phases, Al_3Zr_5 and Al_4Zr_5.

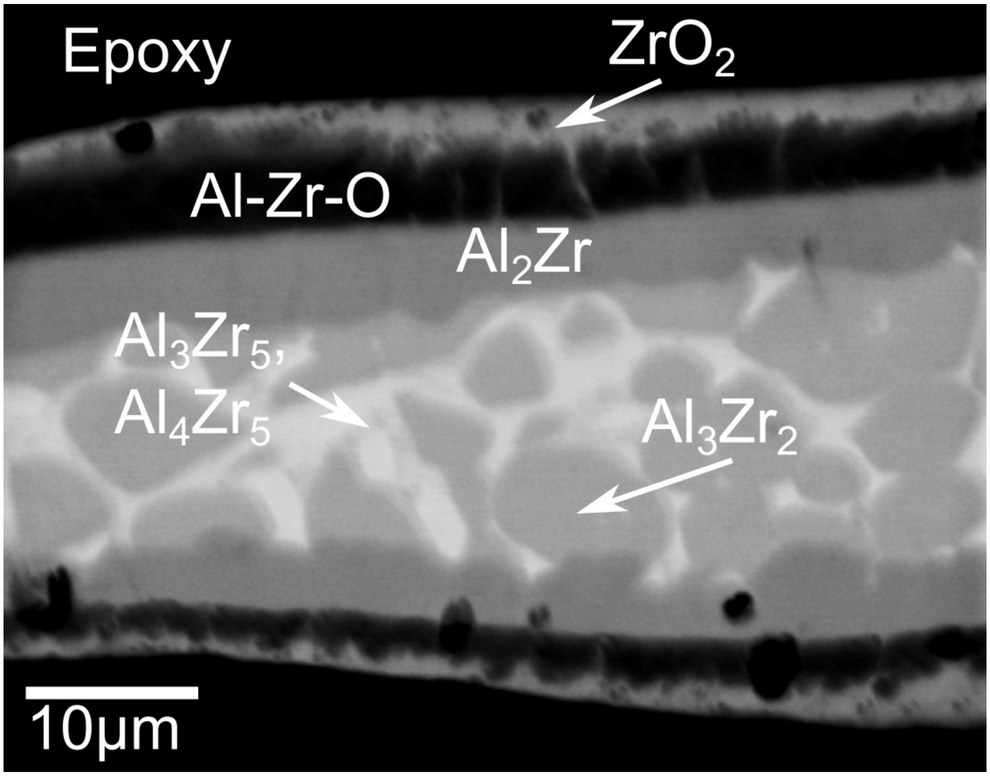

Figure 4.4: A cross-section of a 30 μm thick Al:Zr foil after it was reacted in air, analyzed with an electron microprobe. Reproduced from reference [17].

TEM was used to investigate the oxide/intermetallic interface in greater detail, and is presented in **Figure 4.5**. We have found that the interface between the Al/Zr/O mixed oxide and the Al_2Zr intermetallic layers consists of a very thin amorphous zone approximately 30 nm thick that contains oxygen and approximately 1.8× more aluminum than zirconium, which is only slightly less Al than is present in the Al_2Zr intermetallic. A more detailed micrograph of this interfacial region, represented by Zone 1, is shown in **Figure 4.5b**.

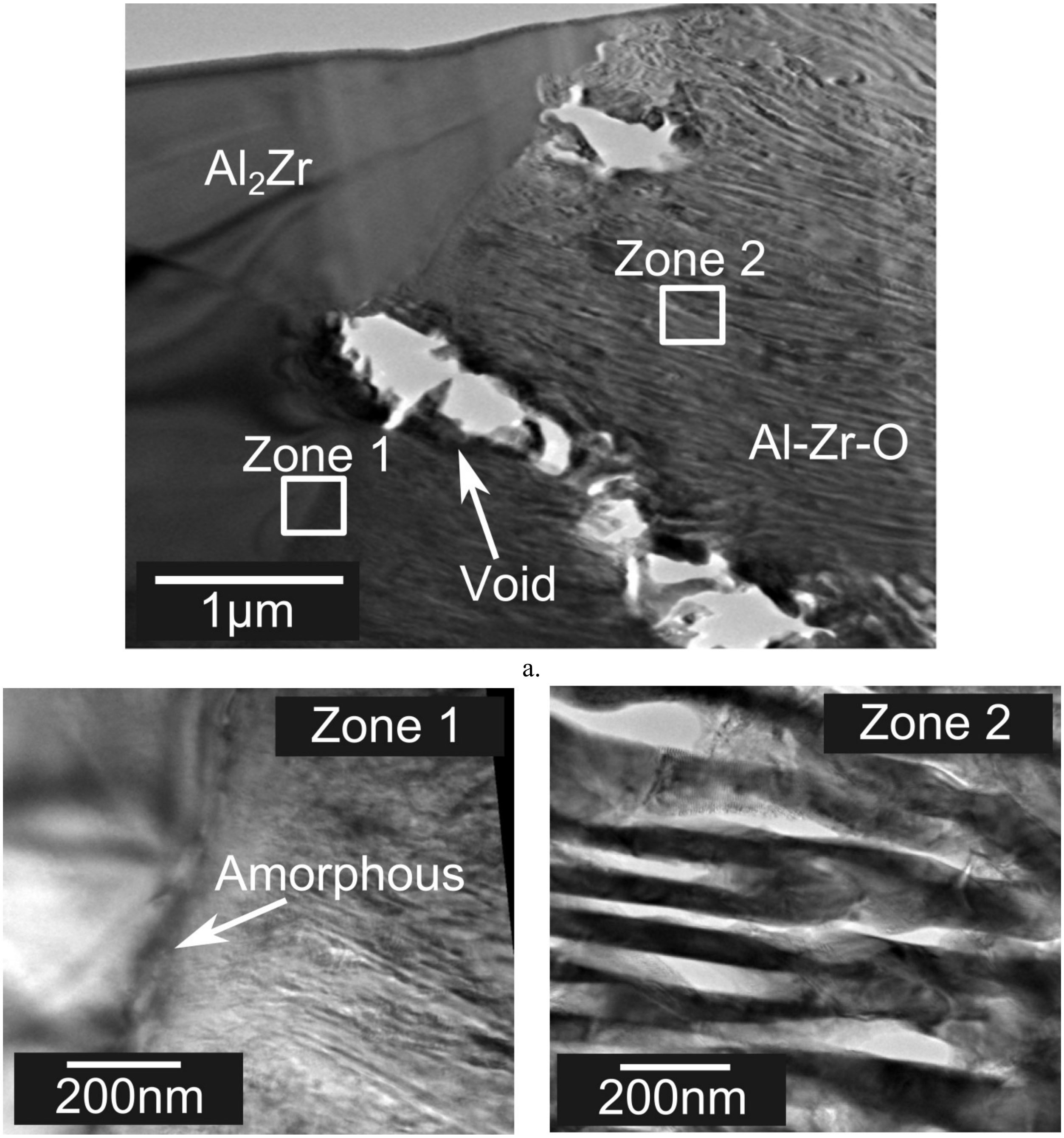

a.

b.

c.

Figure 4.5: TEM images of a FIB cross-section at the interface between the oxide and intermetallic regions. Higher magnification micrographs are provided (b) at the interface (Zone 1), and (c) within the mixed-oxide region (Zone 2).

A second high magnification micrograph, provided in **Figure 4.5c**, displays the lamellar structure that forms within the mixed oxide regions represented by Zone 2. This mixed oxide region also has approximately 1.8× more aluminum than zirconium according to elemental analysis. The diffraction patterns suggest that this region is a mixture of θ-Al_2O_3, monoclinic ZrO_2, and cubic ZrO_2. The θ-Al_2O_3 phase is a metastable crystal structure that occurs as a transition phase between boehmite, AlO(OH), and the thermodynamically stable end product corundum, α-Al_2O_3 [116,117]. The lamellar structure is a result of columnar grains growing perpendicular to the interface. The grains are smaller towards the amorphous boundary, and larger towards the outer oxide layer, which is reasonable considering that these larger grains formed earlier in the reaction and therefore had more time at high temperatures to grow. Finally, the surface oxide layer contains no Al, and is composed of monoclinic ZrO_2 and a superstructure of monoclinic ZrO_2 with a doubling of the c-axis that likely forms as a result of rapid cooling.

4.4 Discussion

4.4.1 Growth of the Orthorhombic ZrO_2 Phase

As mentioned above, the most significant result of the XRD data presented in **Figure 4.3** is the linear growth rate of the orthorhombic ZrO_2 phase, followed by a precipitous decline in temperature coinciding with a transition to a slower growth rate of ZrO_2. **Figure 4.6** emphasizes this relationship by comparing the first derivative of the temperature and the derivative of the integrated area of the orthorhombic ZrO_2 phase throughout the first 1.8 seconds of the reaction. The primary goal of this study was to understand why combustion terminates before the entire foil is completely oxidized and this finding offers an explanation. The linear growth rate is evidence of interface-controlled growth, meaning that the reaction rate is limited by the speed at which the chemical conversion at the interface can take place, not by the rate of O (or Zr) diffusion. Additionally, a linear growth rate means that the reaction rate is constant with time, which helps us understand why the reaction temperatures are relatively constant for the first 1.3 s of combustion.

Reaction temperature is thought to be determined by both the rate at which heat is produced by combustion and the rate at which heat is lost to the surrounding environment, mainly by radiation in this case [17]. A constant reaction temperature implies a constant rate of combustion because the rate of heat loss, which scales with T^4, should also be constant assuming the emissivity is stable. Interface controlled combustion can yield a steady rate of heat production at a given temperature. However, diffusion controlled combustion cannot because the rate of combustion will decrease as the growing oxide phase thickens. This leads to a drop in temperature to establish a new power balance, which in turn lowers the rate of combustion. This negative feedback loop leads to a very sharp decline in temperature. Thus, the transition from interface to diffusion controlled combustion process naturally leads to a decreasing temperature profile, as evidenced in **Figure 4.6** where the transition in growth rate coincides with the sudden drop in temperature observed at t=1.3 s.

This result compares favorably with a computational model developed in collaboration with Dr. Manav Vohra presented in reference [113]. This model used equations describing the growth of ZrO_2 layers on the surfaces of 40 μm thick Al:Zr foils that are nominally identical to those used in the XRD experiments. Equations were developed for both diffusion controlled growth and interface controlled growth. The overall rate was set equal to the lower of the two growth rate mechanisms at each point in time. An emissivity value in the range of 0.1-0.2 leads to the best fit to the experimental data, which agrees with the experimental emissivity used in this work (0.17). The model supports that based on the diffusion rates and enthalpies of combustion, a transition from interface controlled growth to diffusion controlled growth occurs before 1.6 s which matches the experimental data reasonably well.

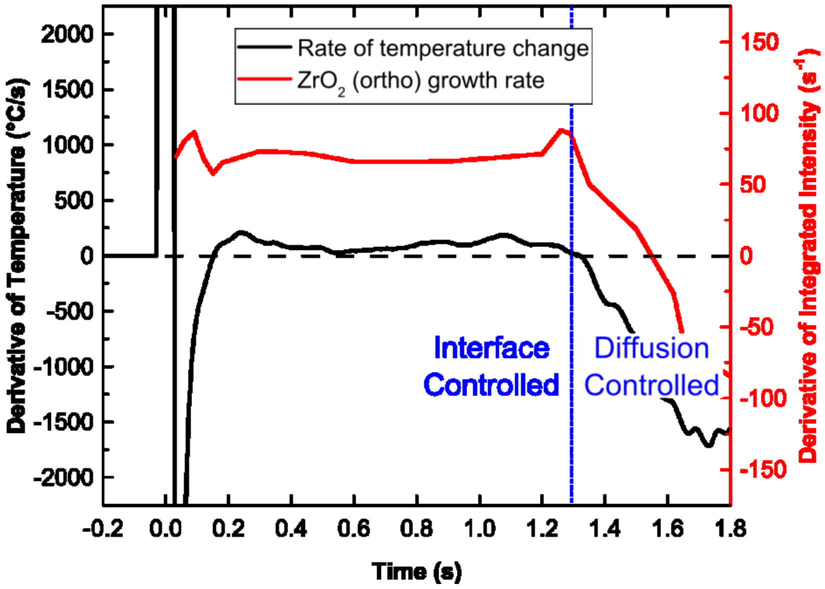

Figure 4.6: The derivatives of temperature and integrated peak intensity for orthorhombic ZrO_2. This plot emphasizes the link between the ZrO_2 growth rate and temperature. Combustion takes place during the linear oxide growth rate (interface controlled growth), and terminates shortly after the oxide growth rate begins decreasing (diffusion controlled growth).

4.4.2 Growth of the Intermetallic Phases

The Al-Zr phase diagram offers a great deal of information when combined with the pyrometry and XRD data in **Figure 4.3** and **Figure 4.2**. A reproduction of the phase diagram from reference [89] has been modified in **Figure 4.7** to show how the equilibrium thermodynamics associated with the diagram correlate with the pyrometry and XRD data. The horizontal bars indicate the minimum and maximum temperatures reached during combustion, and the positions of the red dots indicate the temperatures at which the corresponding phases first appeared. These values are provided in the legend, along with the time at which the phases appeared.

First, it should be pointed out that according to the measured foil compositions in [43], the Al:Zr foils are slightly aluminum rich with an overall Al to Zr ratio of 56 : 44. The Al_3Zr_2 phase is the first to form likely because of the two intermetallics closest in composition to the overall foil composition, AlZr and Al_3Zr_2, the Al_3Zr_2 phase has the higher melting point and is more stable during the rapid increase in temperature following mixing. The AlZr intermetallic is not detected when the foil begins to cool because by this point, the components have separated into distinct Zr-rich and Al-rich regions.

The Al_3Zr_2 phase crystallizes very rapidly, appearing in the first frame where the amorphous peak is first observed, which is defined as the ignition point (t=0). Because each frame has a 30 ms integration time, however, in actuality it is likely that this frame was recorded a few milliseconds after the reaction begins, based on the fact that both are already at 40% of their maximum intensity at this point. This definition of the ignition point generally serves as a good approximation because the difference of a few milliseconds is negligible for a reaction that lasts for ≈4 s. The only failing is in attempting to determine the temperature at which this early phase forms, since the temperature increases at a rate of $\approx 7\times10^5$ K/s during this brief period and a few milliseconds have a significant impact on temperature. Because we do not have the temporal resolution to determine a more accurate value and the Al_3Zr_2 phase is stable across a broad range of temperatures, we shall simply say that it crystallizes within the first few milliseconds of the reaction when the temperature is between the foil ignition point at 708 °C and the melting point of Al_3Zr_2 at 1590 °C.

Al_2Zr forms shortly afterwards at t=90 ms. This progression is logical because the oxidation of Zr to form monoclinic ZrO_2 begins at t=30 ms, and the Al diffuses inwards as Zr is selectively oxidized [114]. This would cause Al-rich zones to form under the oxide, and explains why this Al-rich intermetallic forms second. Its high melting temperature would also promote its formation.

No new intermetallics appear until Al_3Zr_5 crystals develop 1.2 s into the reaction, just as the orthorhombic ZrO_2 integrated peak area and temperature both start to decline when the foil begins to cool. At this point, the temperature of the foil is at 1348 °C and is still increasing. The Al_4Zr_5 phases begin to form shortly after at t=1.3 s when the temperature has peaked at 1355 °C. The fact that both Zr-rich phases start to grow almost simultaneously right as the foil begins to cool may be very telling. It indicates that not enough oxygen is available to form oxides within the amorphous interior of the foil, and the Zr-rich regions that are present form intermetallics instead.

Another intermetallic phase that might be expected but was not observed is the Al_2Zr_3 intermetallic. The compounds to the immediate right and left of it are both present, but it is possible that Al_2Zr_3 does not form simply because it possesses the least stable structure. Al_2Zr_3 has a $P4_2/mnm$ structure [118], while Al_4Zr_5 and Al_3Zr_5 are both $P6_3/mcm$ [119]. Typically, a crystallographic structure becomes harder to form as

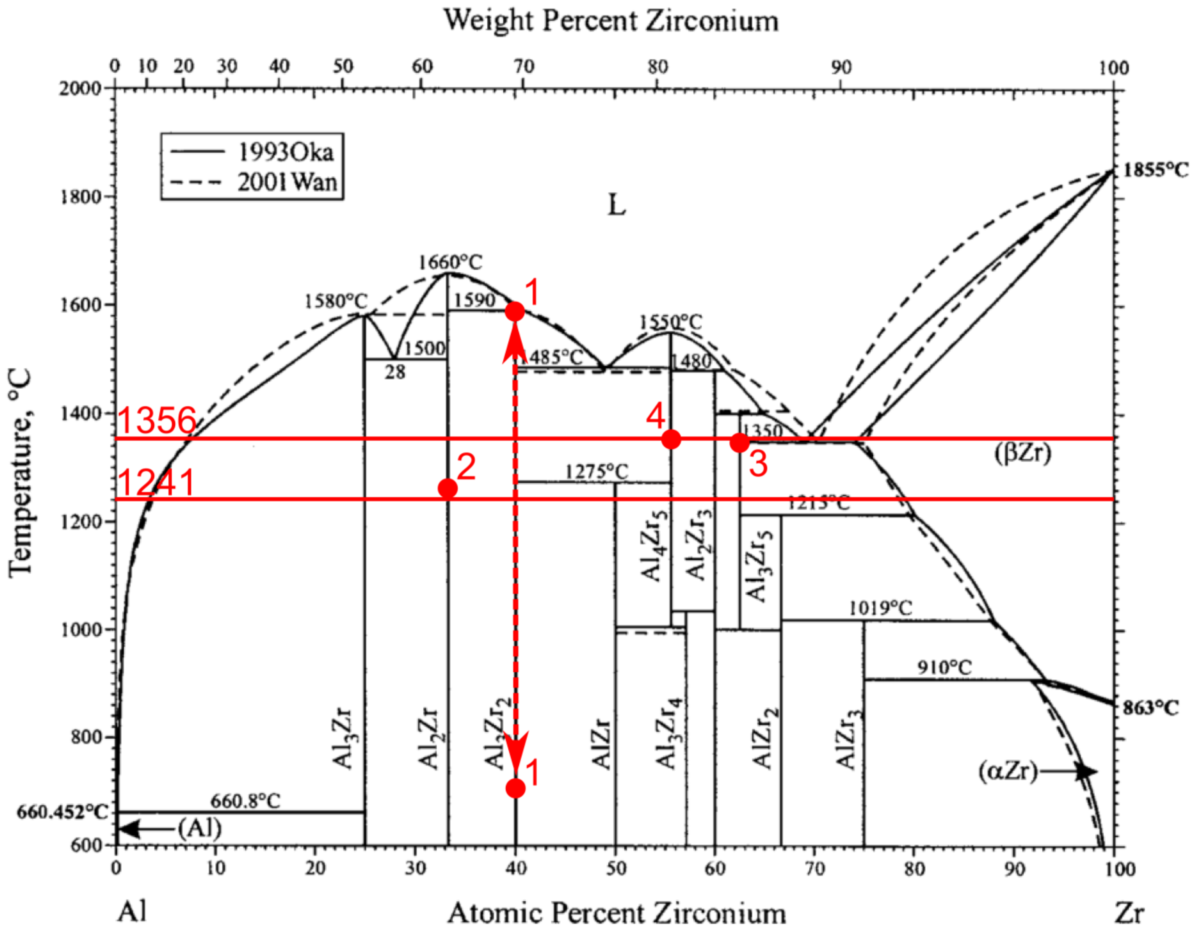

Legend

1	Al_3Zr_2	t≈0 ms	T=708 °C – 1590 °C
2	Al_2Zr	t=90 ms	T=1259 °C
3	Al_3Zr_5	t=1.2 s	T=1348 °C
4	Al_4Zr_5	t=1.3 s	T=1355 °C

Figure 4.7: The Al-Zr phase diagram reproduced from [89] and modified to show which phases were found in the XRD data. The numbering corresponds to the order in which they appeared, and the placement of the red dot for each indicates the composition and the temperature at which it was first observed.

symmetry decreases and the volume of its unit cell increases, both of which apply to Al_2Zr_3 in comparison to its neighboring phases.

4.4.3 A Combined Reaction Mechanism

Before developing our own mechanism to describe why our materials undergo this important switch from interface controlled to diffusion controlled growth of ZrO_2, it is helpful to review the body of work by Paljević [114,120–126] in which researchers measured the oxidation of various Al/Zr intermetallics at high temperatures. They report that orthorhombic ZrO_2 is a metastable structure that reverts to the monoclinic polymorph, and that this oxide layer grows by the vacancy diffusion of oxygen to the interface between the surface ZrO_2 layer and the intermetallic core. This diffusion is assisted by the ZrO_2 layer being doped with Al because replacing Zr^{4+} cations with Al^{3+} cations causes oxygen vacancies to form. They also found that the combustion of an Al_3Zr_2 intermetallic occurs by Al diffusing away from the surface, which leads to Al_2Zr forming in the now Al-rich matrix. This is based on the Wagner theory of selective oxidation, where the more noble metal (Al) escapes oxidation by diffusing into the bulk, leaving the less noble (Zr) atoms to selectively oxidize. They did not observe the formation of Al_2O_3 except in intermetallics that start very Al-rich (Al_3Zr). For Al_2Zr intermetallics, they found that oxidation proceeds logarithmically, rapidly forming a thin oxide film and then it abruptly decreases and terminates. They attribute this to there being so much Al that it cannot diffuse quickly enough into the bulk once the Zr is locally unavailable for oxidation.

The mechanisms proposed in that body of work apply well to the phenomena we have observed in our own experiments, and are in agreement with experimental and computational work regarding the oxidation of pure Zr [127,128]. It is possible to piece together a mechanism by which the reaction must proceed by combining our own results with the mechanisms witnessed in similar studies. A schematic of this proposed mechanism is given in **Figure 4.8**.

(A) We begin with an unreacted bilayer structure of Al and Zr, which upon ignition (B), rapidly mixes and forms an amorphous Al/Zr solution and Al_3Zr_2 crystals. (C) By the next frame recorded, occurring at t = 0.03 seconds, orthorhombic ZrO_2 crystals have begun to form at the external surfaces. Zr from the amorphous matrix diffuses to these surfaces because Zr oxidizes preferentially over the Al [108], though a small amount of metastable θ-Al_2O_3 also forms at this time as well.

(D) The orthorhombic ZrO_2 phase continues to grow, rejecting Al and causing an increase in Al concentration just below the oxide layers. By 0.09 s after ignition, Al_2Zr crystals form in the Al-rich amorphous zones underneath the ZrO_2 crystals. A small amount of ZrN also begins to form at this point because although it is less thermodynamically favorable than an oxide, the larger amount of nitrogen available to react in the environment makes it kinetically likely. (E) The Al_2Zr and ZrO_2 phases continue to grow and form continuous layers by t=0.75 s. While the Al_2Zr phase has been growing during this time, the Al_3Zr_2 phase has been simultaneously decreasing, implying that the rapidly formed Al_3Zr_2 is being converted to Al_2Zr. Because the Al_2Zr phase is now a continuous layer beneath the surface oxide, it is more difficult for Al to diffuse into the bulk [114]. This forces the Al to begin to oxidize in addition to the Zr, forming a mixed oxide region. **Figure 4.5b** shows that the interface between the Al_2Zr and mixed oxide zone is amorphous, but **Figure 4.5c** shows that away from the interface, the oxides have separated into a lamellar structure. This indicates that the conversion to a mixed oxide occurs in an amorphous state, but Al_2O_3 and ZrO_2 are immiscible [129] and phase separate rapidly as the interface moves past.

(F) By t=1.3 s the mixed oxide layer has become so thick that the kinetics of oxidation become limited by the diffusion of oxygen atoms to the interface with the intermetallic. The diffusion of oxygen through Al_2O_3 is much slower than the diffusion of oxygen through ZrO_2, with diffusivities of $\approx 1 \times 10^{-19}$ cm^2/s and 1×10^{-6} cm^2/s respectively, both calculated at the average temperature during combustion of 1299 °C [127,130]. Although it is possible that the diffusion of Zr through the Al_2Zr intermetallic becomes rate-limiting, it is unlikely because the thickness of this layer has not increased since t=0.75 s, after which the growth of the oxide continues to be interface limited. As the combined ZrO_2 and mixed oxide layers reach a critical thickness there is a transition from a linear increase in the ZrO_2 phase indicating interface controlled growth, to a decreasing growth rate associated with diffusion-controlled growth. Also, the Zr-rich intermetallics, Al_3Zr_5 and Al_4Zr_5 begin to form at t=1.2 and t=1.3 s respectively, implying that less Zr is diffusing to the surfaces to oxidize. The decreasing oxidation rate (and therefore heating rate) causes the temperature to decrease. As the temperature decreases, diffusion slows and the oxidation rate and heat production rate drop further still. This negative feedback loop causes the temperature to swiftly drop to the point where combustion can no longer be sustained, and it extinguishes at t=1.6 s.

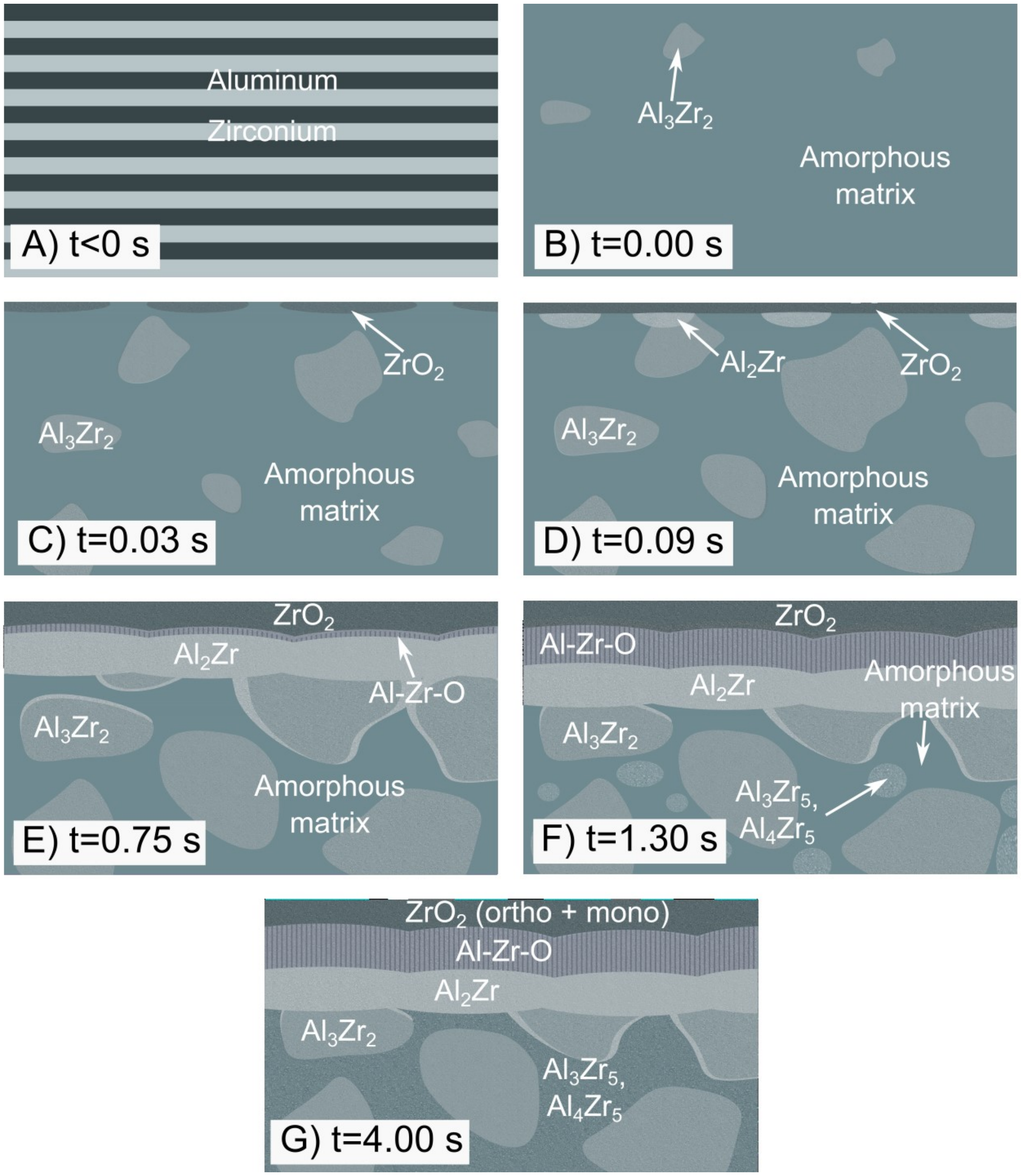

Figure 4.8: Schematic showing the phase progression within a foil cross-section. Not to scale.

(G) Beyond 2 seconds, the foil is cooling and the remaining amorphous matrix crystallizes entirely into Al_3Zr_5 and Al_4Zr_5 mixed intermetallics. An undetermined fraction of the ZrO_2 layer transforms from orthorhombic to monoclinic, ending with a mixture of both structures present in the surface oxide layer and underlying mixed oxide region.

4.5 Conclusion

Al/Zr metal fuels have been developed as additives to enhance the energy density of explosive formulations for bioagent defeat. Previous work [43] has shown that combustion terminates prematurely for these foils, however, and we must understand what causes this to occur if we are to improve their performance. This was accomplished by measuring the phase progression in situ during combustion at the Cornell High Energy Synchrotron Source, and then investigating the final structure of foil cross-sections via TEM.

The combination of these techniques allowed us to construct a mechanism by which the burning of the foil is likely to proceed. In short, ZrO_2 begins to form at the external surfaces quickly after ignition, rejecting Al into the adjacent volume. The resulting increase in Al concentration below the growing oxide leads to the formation of Al_2Zr. At 0.75 s into combustion, this Al_2Zr phase forms a continuous layer, slowing the diffusion of Al away from the oxide interface, forcing the Al to also oxidize despite being less favorable than Zr. Diffusion through Al_2O_3 is significantly slower, and so 1.2 seconds after the reaction begins, the combined thickness of the ZrO_2 and mixed oxide layers exceeds a critical threshold and diffusion of oxygen becomes rate-limiting. The transition from steady interface-controlled growth to decaying diffusion-controlled growth prevents the reaction from maintaining a constant high temperature, and combustion terminates precipitously.

With this knowledge, it may be possible to adjust the foil composition to avoid forming a continuous product layer that limits diffusion. Progress has already been made with volatile species such as Mg, which vaporize during combustion, opening pores and improving diffusion.

5 The influence of geometry on the combustion of Al:Zr and Al-8Mg:Zr nanolaminate foils

5.1 Introduction

We have shown in **Chapter 4** that for Al:Zr foils, the growth of the ZrO_2 phase begins early in the reaction and continues steadily throughout the combustion stage while the growth is interface controlled. After approximately 2 seconds, the oxide layer has thickened to the point where its growth becomes diffusion limited and combustion terminates rapidly. This mechanism has been supported by numerical simulations [113]. A corollary of having a limiting oxide thickness is that the gravimetric heat production from these foils may be expected to be a function of foil geometry. If a foil is thin, a large fraction of the metal may undergo oxidation before it becomes diffusion limited. Conversely, if a foil is thicker, the external oxide shell may constitute a smaller fraction of the volume, leaving unreacted material at the center.

We have also shown that by including Mg in the reactive nanolaminate structure, such as with Al-8Mg:Zr foils, it is possible to improve combustion efficiency [43]. The Mg creates oxygen vacancies in the ZrO_2 layer and also vaporizes readily at the temperatures reached during combustion, creating more vacancies throughout the foil. The higher vacancy concentration allows for improved diffusion of gaseous reactants through the foil and may change the mechanism observed for Al:Zr samples.

In this study, we are investigating how combustion efficiency, temperature, and duration are influenced by the thickness of Al:Zr and Al-8Mg:Zr nanolaminate foils. The nanolaminate foils serve as very uniform, model structures, and those studied here are nominally 52 mm long, 10 mm wide, and 9-60 μm thick.

Changes in thickness lead to a significant change in the surface area to volume ratio (SA/V) of the foil because it is the smallest dimension by three orders of magnitude, while changes in length or width have a negligible effect on SA/V. The surface area to volume ratio (SA/V) is an important parameter because it allows us to relate these results to other material geometries, such as particles. It is well-established that as a particle's diameter increases, the ignition temperature and burn duration also increase [131–134,84]. These effects are the result of the surface area to volume ratio (SA/V) increasing, but it is unknown, however, how the SA/V of a macroscopic foil might influence its combustion characteristics.

It is expected that changing the thickness of the foil is similar to changing the diameter of a particle and has the potential to influence combustion properties, while changing width (or length) should have minimal effect on combustion. This relationship is shown graphically in **Figure 5.1** in which calculated values for SA/V are plotted for foils as a function of width and thickness, and for spherical particles as a function of particle diameter. The functions describing each relationship are provided in the legend, where D is particle diameter, T is foil thickness, and W is foil width. The dependence of the SA/V on foil thickness is analogous to the dependence on particle diameter, but the foil width does not influence the SA/V until unphysically small widths are considered as it approaches the asymptote at 0 mm.

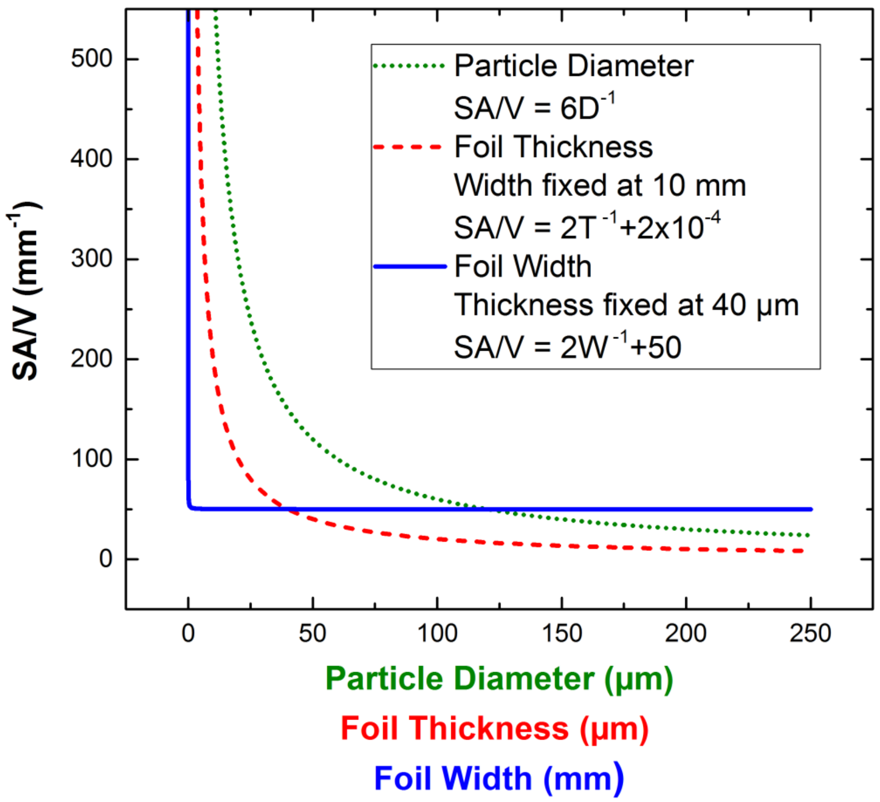

Figure 5.1: A graphical representation showing how the calculated surface area to volume ratio (SA/V) changes when a foil's width or thickness are varied, or a particle's diameter is varied. D=diameter, T=thickness, and W=width.

To perform this study, we have fabricated Al:Zr and Al-8Mg:Zr foils of varying thicknesses and measured the heat generated by each using a specially-designed combustion bomb calorimeter. We have also measured the combustion temperature and duration. Additionally, in order to explain the observed trends for combustion properties as a function of foil thickness, we have investigated the underlying mechanisms of combustion by measuring the oxygen and nitrogen content throughout the thickness of Al:Zr and Al-8Mg:Zr foils. Our goal is to develop a relationship between the foil size and the combustion properties for each type of foil (with Mg and without Mg), and understand what the underlying causes and limitations are for each, such as the diffusion of gaseous reactants (oxygen and nitrogen) towards the center of each foil. We have developed a geometric model to help us understand these relationships.

5.2 Experimental Methods

5.2.1 Fabrication: Sputter Deposition

Nanolaminate foils were sputter deposited with two different compositions: Al:Zr, and Al-8Mg:Zr. The Al:Zr foils are approximately 50 at.% Al and 50 at.% Zr. The Al-8Mg:Zr foils are 46 at.% Al, 4 at.% Mg, and 50 at.% Zr as an Al-Mg sputter target that is 92 at.% Al and 8 at.% Mg was used in place of the Al target. The Al and Al-8Mg targets were 99.99% pure, and the Zr target was 99.7% pure; all were purchased from Plasmaterials, Inc. in Livermore, CA. Foil fabrication has been explained in depth previously [43], but in short, each metal (Zr and either Al or Al-8Mg) was simultaneously magnetron sputtered onto brass substrates fixed to a rotating, water-cooled carousel. Foil width was dictated by the pattern of tape on the substrates that determines the boundaries between strips of foil, and foil thickness was adjusted by varying the deposition time. The total sputtering rate was about 1 μm/hr. The foil widths and lengths were fixed at 10 mm and 52 mm, respectively, while foil thickness was varied from 9 to 60 μm. Bilayer spacing was held constant at approximately 80 nm for all foils [41].

5.2.2 Heat of Combustion: Bomb Calorimetry

The heat generated by a combination of intermetallic formation and combustion reactions was measured in a specially designed bomb calorimeter described elsewhere [44]. It was designed to minimize heat sinking of the reacting foils, maximize surface area available for oxidation, and ignite foils with a low-energy spark. The calorimeter is extremely sensitive, with an energy equivalent of 279 ± 6 J/K, allowing for measurements on the order of just tens of Joules. Because we were interested in combustion efficiency for foils with different chemistries and geometries, heats of combustion were measured by reacting foils in 1 atm of air. In this environment, partial combustion occurs based on the kinetics associated with the foil's composition and geometry and makes it possible to assess what combination of properties may lead to improved performance.

Variations in foil thickness and hence foil mass caused the quantity of oxygen required for complete combustion to vary significantly and a bias arose during the bomb calorimetry experiments. There was excess oxygen within the chamber for smaller mass foils and so these samples could react more completely than larger mass foils, for which the chamber with 1 atm of air was an oxygen-deficient environment. We will refer to this as the "oxygen requirement bias", and we developed a rigorous correction method to subtract this bias and isolate only the influence of the foil geometry. This was accomplished by characterizing the oxygen requirement bias using foils where thickness (and therefore SA/V) was held constant but mass was varied by adjusting the foil width. **Figure 8.3** shows this data for Al:Zr (a) and Al-8Mg:Zr (b) foils, and verifications that the corrections were valid are provided in **Figure 8.4** and **Figure 8.5**. It was also hypothetically possible to avoid the oxygen requirement bias by adjusting the pressure or oxygen content of the environment for each foil. This was not a feasible approach, however, given the high degree of control over these parameters that would be necessary to account for small changes in foil mass.

5.2.3 Post-Reaction Analysis: SEM/EDS, and 3D Laser Profilometry

Foils reacted in the bomb were mounted in epoxy discs, cross-sectioned using a diamond saw, and polished to 0.25 μm with a diamond suspension. Each sample was then viewed in a Scanning Electron Microscope (SEM) using Energy-Dispersive X-Ray Spectroscopy (EDS) in order to correlate heat measured in the calorimeter with oxygen and nitrogen penetration into the foil. Foils that produced more heat per gram were expected to have greater oxygen contents, and viewing the post-reaction oxide/metal foil structure revealed how the geometry of any given foil may have influenced its combustion properties.

A Jeol 6700 SEM with an EDAX EDS detector was used for imaging in backscatter mode to provide contrast between the different phases. EDS line scans showed composition as a function of distance through the thickness of the foil, and were averaged to give a comparative estimate for total oxidation and nitridation of the sample. The average atomic percent oxygen and nitrogen values were calculated for each foil type by performing on the order of 10 SEM-EDS line scans at approximately regular intervals across the widths of the sectioned and polished foils. The oxygen and nitrogen contents were averaged across each line scan to find the average composition in that region. Then the compositions of all regions were averaged to obtain a representative value for the foils as a whole. Any slight oxidation or nitridation of the surface of the sample that might occur between polishing and loading into the SEM is expected to be negligible since the interaction depth of the EDS measurement will be much larger than the thickness of a surface contaminant layer. However, this is only a semi-quantitative technique because O and N are light elements and standardless calibration software was used. We therefore have a low confidence in the accuracy of the actual values, but the errors are consistent from sample to sample. Thus, the data is best utilized for qualitative comparisons to indicate which foils contain greater amounts of oxygen or nitrogen, and where these gaseous reactants are located within the sample.

The surfaces of Al:Zr and Al-8Mg:Zr foils reacted in air were also investigated using 3D laser profilometry, specifically with a Keyence VK-X100 series confocal laser microscope. Values for roughness and surface area per projected area (SA/A) were calculated and averaged from three different regions from a foil of each composition. Both foils had an original thickness of approximately 37 μm.

5.2.4 Burn Temperature and Duration: Pyrometry and High Speed Videography

A two-color pyrometer, designed and built in-house, was used to measure the temperature of the reacting foils. Foils were held within the ignition frame used in the bomb calorimeter, but were reacted in open air rather than enclosed within the bomb. The pyrometer functions as follows: An optic is focused onto a 1 mm diameter circle at the center of each foil, and light is channeled from the focusing optic into the pyrometer with a 600 μm fiber optic cable (Ocean Optics, Inc.). The signal is split into two equal beams using a bifurcation of the fiber as well as with a beam splitting cube for redundancy. One resulting beam is filtered at 1400 nm, the other at 1600 nm, and intensity of light at each of these wavelengths is measured using an InGaAs photodetector. The temperature is obtained from the ratio of light at these two wavelengths, based on a calibration from a blackbody source ranging from 600 K to 1200 K. All pyrometer components, unless otherwise specified, were purchased from Thorlabs, Inc. in Newton, NJ. Because the collection optic is focused on the center of the foil, we assume that the temperatures measured are at the foil surface and are not influenced heavily by adjacent hot particles or vapor.

A measurement of combustion duration could have been obtained from pyrometry data based on how long the foil remained at high temperature, but this method would be misleading because it only measures the temperatures within a 1 mm^2 circular area of the foil. A NAC Memrecam high speed camera was therefore used in tandem with the pyrometer to record each reaction and provide a more representative value for combustion duration by incorporating the entire foil. The videos were analyzed using a MATLAB program written for this purpose. The number of pixels corresponding to the combusting foil surface, after any high-temperature reshaping or particle/vapor evolution has occurred, were isolated from the background by thresholding the greyscale videos. This intensity threshold was set at 50% of the peak intensity during combustion of Al:Zr foils, and 20% of the peak intensity during combustion of Al-8Mg:Zr foils. Different threshold values were necessary because Al-8Mg:Zr foils burned much brighter and were recorded with a lower aperture setting. Any pixels above this threshold were considered to correlate with combustion. These thresholding values were determined as broad approximations that could be applied to all foils of that composition: high enough to exclude reflections from external lighting, yet low enough to include regions burning at a slightly lower temperature. The burn duration was defined as the length of time that at least half of the foil surface (50% of the pixels originally designated as combusting) remained above the intensity thresholds that were attributed to combustion. This method accounted for global foil behavior, and provided normalization such that foils of the same composition could be compared.

5.3 Results

5.3.1 Heat of Combustion

Heats of reaction measured for 10 mm wide Al:Zr and Al-8Mg:Zr foils are plotted in **Figure 5.2** as a function of foil thickness. This data has been corrected for the oxygen requirement bias that arises as mass changes, as discussed in the Experimental Methods. Measurements were also performed in Ar environments to show that the heats measured in air are well above the heats produced by the intermetallic formation reactions alone (≈0.7 kJ/g), and that the intermetallic formation reactions go to completion regardless of the foil geometry. The heats measured in air are significantly lower than the theoretical maximum heats of combustion for Al:Zr and Al-8Mg:Zr foils (≈16.3 kJ/g). This suggests that only partial combustion is occurring, as is expected in 1 atm of air. The heat output from Al:Zr samples decreases significantly as foil thicknesses increases, from 6.39 ± 0.28 kJ/g at 9 μm thick, down to 4.51 ± 0.02 kJ/g at 59 μm thick. This inverse dependence of heat production upon foil thickness is very similar to the trend for the SA/V, as shown in **Figure 5.1.** Heat from Al-8Mg:Zr foils, however, seems to be unaffected by the foil geometry, maintaining an average output of 6.45 ± 0.25 kJ/g across the entire range of thicknesses tested. This suggests that the measured heat is strongly dependent upon SA/V for Al:Zr foils, but not for Al-8Mg:Zr foils.

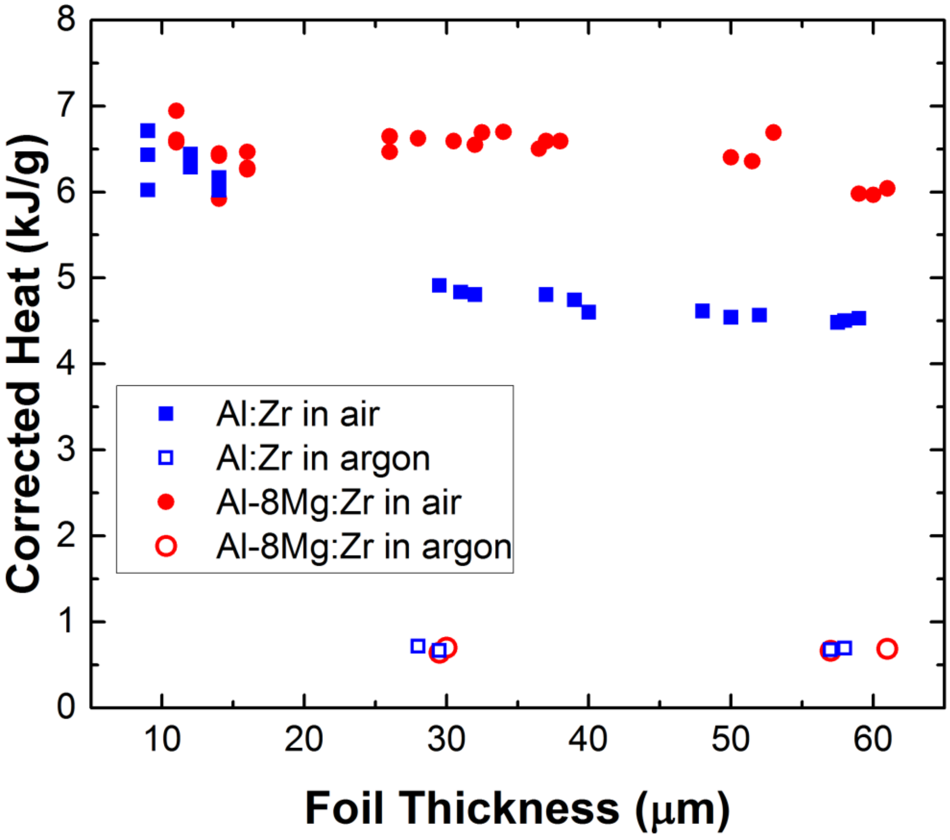

Figure 5.2: The heats of partial combustion of Al:Zr and Al-8Mg:Zr foils. Data was collected using bomb calorimetry in 1 atm of air and a correction was applied to remove the "oxygen requirement bias". Data was also collected in 1 atm of argon, in which only the intermetallic formation reactions occur.

5.3.2 Post-Reaction Composition and Microstructure

Following combustion in air, the average atomic percent oxygen and nitrogen were determined by performing SEM-EDS on representative thin and thick foils of both compositions. The averaged values are listed in **Table 5.1**. The oxygen content within the thin Al-8Mg:Zr foil is within the error of its thicker counterpart, but the thin Al:Zr foil has significantly more oxygen than the thick Al:Zr foil. There is a similar trend for the nitrogen content; the thin and thick Al-8Mg:Zr foils have approximately equal nitrogen contents, but the thin Al:Zr foil has a higher nitrogen content than its thicker counterpart. The standard deviation is large for thin foils of either sample composition because these foils undergo severe reshaping and the oxygen content in particular is highly variable depending on the location of the scan. **Table 5.1** also includes average oxide layer thicknesses for each foil. Again, the standard deviation for thin foils is quite large, but on average, the outer oxide layer thickness does not depend significantly upon the initial foil thickness. The oxide shell is thicker for Al:Zr foils, however, in comparison to Al-8Mg:Zr foils (3.7-5.5 μm and 2.5-2.9 μm, respectively).

Composition	Initial foil thickness (μm)	Overall at.% O	Overall at.% N	Oxide layer thickness (μm)
Al:Zr	9	39.7 ± 15.7	22.0 ± 5.1	5.5 ± 3.2
Al:Zr	60	13.9 ± 2.9	11.2 ± 4.0	3.7 ± 0.8
Al-8Mg:Zr	13	23.7 ± 10.4	20.1 ± 4.3	2.9 ± 1.7
Al-8Mg:Zr	56	16.2 ± 3.2	19.0 ± 2.4	2.5 ± 0.8

Table 5.1: Average nitrogen and oxygen content for the thinnest and thickest foils of each chemistry from SEM-EDS measurements of foil cross-sections.

Representative SEM micrographs and their corresponding oxygen profiles for Al:Zr foils are shown in **Figure 5.3**. Because the images were taken using backscattered imaging, there is contrast between different phases: lighter regions are higher Z elements, and darker regions contain lower Z elements. The interior sections have dark and light speckling corresponding to different Al- or Zr-rich intermetallic phases. The thicker Al:Zr foil (**Figure 5.3a**) has a clear oxide shell approximately 5.5 ± 3.2 μm thick in which the oxygen content is quite high (roughly 55 at.%). The foil has thickened during its reaction, going from an initial 60 μm thick to a final 65 μm thick in this particular region.

The thinner Al:Zr foil (**Figure 5.3b**) seems to thicken to a much greater extent during its reaction; this particular region is nearly 45 μm thick after reaction, despite starting at only 9 μm thick before the reaction. Presumably, this thickening effect could be a result of the soft metals reshaping at high temperatures to reduce the foil's surface area. By contracting in width and length, it expands in thickness. Furthermore, the growth of lower-density oxide phases and voids may lead to significant expansion. Again, the exterior surfaces form an oxide shell, in this case with that of the bottom surface being much thicker (≈5 μm) than that of the top surface (<1 μm). Note that "bottom" and "top" refer to the image only; all foils are initially symmetric and there is no true directionality across their thicknesses. Averaging the estimated thicknesses of the top and bottom oxide layers, the overall oxide thickness on the thin, 9 μm foil is approximately 3.7 ± 0.8 μm, which is similar to the thickness of the oxide layer on the thick, 60 μm Al:Zr foil considering the large standard deviations for each.

Figure 5.4 contains the SEM images and EDS oxygen profiles for Al-8Mg:Zr foils. Foils of this composition exhibit severe fracturing and void formation because Mg vaporizes and causes the ejection of hot particles during combustion [43]. We performed line scans on paths that did not contain voids because data within the void would give rise to inconsistencies from either measuring below the focal plane or from epoxy that flowed into the voids during sample mounting. As a result, the line scans were not necessarily orthogonal to the foil surface. Similarly to the Al:Zr foils, we observe an increase of oxygen content at the external surfaces of the Al-8Mg:Zr foils. The border between the oxide and intermetallic zone is more diffuse, however, differing from the more distinct shell that was observed with Al:Zr foils. The oxide layer thicknesses are very similar for both samples (2.9 ± 1.7 µm thick and 2.5 ± 0.8 µm thick) supporting that the oxide layer thickness does not vary significantly despite large changes in the initial foil geometry.

We also see more significant thickening of Al-8Mg:Zr foils in comparison to Al:Zr foils. The thicker Al-8Mg:Zr foil (**Figure 5.4a**), started at 56 µm pre-reaction but measures approximately 100 µm thick post-reaction in the region shown. Even thicker regions are present, especially where large voids are located, but much thinner segments are present as well. In this particular sample, there also seems to be an oxide phase within the interior approximately 20 µm from the surface. The thinner foils, for which a representative image is shown in **Figure 5.4b**, are even more fragmented and porous than the thicker foils. The final foil thicknesses ranged from single microns to hundreds of microns across different areas. The representative region we have selected has locally grown to approximately triple its original thickness. The more severe foil reshaping that occurs for Al-8Mg:Zr foils is likely a result of having a slightly lower melting temperature than for Al:Zr foils due to the alloying with Mg.

The exterior surface of foils reacted in air were viewed using 3D laser profilometry, the results of which are shown in **Figure 5.5a** for an Al:Zr foil and in **Figure 5.5b** for an Al-8Mg:Zr foil. The Al:Zr foil exhibits ridges resulting from the propagation wave of the intermetallic formation reaction. The average roughness (R_a) is highly consistent; it was calculated to be exactly 2.7 µm for all three regions of the foil measured. The surface area per projected area (SA/A), or relative area, is 2.3 ± 0.1 for the Al:Zr foil. The Al-8Mg:Zr foil, however, has a much rougher surface, with an R_a of 12.3 ± 1.6 µm, and a

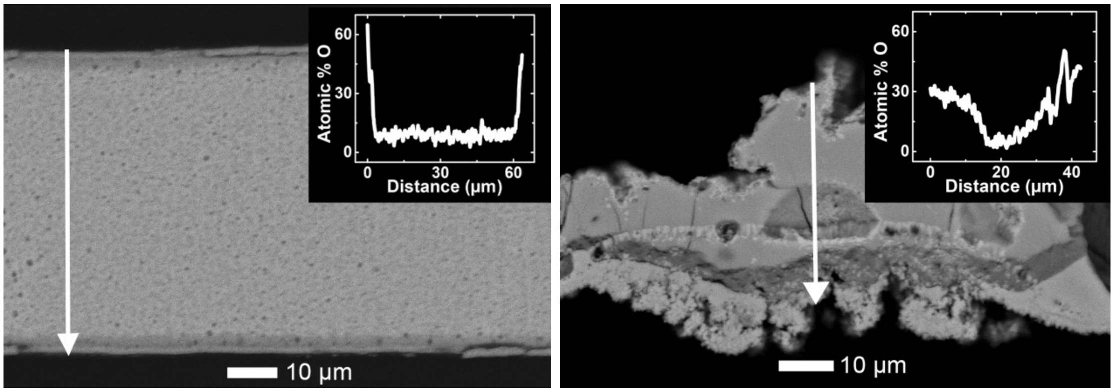

a. b.

Figure 5.3: Backscattered SEM images of Al:Zr foil cross-sections from samples that were 60 µm thick (a) and 9 µm thick (b) prior to reaction. Line scans measuring the atomic percent oxygen are provided for each to show examples of how the oxygen content may change as a function of position within the foil.

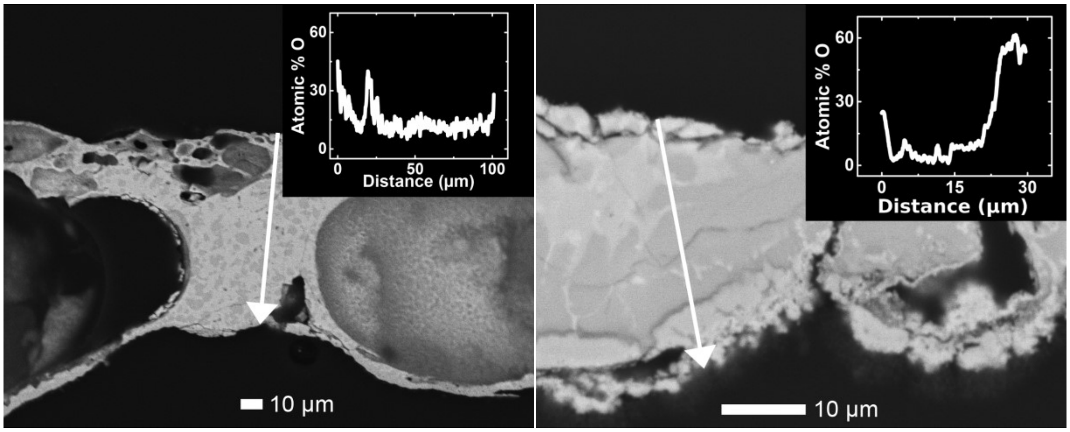

a. b.

Figure 5.4: Backscattered SEM images of Al-8Mg:Zr foil cross-sections from samples that were 56 µm thick (a) and 13 µm (b) prior to reaction. Line scans measuring the atomic percent oxygen are provided for each to show examples of how the oxygen content may change as a function of position within the foil.

SA/A of 3.9 ± 0.2. This is likely due to the porosity from material ejection that occurs for Mg-containing foils and a greater extent of oxidation [43].

5.3.3 Foil Temperature and Burn Duration

Still frames from high speed videos of the 60 µm thick Al:Zr and Al-8Mg:Zr foils reacting in air are presented in **Figure 5.6** for the first 100 ms of reaction to demonstrate the difference in behavior between Al:Zr and Al-8Mg:Zr foils immediately after ignition. Comparing the frames taken at 20 ms for the two foil types, the intermetallic formation reactions propagate more quickly in Al:Zr foils (≈3.1 m/s) than they do in the Al-8Mg:Zr foils (≈1.3 m/s). The decrease in propagation rate is likely the result of Mg lowering the thermal conductivity in the Al layers. Al-8Mg:Zr foils produce plumes of vapor immediately upon ignition and eject molten particles throughout the intermetallic formation reaction, and continue to do so for an additional ≈60 ms. The Al:Zr foils do not produce any vapor or particles. The sparks visible in the first frame (t=0 ms) are attributed to the electrical current used to ignite the foil.

Similarly, **Figure 5.7** presents still frames from the same reactions, but now focusing on the long-term reaction in order to demonstrate the different combustion durations and foil reshaping. At t=0.5 s, the Al-8Mg:Zr foil exhibits porosity that is not present in the Al:Zr foil. The sagging of the foils, particularly severe for Al-8Mg:Zr foils, indicates the reshaping of the foil due to gravity while it softens at high temperatures. Both foils cool non-uniformly, with hot and cold spots developing across the foil surface, which is why the analysis of high-speed videos with the entire foil in view offers more rigorous temporal data than pyrometry of a single point on the surface. The Al:Zr foils combust for a longer duration, with high temperature zones still present at t=2.0 s, in comparison to the Al-8Mg:Zr foils that are almost completely cool by t=1.0 s. For both **Figure 5.6** and **Figure 5.7**, the Al-8Mg:Zr foils appear darker because it was necessary to close the camera aperture more for viewing the much brighter combustion of the Mg-containing foils. The computational analysis of the videos took this into account for burn duration calculations by normalizing the intensity, as described in the Experimental Methods.

The results of the burn duration analysis from the high-speed videos are presented in **Figure 5.8a**. With a 600% increase in foil thickness, we see a 24% increase in burn duration for Al:Zr foils, going from 1.37 ± 0.07 s to 1.71 ± 0.07 s. The trend is even stronger for Al-8Mg:Zr foils, with a 42% increase in burn duration, increasing from 0.66 ± 0.04 s for 10 μm thick foils to 0.94 ± 0.06 s for 59 μm thick foils.

Another group has studied the combustion duration of Al and Al-Mg alloy particles as a function of the particle diameter [84]. Their data was fit with power law curves of the form $t=aD^n$ where t is time, a is a scaling coefficient, D is particle diameter, and n is an exponent whose value is linked to the combustion mechanism. The values of n calculated in this reference were 0.53 for pure Al, and 1.21 for Al-10Mg, which is very close in composition to the Al-8Mg used in this study. A similar study found an n value of 1.8 for the combustion duration of Zr-rich alloy particles (25 at.% Hf) [135]. The combustion of foils might also be expected to follow a similar power law fit, though with the exponent being one third of the value expected for particle combustion given that diffusion is 1D with foils and 3D with particles. However, it is not possible to determine whether or not our data correlates with these predicted power law trends because we only

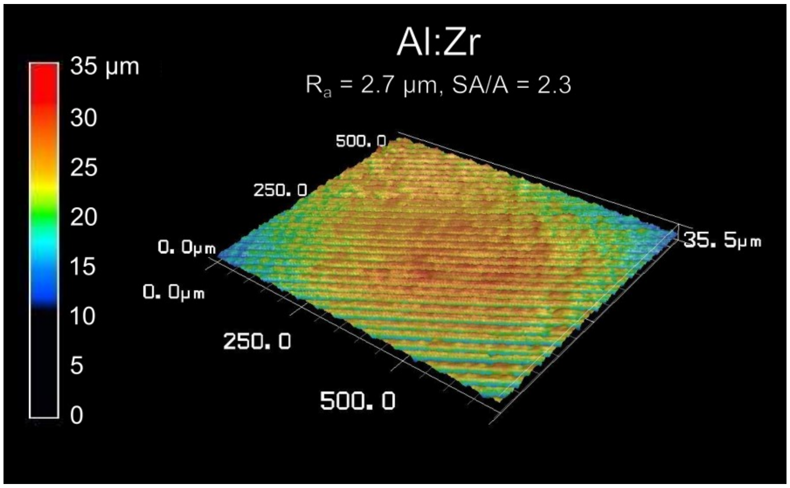

a.

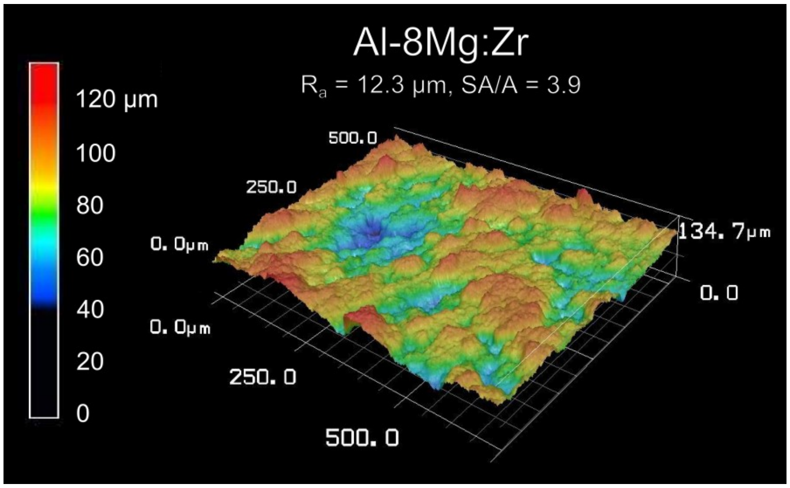

b.

Figure 5.5: 3D laser profilometry performed on 37 μm thick (a) Al:Zr and (b) Al-8Mg:Zr foils after reacting in air. The average roughness (R_a) and surface area per area (SA/A) were calculated and found to be significantly greater for Al-8Mg:Zr foils.

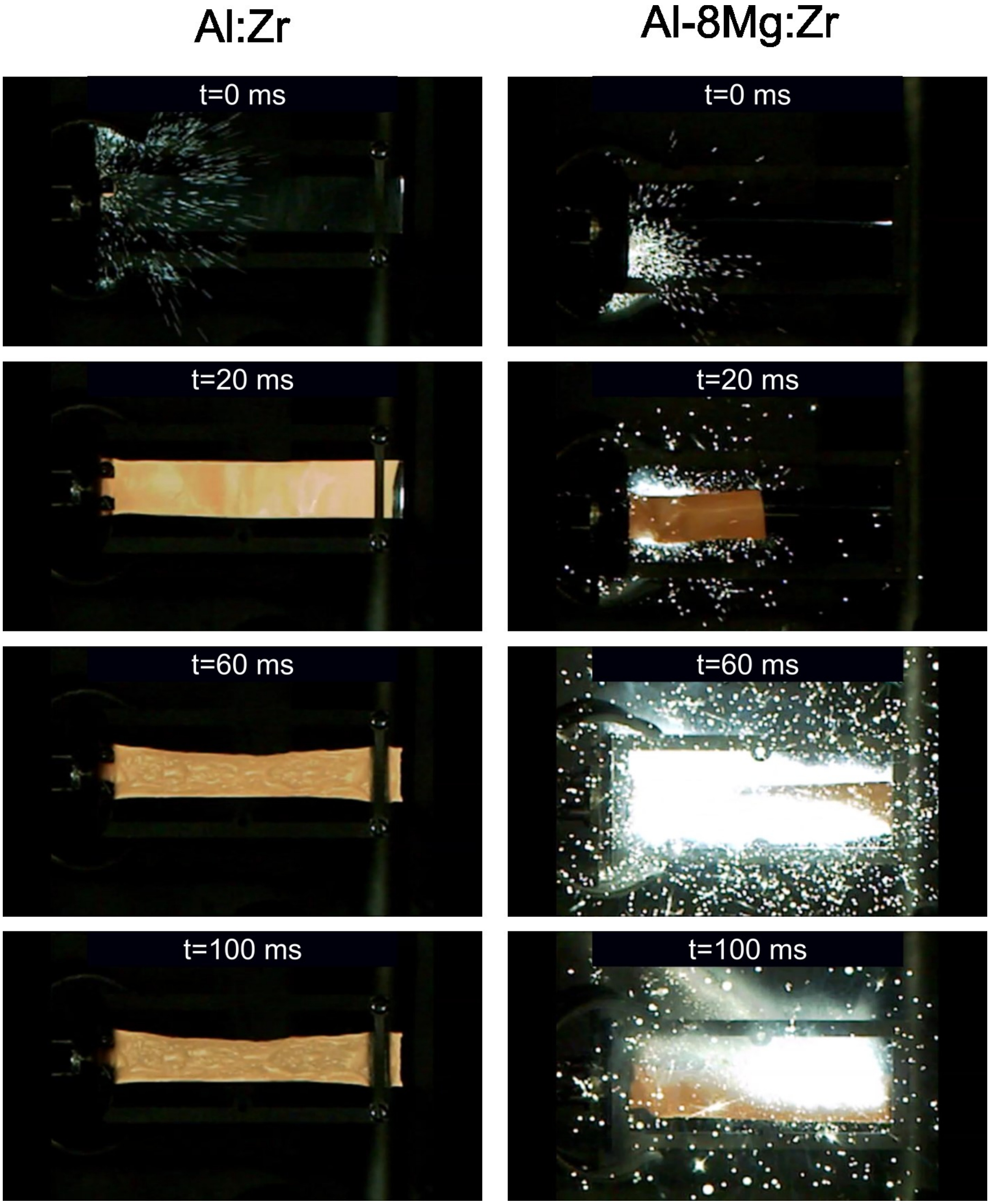

Figure 5.6: Still frames from high speed videos of 60 μm Al:Zr and Al-8Mg:Zr foils reacting in air. The time scale focuses only on the early reaction behavior, from t=0 to t=100 ms, to demonstrate that Al-8Mg:Zr foils produce a rapid burst of vapor and particles early in their reaction, while Al:Zr foils do not.

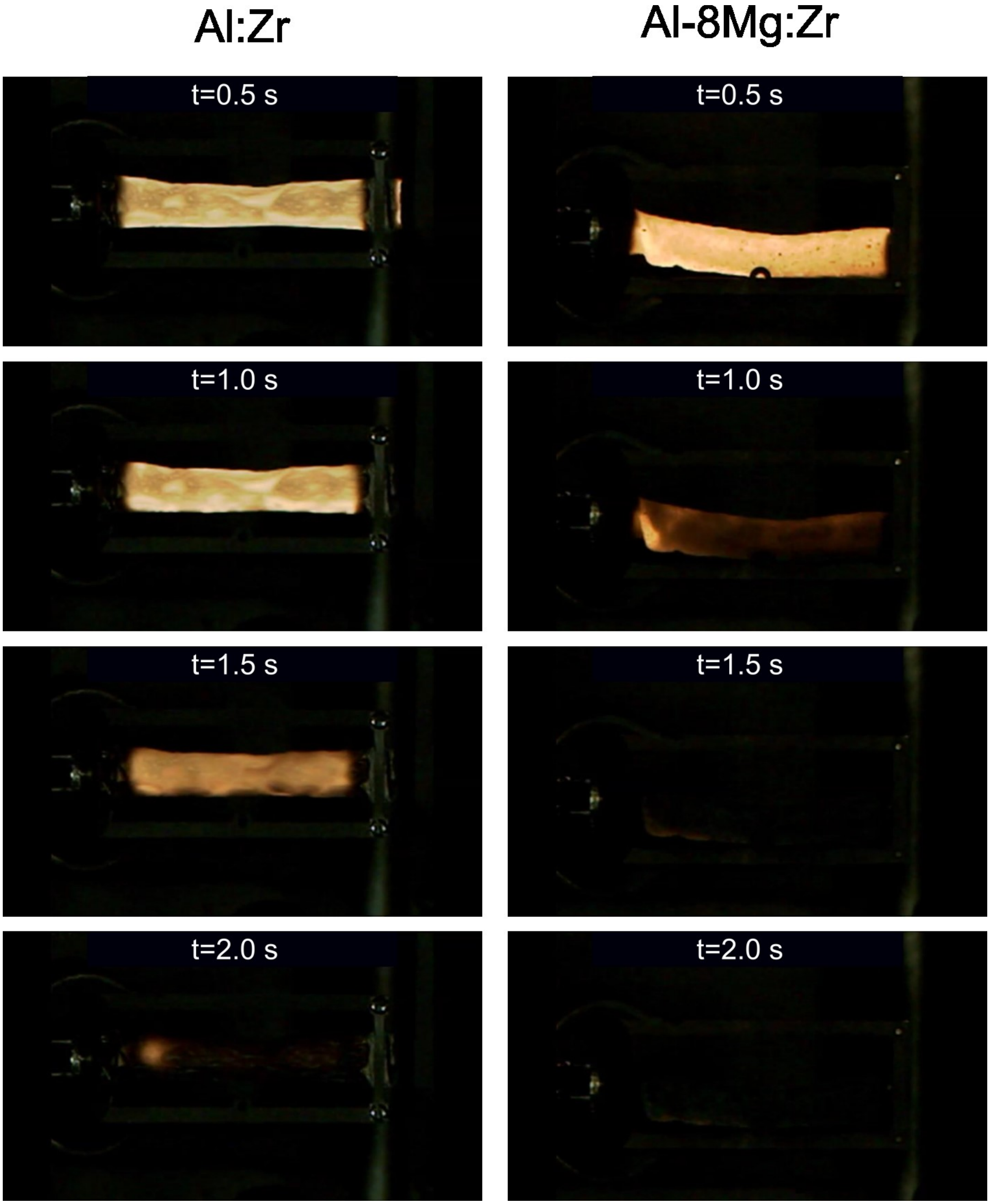

Figure 5.7: Still frames from high speed videos of 60 μm Al:Zr and Al-8Mg:Zr foils reacting in air. The time scale, from t=0.5 to t=2.0 s, encompasses the full reaction durations to demonstrate that Al:Zr foils combust significantly longer than Al-8Mg:Zr foils, and that temperature is non-uniform throughout each sample, with distinct hot and cold zones.

have two usable data points for each foil type. The thinnest foils (10 μm thick) could not be used to calculate a fit because their burn durations were artificially extended due to the edges curling during combustion, leading to reduced heat losses and longer burn durations compared to the larger thickness foils.

The reactions typically contain an initial spike in temperature resulting from the very rapid intermetallic formation reaction and a plateau in temperature that extends for 0.5 to 2 s and marks the combustion of the foil. The average temperature during this plateau region is plotted in **Figure 5.8b** versus foil thickness. The data indicates that the combustion temperature is not significantly influenced by the foil thickness. For a 6x increase in foil thickness, from 10 μm to 60 μm, we see little change in temperature for foils of either type. Across all thicknesses, the average plateau temperature is 1632 ± 77 K for all Al:Zr foils, and 1641 ± 36 K for all Al-8Mg:Zr foils. The error bars associated with the pyrometry measurements are estimated to be 5%, or ≈80 K based on our confidence in the calibration, which is larger than the standard deviations calculated for the foil temperatures across all thicknesses. For this reason, we interpret the data as showing no significant relationship between foil combustion temperature and foil thickness.

It should be noted that although Al-8Mg:Zr foils combust more brightly than Al:Zr foils do, the brightness does not necessarily indicate that these foils are at higher temperatures or produce more net heat. This will be examined in more detail in the Discussion, but in short, the Mg-containing foils are brighter despite being at the same temperature as Al:Zr foils because they have a greater emissivity. This is consistent with

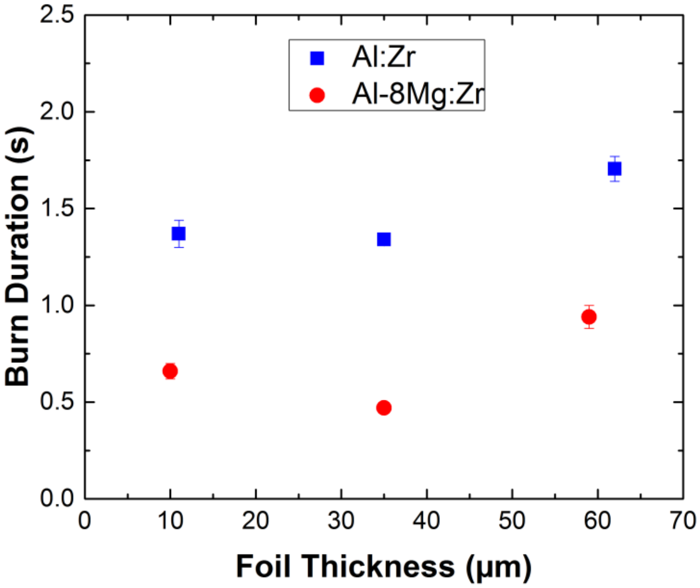

a.

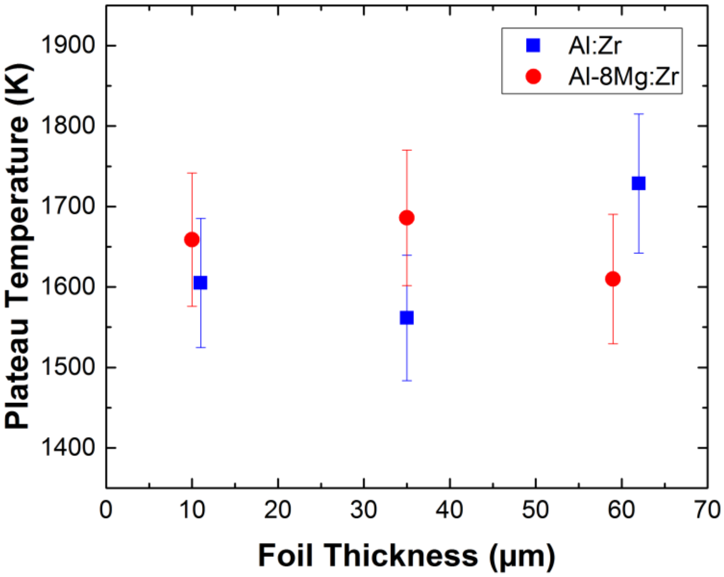

b.

Figure 5.8: a) The temperature of the combustion plateau, measured using a two-color pyrometer, and b) burn duration, measured using a high-speed camera, both as a function of foil thickness.

two-color pyrometry, where temperature is calculated using the ratio of light intensity of two wavelengths, but the net intensity is not considered.

5.4 Discussion

5.4.1 The Effect of Geometry on Combustion Behavior

The total gravimetric heat release (**Figure 5.2**) is highly dependent upon foil thickness for Al:Zr samples; it decreases by 42% as thickness increases from the thinnest foils tested (9 μm thick) to the thickest foils tested (59 μm thick). For Al-8Mg:Zr foils however, there is no significant change within approximately the same range, from 11 to 61 μm thick, over which the heat production remains a nearly constant 6.45 ± 0.25 kJ/g.

For Al:Zr foils, the oxide shell that develops at the foil exterior is well defined, and is approximately 4-5 μm thick. For Al-8Mg:Zr foils, the oxide shell is far more variable and its border is diffuse, but it does seem to be thinner than the oxide layer on the Al:Zr foils (roughly 3 μm thick). The compositional data from **Table 5.1**: Average nitrogen and oxygen content for the thinnest and thickest foils of each chemistry from SEM-EDS measurements of foil cross-sections. shows that the overall oxygen and nitrogen content decreases with Al:Zr foil thickness, but for Al-8Mg:Zr foils, the content in the thicker samples is within the (large) standard deviation of the thinner samples. This is consistent with the calorimetric measurements. Heat generation scales with the extent of oxidation and nitridation, and so we expect that the oxygen and nitrogen content for Al:Zr foils is higher for thin samples, which produce more heat per gram, and lower for thick samples, which produce less heat per gram. Similarly for Al-8Mg:Zr foils, heat output seems unaffected by the sample thickness, and the oxygen and nitrogen content does not change by a statistically significant amount either. It is important to note that the values for oxygen and nitrogen content reported in **Table 5.1** are meant only as a basis for comparison between samples; the exact values are not expected to be accurate, as discussed in the Experimental Methods. The oxygen and nitrogen contents reported are indeed unphysically high, in some cases larger than could be accounted for by complete combustion of the metal constituents.

The combustion duration scales with the foil thickness for both Al:Zr samples and Al-8Mg:Zr samples, as shown in **Figure 5.8b**. It is not a particularly sensitive relationship, though. A 6x increase in thickness only yields a 24% increase in burn duration from Al:Zr foils, and a 42% increase from Al-8Mg:Zr foils. We observed that the foil edges curl severely during the combustion of the thinnest foils of both compositions, potentially leading to the extended combustion durations that surpass that of the intermediate thickness foils. As discussed in the Results section, we are unable to develop a power law fit for the combustion duration as a function of time that would be expected for particles, due to the fact that this curling effect is not accounted for in combustion theory for particles. We can note, however, that our foils burn for much longer durations, on the scale of seconds, as might be expected for macroscopic foils combusting at lower temperatures, compared to particles that combust for milliseconds.

Since our primary goal is to control burn duration by tuning the geometry of our reactive materials with minimal loss in combustion efficiency, it is useful to plot these two metrics against each other. Heat and burn duration could not be measured simultaneously in our experimental setup because heat was measured in the enclosed bomb where it could not be viewed with the high-speed camera. By combining results from **Figure 5.2** and **Figure 5.8a**, however, we are able to obtain the heat generation as a function of combustion duration, presented in **Figure 5.9**. This plot is instructive in that it emphasizes that Al-8Mg:Zr foils combust for shorter durations than Al:Zr foils do, but release more total heat within that time. Furthermore, it demonstrates the energy cost associated with increasing the burn duration by tuning the composition and geometry of the sample. Based on the concatenated data a 100% increase in the combustion duration from 0.5 to 1 s, for example, is associated with a decrease in heat output of approximately 12%.

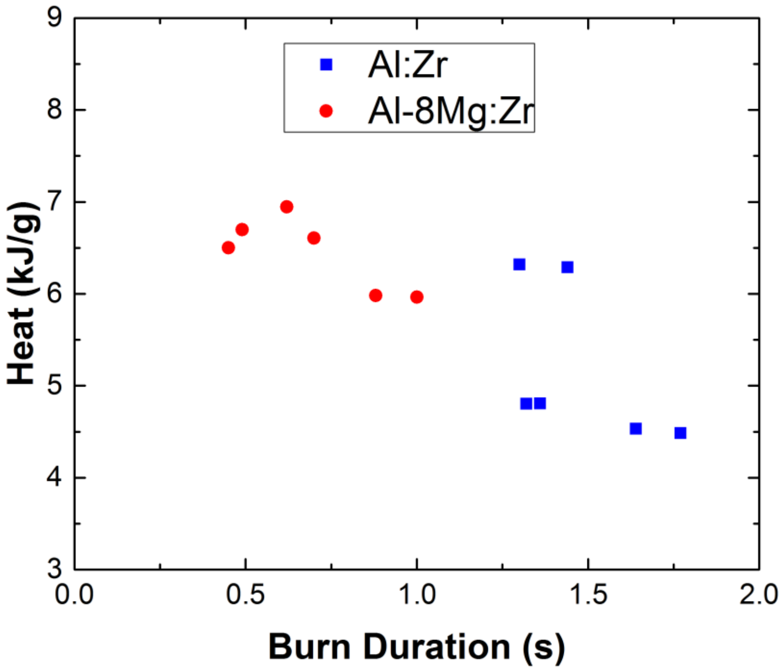

Figure 5.9: Heat production as a function of burn duration. Bomb calorimetry and high-speed video data are combined after being collected separately for nominally identical foils because both cannot be measured in a single experiment.

Unlike combustion duration, the temperature of combustion does not appear to depend on geometry (within the range tested) for either of the foil compositions, as shown in **Figure 5.8b**. Other research has shown that as the particle diameter increases for Al and Al-Mg micron-scale particles, combustion temperature increases [84], and for Zr particles, combustion temperature decreases [136]. The fact that we do not observe a significant dependence of temperature on foil thickness likely indicates that temperature trends of foils and particles are not easily compared due to the strong differences in SA/V. Although **Figure 5.1** shows that the SA/V scales similarly for the diameter of a spherical particle and the thickness of a foil, the actual values for SA/V are much higher for particles, especially at smaller diameters <30 μm. The combustion temperatures of these foils (1632 ± 77 K for all Al:Zr foils and 1641 ± 36 K for all Al-8Mg:Zr foils) are approximately half the ≈3000 K temperatures measured in on ongoing study with 35 μm diameter burning particles of the same compositions (Al:Zr and Al-8Mg:Zr).

It may seem contradictory that Al-8Mg:Zr foils combust for approximately half the duration of Al:Zr foils and produce more heat, yet combust at essentially the same temperature (1632 ± 77 K for all Al:Zr foils and 1641 ± 36 K for all Al-8Mg:Zr foils). This can be explained, however, if the higher heat generation rate is balance by a higher heat loss rate. To support this claim, it is possible to calculate the heat production per second using the total heat output and burn duration. We found that the heat production rate is approximately 160% higher for 60 μm thick Al-8Mg:Zr foils, as an example, than for Al:Zr foils of the same thickness. Because both foils have the same approximate combustion temperature of 1640 K, the cooling rate must change by a similar magnitude (increase by ≈160%) to balance the increased heating rate. Radiation is the primary cooling mechanism for these foils [17] and can be estimated using the Stefan-Boltzmann Law:

$$j^* = \varepsilon\sigma A T^4 \qquad \text{Equation 1}$$

where j^* is the total energy radiated per area per time (watts), ε is the emissivity (unit-less), σ is the Stefan-Boltzmann constant (5.67 x 10^{-8} W m^{-2} K^{-4}), and T is temperature (K). According to the results in **Figure 5.5**, the surface area of Al-8M:Zr foils is 70% higher than that of Al:Zr foils and the emissivity, though not measured, could change significantly with the 4.5x increase in roughness. Combining the potential changes in surface area and emissivity using **Equation 1**, it is feasible for the increase in radiative heat loss to balance the 160% increase in heat generation.

5.4.2 Proposing a reaction mechanism for the combustion of Al-8Mg:Zr foils

We have shown that the combustion efficiency of Al:Zr foils depends upon the foil thickness while the efficiency of Al-8Mg:Zr foil combustion does not. In order to understand why this occurs, one must consider how the reaction mechanisms may differ between these foils of different compositions.

As described in the Introduction, a related study has shown that the growth of the oxide is initially interface limited [45], which means that the condensed state flux of the gaseous reactants is faster than the rate at which atoms can rearrange to form the crystalline oxide phase. The diffusivities of oxygen and nitrogen through the intermetallics are unknown, but they can be approximated as 10^{-6} to 10^{-8} cm^2/s for Al:Zr based on values for diffusion through zirconium at our combustion temperature of 1630 K [137,138]. For Al-8Mg:Zr foils, we expect that the rate of diffusion will be significantly higher due to Mg causing the vacancy concentration to be higher than it is for Al:Zr foils. Mg introduces vacancies into the foils in two ways: cation vacancies from Mg vaporizing rapidly during the intermetallic formation reaction, and anion (oxygen) vacancies from Mg atoms within the ZrO_2 layers because they are of a lower valence (2+) than the Zr cations (4+) [108]. If we assume that each Mg atom causes a vacancy (those that vaporize all cause cation vacancies, and those that remain all dope the oxide), and the foils are 4 at.% Mg, then the vacancy concentration will increase to $4x10^{-2}$. The thermal equilibrium vacancy concentration at 1673 K was calculated to be $7.51\ x10^{-3}$ in Al, and $2.87x10^{-6}$ in Zr [139–141]. Therefore, depending on the average equilibrium concentration in Al:Zr, the addition of vacancies from Mg could likely yield an increase in vacancy concentration by 1-4 orders of magnitude. This higher vacancy concentration could in turn cause the diffusivity to also increase by the same extent if we assume the primary mechanism is vacancy diffusion [142]. This will cause more of the gaseous reactants to diffuse into the central regions of Al-8Mg:Zr foils than for Al:Zr foils, where heat is generated from forming solid solutions. If more heat is being produced in the central intermetallic solid solution region, then the Al-8Mg:Zr foils become less dependent upon the volume fraction of the surface ZrO_2 layer, and therefore less dependent upon foil thickness.

The solubility data for oxygen and nitrogen in the various intermetallics we form (Al_2Zr, Al_3Zr_5, and Al_4Zr_5) is unknown. It is possible to estimate, however, using the phase diagrams for elemental Al and Zr. For Al, the solubility limit for oxygen or nitrogen is infinitesimally small [143,144]. However, the Zr-O phase diagram [145] shows that at our temperature, crystalline Zr is expected to accept 31 at.% O into the octahedral interstitial sites of its HCP lattice before ZrO_2 will begin to form. Similarly, Zr will accept 23 at.% N before ZrN will form [146]. Because the three dominant intermetallics that form all have hexagonal crystal structures like Zr, the intermetallics may behave more similarly to Zr and have a high solubility of oxygen and nitrogen. It is therefore likely that some portion of the gaseous reactants diffuses into the bulk of the foil before their concentrations at the surfaces exceed the solubility limit and chemically combine to form the crystalline oxide and nitride end products. Because diffusion is faster in Al-8Mg:Zr foils, a larger portion of the incident oxygen and nitrogen may diffuse inward and therefore produce more heat from the internal region in comparison to Al:Zr foils.

Another important difference that we observed is that Al-8Mg:Zr foils burn for 45-65% less time than Al:Zr foils of the same thickness. The above argument might explain this phenomenon as well. Because more heat is being released by the central solid solution region, the foil consumes reactants and generates heat faster, and therefore also terminates faster. Our results indicate, however, that the oxide layer thickness in Al-8Mg:Zr foils does not grow to the thickness measured for Al:Zr foils, which is limited by the switch to diffusion-controlled growth [45]. This implies that either combustion in Al-8Mg:Zr foils does not become diffusion limited and terminates for an alternative reason, or that Al_2O_3 forms faster in these foils, causing the reactions to become diffusion limited at smaller oxide thicknesses.

5.4.3 A Simple Geometric Model of Combustion

Development of the Model

Based on experimental observations, we suggest that the zones of the foil near the external surfaces undergo severe oxidation, and zones in the central regions form solid solutions of oxygen and nitrogen in the intermetallic phases. This is presented schematically in **Figure 5.10**. It is important to note that with this simplified 2D visualization, each region of the foil is presented as an area in the cross-section, but the area fraction is equivalent to the volume fraction in a 3D foil.

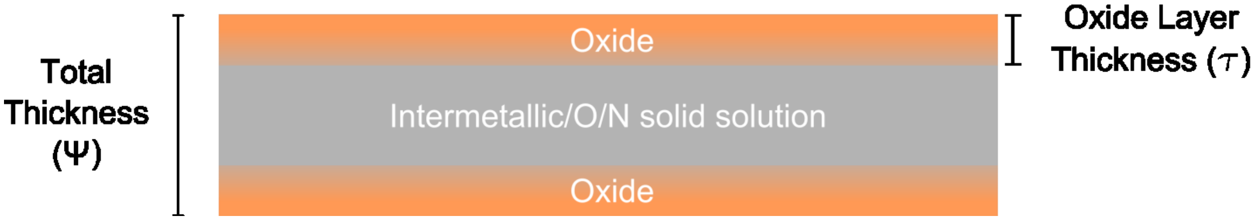

Figure 5.10: Schematic foil cross-section (not to scale) describing the geometry-dependent penetration of oxygen and nitrogen into the foils.

If we assume that the outer oxide layers have a constant thickness in all foils of a given composition, then for smaller thickness foils, larger fractions of the foil will be highly oxidized as the proportion of this outside region increases, and vice versa. The fraction of the initial foil that becomes the highly reacted surface region can be expressed as

$$F = \frac{2\tau}{\Psi} \qquad \text{Equation 2}$$

where Ψ is the foil's total thickness (pre-reaction) and τ is the thickness of the surface oxide layer. We must stipulate that

$$0 \leq \tau \leq .5\Psi \qquad \text{Equation 3}$$

so that the combined volume of the oxide layers on the top and bottom of the foil cannot exceed the total volume of the foil.

F, the fraction of the foil associated with oxide shell (exterior region), can be thought of as volume fraction, mass fraction, or mole fraction because they are all equivalent in this case. The molar volume, density, and Al and Zr contents are all constant across the *initial* foil thickness. These properties will vary for the final foil, but to relate the combustion behavior back to the initial foil geometry, we must neglect the volume and density changes associated with combustion and instead consider what part of the initial foil undergoes complete oxidation.

The total heat of combustion is the sum of the heat generated by the oxidation of the exterior shell, described by *F*, and the heat generated by the intermetallic and solid solution formation at the foil interior, described by $1\text{-}F$.

$$Q_{total} = Q_{exterior} + Q_{interior}$$

Equation 4

The oxidation occurring in the exterior shell can be calculated using the literature enthalpy of formation of ZrO_2 and Al_2O_3 ($\Delta H_{f\ ZrO_2}$ and $\Delta H_{f\ Al_2O_3}$) combined with the moles of Zr and Al (N_{ZrO_2} and $N_{Al_2O_3}$) [91].

$$Q_{exterior} = F[N_{ZrO_2}\Delta H_{f\ ZrO_2} + N_{Al_2O_3}\Delta H_{f\ Al_2O_3} + N_{MgO}\Delta H_{f\ MgO}]$$

Equation 5

Previous work has shown that that all metals in this exterior zone are completely oxidized [45] and so the enthalpy formation of the oxides are the only source of heat. The same study showed that in Al:Zr foils approximately 40 µm thick, the Al and Zr concentrations in the oxide are equal to that of the overall foil composition. This was calculated using the experimentally observed thicknesses of the outermost ZrO_2 layer and underlying 2Al-Zr-5O mixed oxide, combined with the molar volume of each phase to determine the concentration of each metal in the area. Therefore the composition in the exterior region of an Al:Zr foil is N_{Zr}=0.5 and N_{Al}=0.5 initially, and $N_{ZrO_2} = 0.5$ and $N_{Al_2O_3} = 0.25$ after combustion, all in moles oxide per mole of metal atoms.

Because we lack the same data for Al-8Mg:Zr foils, we assume that the same characteristics apply to those foils as well; complete combustion occurs in the exterior region, and the relative amounts of metals in the oxide layers are equal to the overall relative amounts in the initial foil composition. We can therefore calculate the corresponding moles of oxides within the exterior region ($N_{ZrO_2} = 0.5$, $N_{Al_2O_3} = 0.23$, and $N_{MgO} = 0.04$, again in moles oxide per mol of metal atoms). Approximately half of the Mg combusts as a vapor outside of the foil [43], but this does not affect the net heat output because all material that vaporizes recondenses, leading to the same net heat as if it was contained within the mixed oxide and so vaporization is not included in the model.

Crystalline oxides do not form in the interior region of the foil,. Instead, it is likely that solid solutions of oxygen and nitrogen form in the intermetallics. Therefore, the heat produced by the interior zone can be calculated as

$$Q_{interior} = Q_{dissolution} + Q_{intermetallic} \qquad \text{Equation 6}$$

We have found that within the interior of the foil, the dissolved oxygen and nitrogen are homogenously dispersed throughout various intermetallics. The heat of dissolution of oxygen and nitrogen into the interior of the foil can be estimated as

$$Q_{dissolution} = (1-F)\left[\eta_{ox.}\Delta H_{Al/Zr-O} + \eta_{nit.}\Delta H_{Al/Zr-N}\right] \quad \text{Equation 7}$$

where $\eta_{ox.}$ and $\eta_{nit.}$ are the moles of oxygen and nitrogen, respectively, that have dissolved into 1 mole of metal. These values are essentially the oxygen and nitrogen concentrations within the foil interior $(1-F)$. The values of $\eta_{ox.}$ and $\eta_{nit.}$ can be calculated using the SEM-EDS data presented in **Table 5.1** using the results for the 60 μm thick foils because the values of the thickest foils are dominated by the concentration within the interior portions of the foils. Data provided in previous work [43] may be more accurate because it was generated using a microprobe with NIST standard calibrations, but uses fewer data points. To obtain the highest quality data, we have therefore averaged the oxygen and nitrogen compositions from each data set. For Al:Zr foils, $\eta_{ox.}$ and $\eta_{nit.}$ were determined to be 0.12 and 0.11, respectively. For Al-8Mg:Zr foils, $\eta_{ox.}$ and $\eta_{nit.}$ were determined to be 0.25 and 0.39, respectively.

$$\eta_{ox.} = \frac{at.\%\ O}{at.\%\ Al + at.\%\ Zr + at.\%\ Mg} \quad \text{Equation 8}$$

$$\eta_{nit.} = \frac{at.\%\ N}{at.\%\ Al + at.\%\ Zr + at.\%\ Mg} \quad \text{Equation 9}$$

The ΔH terms are the enthalpies of dissolving oxygen or nitrogen into the Al/Zr intermetallics. The enthalpies of dissolution into the range of intermetallic compounds that form are unknown, but the enthalpies of dissolution for oxygen and nitrogen into zirconium are in the literature. The enthalpy of dissolving oxygen into Zr is -415 kJ/mol of oxygen, and -429 kJ/mol for nitrogen [147,148]. Because these are the only known values, we use them as estimates for the enthalpies of dissolution into the various intermetallics ($\Delta H_{Al/Zr-O}$ and $\Delta H_{Al/Zr-N}$).

It is important to note that although the entire foil forms intermetallics initially, any portion that then forms an oxide or nitride must then dissociate again before forming the final products. As such, there is no net heat from forming the intermetallic in the exterior shell. For the solid solutions at the foil interior, oxygen and nitrogen presumably go into interstitial sites within the intermetallics and therefore the intermetallics do not need to dissociate and there is a net heat from forming the intermetallic.

$$Q_{intermetallic} = Q_{int^*}(1 - F) \qquad \text{Equation 10}$$

where Q_{int^*} is the heat of the intermetallic formation reaction in Al:Zr or Al-8Mg:Zr foils, which was measured by bomb calorimetry in argon (**Figure 5.2**).

Application of the Model

We are interested in how the heat production, Qtotal, varies as a function of total foil thickness, Ψ. Therefore, Qtotal was calculated for every integer Ψ value from 1 to 60 μm because this is the area of interest corresponding to the experimental data. The values of each parameter used for Al:Zr and Al-8Mg:Zr foils are provided in **Table 5.2**. The gravimetric heats as a function of foil thickness predicted by the models for each foil type are shown in **Figure 5.11**.

Parameter	Description	Value for Al:Zr	Value for Al-8Mg:Zr
Ψ	Total foil thickness	n= 1 to 60 μm	n= 1 to 60 μm
τ	Thickness of surface oxide layer	2 μm	1 μm
N_{ZrO2}	Moles of ZrO_2 per 1 mole of metal	0.5	0.5
N_{Al2O3}	Moles of Al_2O_3 per 1 mole of metal	0.25	0.23
N_{MgO}	Moles of MgO per 1 mole of metal	0	0.04
$\Delta H_{f\,ZrO2}$	Enthalpy of formation of ZrO_2	-1097 kJ/mol	-1097 kJ/mol
ΔH_{fAl2O3}	Enthalpy of formation of Al_2O_3	-1676 kJ/mol	-1676 kJ/mol
$\Delta H_{f\,MgO}$	Enthalpy of formation of MgO	-602 kJ/mol	-602 kJ/mol
$\eta_{ox.}$	Moles of oxygen dissolved into 1 mole of metal	0.12	0.25
$\eta_{nit.}$	Moles of nitrogen dissolved into 1 mole of metal	0.11	0.39
$\Delta H_{Al/Zr\text{-}O}$	Enthalpy of dissolution of O into the Al/Zr intermetallics	-415 kJ/mol	-415 kJ/mol
$\Delta H_{Al/Zr\text{-}N}$	Enthalpy of dissolution of N into the Al/Zr intermetallics	-429 kJ/mol	-429 kJ/mol
$Q_{int.*}$	Heat produced by the intermetallic formation reactions	-696 kJ/g	-696 kJ/g

Table 5.2: Descriptions of all parameters used in the model of geometry-dependent heat for Al:Zr foils.

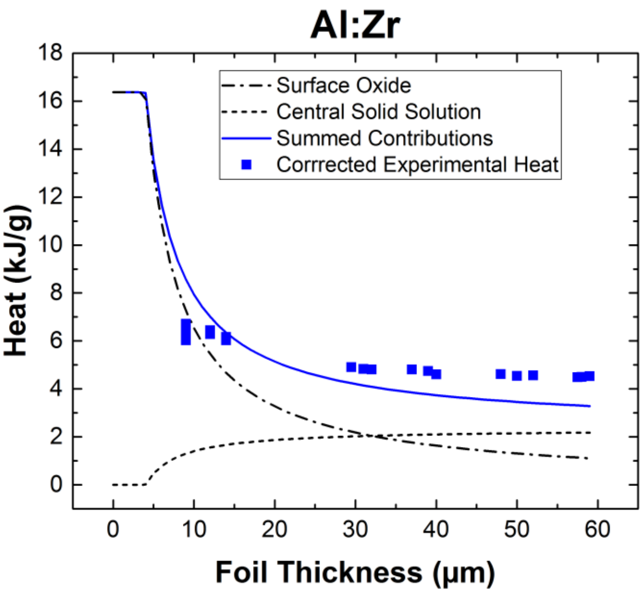

a.

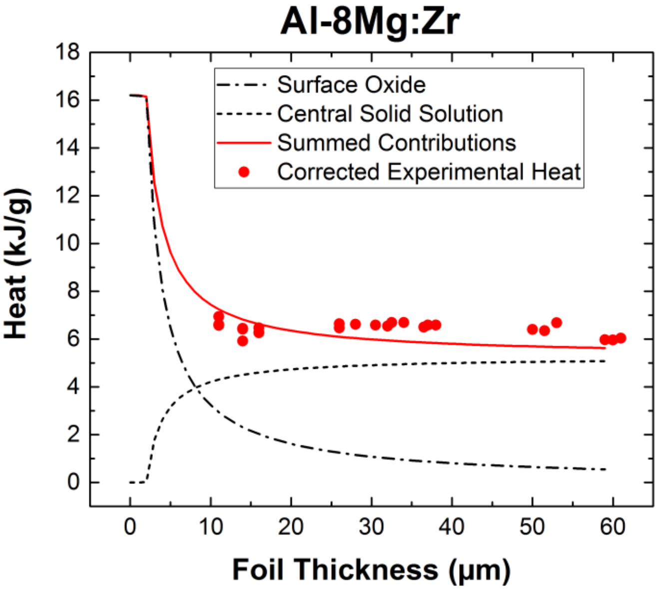

b.

Figure 5.11: The results of the geometric model for a.) Al:Zr and b.) Al-8Mg:Zr foils of varying thicknesses, with experimental data points overlaid for comparison. The models include curves for the interior and exterior regions separately to illustrate each zone's contributions to the net heat.

Interpretation of the Model

The heat generation predicted by the model matches the data well for both foil compositions, which supports that our proposed mechanism offers a feasible explanation of the experimental results. The oxide layer thickness, τ, is the only experimentally observable value that was modified to go into the model. The micrographs presented in **Figure 5.3** and **Figure 5.4** show that the thickness of the oxide layer is roughly 4-5 μm for Al:Zr foils, and roughly 3 μm for Al-8Mg:Zr foils. The model however, does not account for expansion that occurs from oxygen intake during the formation of the oxide, or the significant porosity that is evident in the final products that are not present in the initial foil. Therefore, the τ values used in the model were smaller than the thicknesses estimated from the micrographs.

The calculated heat production displays a plateau at very small thicknesses where the oxide layer thickness, τ, reaches half of the total foil thickness, Ψ. At this point, the entire foil is consumed by the oxide layers and so the heat production cannot increase further. This maximum occurs at the maximum theoretical heat of combustion, which is 16.4 kJ/g for Al:Zr foils and 16.2 for Al-8Mg:Zr foils.

According to the model, Al:Zr foils have a much stronger dependence on thickness because the magnitude of decline in heat from the surface oxide layer is greater than the increase in heat from the central intermetallic region. Thus, the net trend for heat production as a function of foil thickness is dominated by the fraction of foil volume attributed to this oxide layer.

For Al-8Mg:Zr foils on the other hand, the heat contribution from the central solid solution increases at a rate nearly equivalent to the rate at which the contribution from the surface oxide layer decreases. This causes the net heat production to balance at a nearly constant total heat output across the range of thicknesses tested. This conclusion is also supported by the comparison of oxygen and nitrogen content in thick and thin Al-8Mg:Zr foils. Although the averages vary, the oxygen and nitrogen contents of the thick foils are within 1 standard deviation of contents in the thin foils, suggesting that the total amount of oxygen and nitrogen within the foils depends less upon the foil thickness.

5.5 Conclusion

Using bomb calorimetry, we have shown that the heat produced during the combustion of Al:Zr foils is highly dependent upon the growth of crystalline oxide layers on their external surfaces. This causes a strong dependence upon geometry because the volume fraction of this oxide shell becomes smaller and smaller as foil thickness increases. This dependence is not observed for Al-8Mg:Zr foils, however. Imaging reacted foil cross-sections of various thicknesses for each foil composition showed that the oxide layer thickness does not depend upon the foil's overall thickness. Elemental analysis within these cross-sections revealed that the content of gaseous reactants (oxygen and nitrogen) are similar between thin (≈10 μm) and thick (≈60 μm) Al-8Mg:Zr foils, but the thick Al:Zr foils contain significantly less oxygen and nitrogen than do their thinner counterparts . This concurs with the calorimetric result that Al-8Mg:Zr samples maintain high levels of heat release as foil thickness increases, while Al:Zr foils decrease in combustion efficiency. The combustion temperature and duration, as measured with a two-color pyrometer in tandem with a high-speed camera, show that for both foil compositions, temperature is not highly influenced by foil geometry. Burn duration, however, does increase as thickness increases for both Al:Zr and Al-8Mg:Zr foils.

The difference in combustion dependence between Al:Zr and Al-8Mg:Zr foils can be explained by the Mg in Al-8Mg:Zr leading to vacancies that increase the diffusion rates of gaseous reactants into the foil, enabling it to maintain a higher level of combustion efficiency at larger foil thicknesses. The oxygen and nitrogen form solid solutions in the central intermetallic regions of the foil, releasing enough heat to balance the decreasing contribution from the external oxide layers as foil thickness increases. Because significant amounts of heat are produced by both regions, the combustion efficiency of Al-8Mg:Zr foils does not depend upon the foil thicknesses. This mechanism was supported by a simple geometric model, in which the heat produced by each region of the foils was approximated using estimates for the extents of oxidation and nitridation from compositional data.

These findings are significant because our goal of working with these materials is to develop materials that produce as much heat as possible over an adjustable combustion duration. **Figure 5.9** shows that the heat production during the combustion of these Al:Zr and Al-8Mg:Zr foils drops by only 12% with an increase in combustion duration of 100%. This ability may be desirable in various applications, specifically for bioagent defeat purposes in which it is ideal to burn over extended durations while producing as much heat as possible.

6 Heat Production from Al/Zr Reactive Nanocomposite Particles

6.1 Introduction

The work presented in previous chapters focuses on Physical Vapor Deposited (PVD) reactive foils, which serve as simple prototype structures that are highly regular and easier to study in a scientific fashion. The foils are near-perfect rectangular prisms with very regular reactant spacings, which greatly reduces the number of variables that may influence their properties. Additionally, measurements are easier and more repeatable when working with a single, stationary, macro-scale foil rather than a compact of particles. The simple structure of layered foils also allows for straightforward modeling of the intermetallic and combustion reactions that occur [48,113].

In order to be useful as a fuel additive, however, these materials must be fabricated as particles so that they can be mixed into a binder alongside oxidizers and other additives in explosive formulations [149]. The combustion of typical particle compacts is somewhat more complex, though, due to variability in particle size distribution and composition, interplay between adjacent particles, and particle cloud dispersal. Sputter depositing particles has a lower level of control than sputtering foils, but the method does produce particles that are nominally identical in composition and geometry. Thus, while expensive to fabricate, they can serve as model materials to help understand the behavior of mechanically processed nanocomposite powders that are much less consistent from particle to particle. With mechanical processing, the resulting nanocomposite particles show large distributions in particle size, non-uniformities in composition, and variations in the extent of premixing. However, they can be fabricated in kilogram-scale quantities and are therefore more useful in real world applications. Reactive materials made by these three fabrication methods are compared in **Figure 6.1** where cross-sections of representative structures for each material are qualitatively arranged so as to illustrate the trade-off between structural control and utility. Utility includes the ability to mix the material into a formulation, cost per kg, and the potential for mass production.

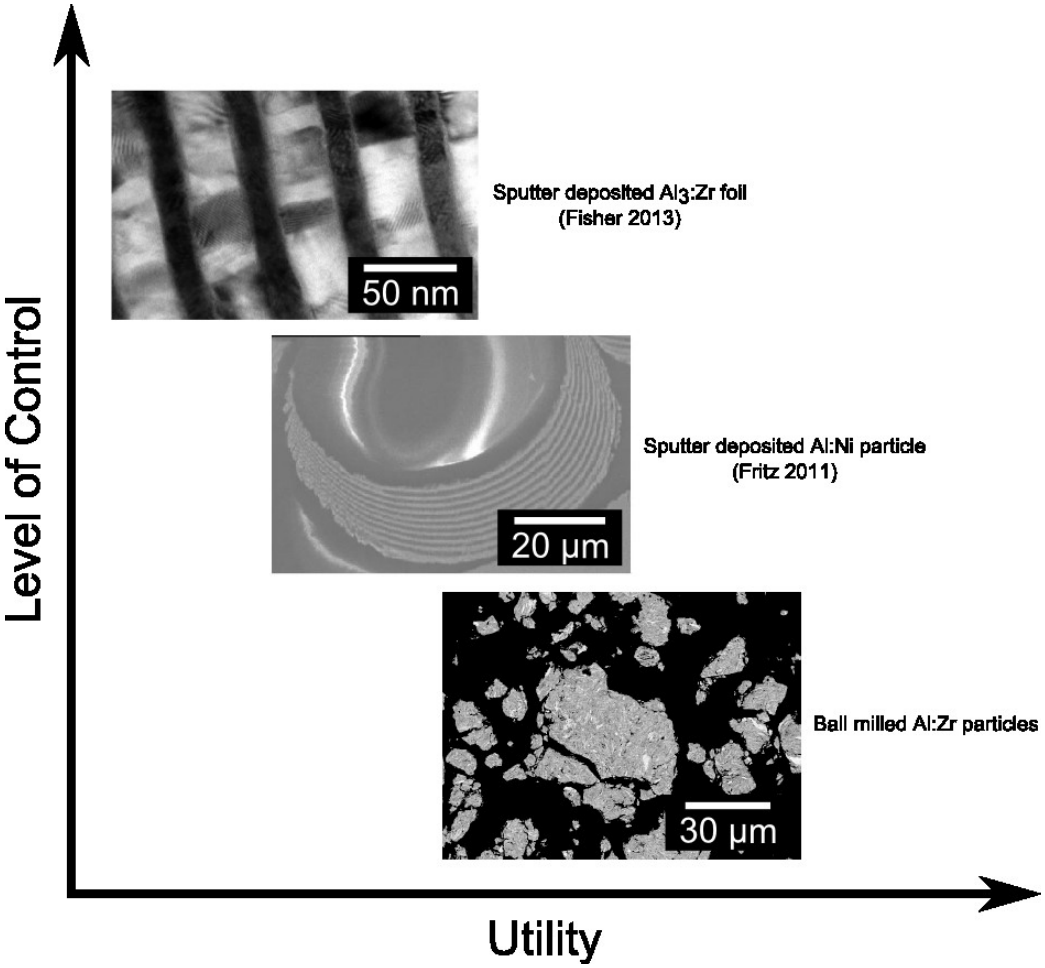

Figure 6.1: Comparing the three different fabrication techniques concerning the level of control and utility of each. Utility includes the ability to mix the material into a formulation, cost per kg, and the potential for mass production. Cross-sections for the 3Al:Zr foils and Al:Ni particles were reproduced from reference [41] and [150], respectively.

Our approach to developing nanocomposite metal fuels has been to start with well-controlled materials to develop a strong scientific understanding, then apply that knowledge to materials with higher utility. The final materials, fabricated by ball milling, are currently under investigation. Combustion characteristics are being determined using high-speed videography to calculate flame propagation speeds, wire ignition tests to determine ignition properties, and spectroscopy to measure temperature and species during combustion. In this chapter, however, we focus on work that has been completed at the intermediate stage using PVD particles. The particles are fabricated by sputtering with the same process described in **Section 3.2.1**, but with nylon mesh for substrates rather than brass sheets. After deposition, the particles are removed from the nylon substrates using a wet, mechanical process.

A loose compact of particles are reacted in 1 atm of oxygen in a specially designed bomb calorimeter. The design of this calorimeter will be described, and the measured heats of combustion for these PVD particles (Al:Zr, Al-8Mg:Zr, and Al-38Mg:Zr) will be reported alongside results for PVD foils and ball milled particles of the same compositions for comparison. We also investigate the heat produced by PVD particles of a single composition (Al:Zr) but varying particle sizes because, as discussed previously in **Chapter 5**, the geometry of the material may significantly affect its combustion.

6.2 Fabrication of PVD Particles

The process of magnetron sputter depositing nanolaminate foils was developed and presented in reference [150] and was modified for this study to obtain the compositions of interest. **Figure 6.2** is a schematic depicting the method that has been reproduced from reference [75].

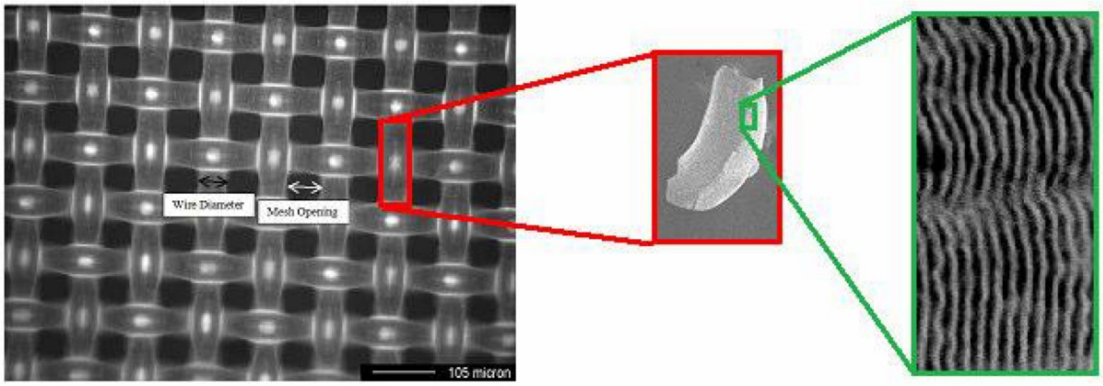

Figure 6.2: Schematic of sputtering reactive nanolaminates onto mesh substrates. The particle size is dictated by the mesh size and the deposition thickness. The figure is reproduced from reference [75].

Nylon mesh with a square weave was used as the substrate for depositing nanolaminate particles because the material deposited onto the surface of the mesh will fracture at the interfaces between the threads when a bending stress is applied. The pattern of the weave and the diameter of the threads dictate the dimensions of the particles; a square weave resulted in particles with a width equal to the thread diameter, and a length that was 3× the width. The thickness of the particle was dictated by the sputtering parameters, specifically the combination of cathode powers and deposition time. The compositions and maximum bilayer spacing of these PVD particles were designed to match those of the PVD foils. Therefore, the sputtering conditions such as target purity, rotation rate, and cathode power, were the same as those detailed in **Section 3.2.1.**

The shape of the nylon mesh caused the particles to have a crescent shape, where the center of the particle is thickest and the edges taper down due to shadowing from adjacent threads during deposition. Also, because the threads were cylindrical, the particles had a rounded morphology, as can be seen in **Figure 6.2**.

As previously shown in **Chapter 5**, the combustion of Al:Zr foils depended strongly upon their geometries. In order to investigate how this dependence applies to particles, we also fabricated Al:Zr particles of varying sizes. However, it has been shown that the packing density of the loose particle compacts depended upon the length to thickness ratio of the particles, and this may influence combustion behavior [150]. Therefore, in order to see trends associated with just particle size and not the packing density, we fabricated particles of three sizes, varying the mesh size and deposition thickness to maintain the same packing fraction while altering overall particle size.

Particle Size Designation	Mesh Size (µm)	Particle Width (µm)	Particle Length (µm)	Particle Thickness (µm)
Small (0.5×)	25	25	75	20
Standard	50	50	150	40
Large (1.5×)	75	75	225	60

Table 6.1: Calculated particle dimensions as a function of mesh size, with thickness adjusted to maintain a constant length to thickness ratio and therefore a constant packing density.

The packing density was measured for each loose particle compact by pouring the particles into a graduated cylinder to a specific volume and measuring the associated mass. Each measurement was performed three times to obtain average values. The cylinder was of large enough diameter that any wall-effects were insignificant.

6.3 Design of the Particle Bomb Calorimeter

The design and functionality of the foil calorimeter was described at length in **Chapter 2** because it is a unique and highly specialized instrument. We also designed and fabricated a second calorimeter specialized for reactive particles. This calorimeter is less specialized because most calorimeters are designed to hold and ignite materials in powder or particle form. However, this calorimeter is still of interest because it is highly sensitive, with a calorimeter constant of 135 J/K, which is roughly double the sensitivity of the foil calorimeter (279 J/K). This is possible because the large container volume required for foils 52 mm in length is obviated for a much smaller particle compact but with a similar mass.

The overall concept behind the design of the particle calorimeter is very similar to that of the foil calorimeter: increase the sensitivity by minimizing the mass and volume of the bomb and the surrounding liquid bath, and by using low heat capacity materials like titanium for the bomb and silicone oil for the bath. **Figure 6.3a** depicts the general calorimeter assembly, which is very similar to that of the foil bomb calorimeter but about half the size. The design of the bomb itself, shown in **Figure 6.3b,** is also very similar to that of the foil calorimeter, with a gas valve and two posts that serve as terminals for electrical connections for ignition. The largest design difference for this calorimeter is the sample holder and ignition mechanism, which are shown in **Figure 6.3c.** Particles are contained in a ceramic crucible held stationary on a platform which can be raised and lowered. There is a V-shaped Nichrome filament between the electrical terminal posts. The sample is raised until the tip of the V is pressed into the sample, and the platform is fixed in place with hex nuts on the platform posts. The bomb is then sealed, connected to the Delrin lid, and lowered into the flask of silicone oil. After equilibration to establish a baseline, the power supply set to ≈10 V is triggered to resistively heat the filament and ignite the particles.

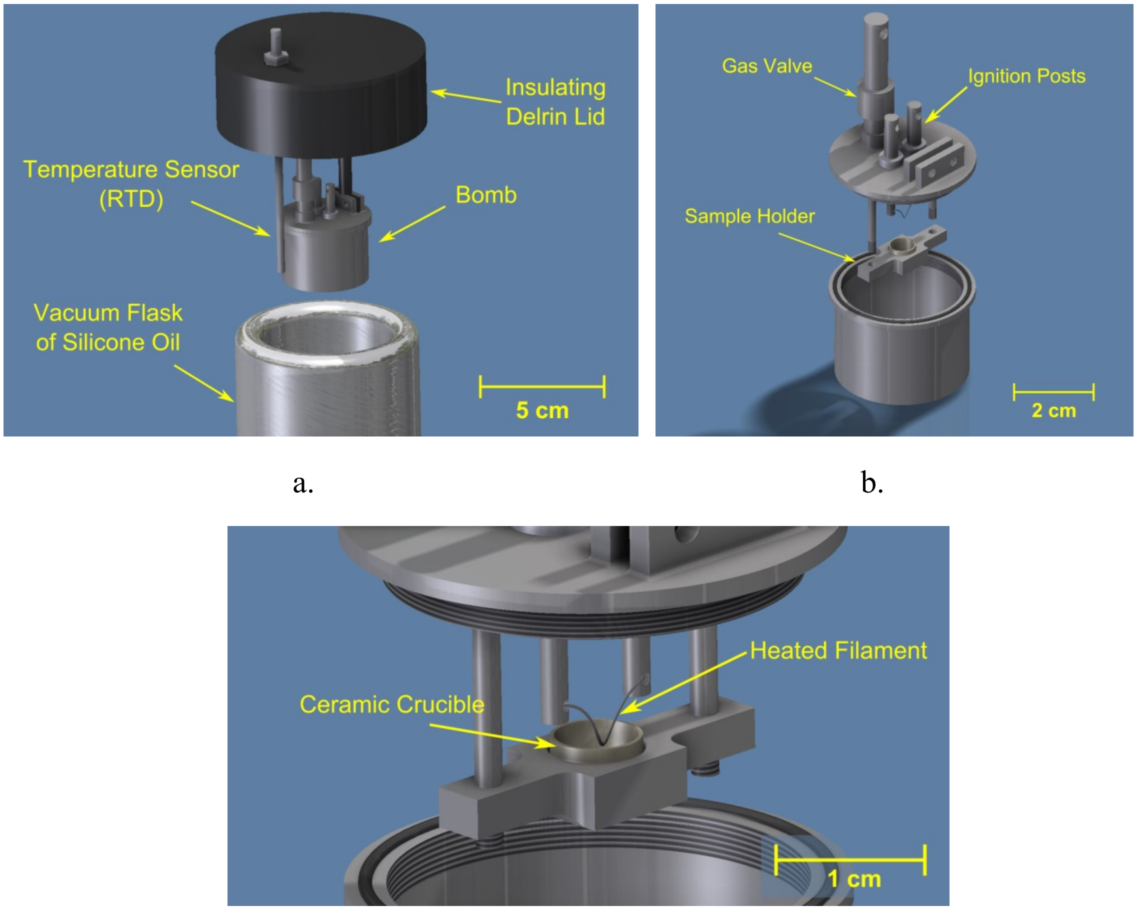

a.

b.

c.

Figure 6.3: The design of the particle bomb calorimeter. (a) Major components of the particle bomb calorimeter assembly, including a vacuum flask of silicone oil, an RTD temperature sensor, and a Delrin lid for insulation. (b) The environment of the bomb is controlled via the gas valve welded to the lid, and ignition is achieved by connecting leads from the power supply to the ignition posts. (c) The samples are contained in a ceramic crucible in a holder than is raised until the sample is in contact with a filament that is resistively heated for ignition.

For these particular tests, each particle sample was reacted in the calorimeter in 1 atm of oxygen. It was not possible to obtain reliable data for samples reacted in 1 atm of air because particles did not eject from the crucible in that atmosphere, resulting in wide variations in the data. The combustion behavior in air was primarily a function of the amount of particles that did eject, since the remaining particles would sinter together in the crucible, greatly inhibiting combustion. This caused the data to be erratic and not representative of how particles would burn as a dispersed cloud, which is closer to the condition of interest (explosive launch).

6.4 Results

To ensure that the PVD particles of each composition and geometry of were comparable, we first determined the packing density of each. The percent of the theoretical maximum density (%TMD) is calculated as the density of the compact relative to the density of a fully dense alloy of the same composition. PVD foils have a %TMD of 100% because they are deposited as fully-dense structures. The loose particle compacts had a %TMD of approximately 38.5% for each size and composition, except for the Al:Zr particles deposited onto the 25 μm mesh. The %TMD was significantly lower for this sample, at only 29.7%. The packing density and %TMD for each particle type is provided below in **Table 6.2**. After measuring the particles by optical microscopy, we found that this anomalous %TMD is likely the result of unreliable dimensions of the 25 μm mesh. Although the particles were approximately 25 μm wide, as was expected, they were significantly longer than designed for; roughly 126 μm long in comparison to the expected length of 75 μm. The other samples (intermediate and large sizes) were of the correct approximate dimensions, with an average error of ±11%.

Each of these samples was combusted in 1 atm of oxygen in the particle bomb calorimeter. The data for the three compositions of particles sputtered onto the 50 μm mesh (particles 50 μm x 150 μm x 40 μm) is presented in **Figure 6.4**: with data from PVD foils and ball milled materials of the same compositions for comparison. The PVD foils were approximately 40 μm thick, matching the smallest dimension of the particles, and were combusted in 1 atm of oxygen in the foil bomb calorimeter, as presented in **Figure 3.4**. The ball milled particles were milled for 1 hour with a ball to powder ratio (BPR) of 10, and had a mean diameter of approximately 30 μm. The full details of fabrication and other characterization techniques performed on these ball milled particles are outside the scope of this chapter, and will be the subject of a forthcoming publication.

Composition	**Mesh Size (μm)**	**Packing Density (g/cm^3)**	**% TMD**
Al:Zr	25	1.46 ± 0.02	29.7
Al:Zr	50	1.84 ± 0.05	37.3
Al:Zr	75	1.97 ± 0.02	40.0
Al-8Mg:Zr	50	1.91 ± 0.04	39.4
Al-38Mg:Zr	50	1.73 ± 0.02	37.7

Table 6.2: Packing density for PVD particles of varying sizes, as represented by mesh size. The mesh size dictates the particle dimensions, as described in **Table 6.1**.

The Al:Zr and Al-8Mg:Zr particles, whether ball milled or sputter deposited, all released ≈11.3 kJ/g of heat during combustion with differences typically falling within one standard deviation of each other. This was a 46% improvement over the best-performing PVD foil, specifically the Al-8Mg:Zr foils. The Al-38Mg:Zr particles did not perform as well, with the PVD particles producing only 26% more heat than the PVD foils, and the ball milled particles actually performed 20% worse than the foils. This is the only case in which the ball milled materials do not perform within one standard deviation of the PVD particles.

The heat of combustion from Al:Zr PVD particles of varying sizes was also tested. The data presented in **Table 6.3** shows that size did not play an important role in these tests, as it did for foils, despite large changes in SA/V. The SA/V values were calculated by approximating the PVD particles as rectangular prisms, or essentially miniature foils.

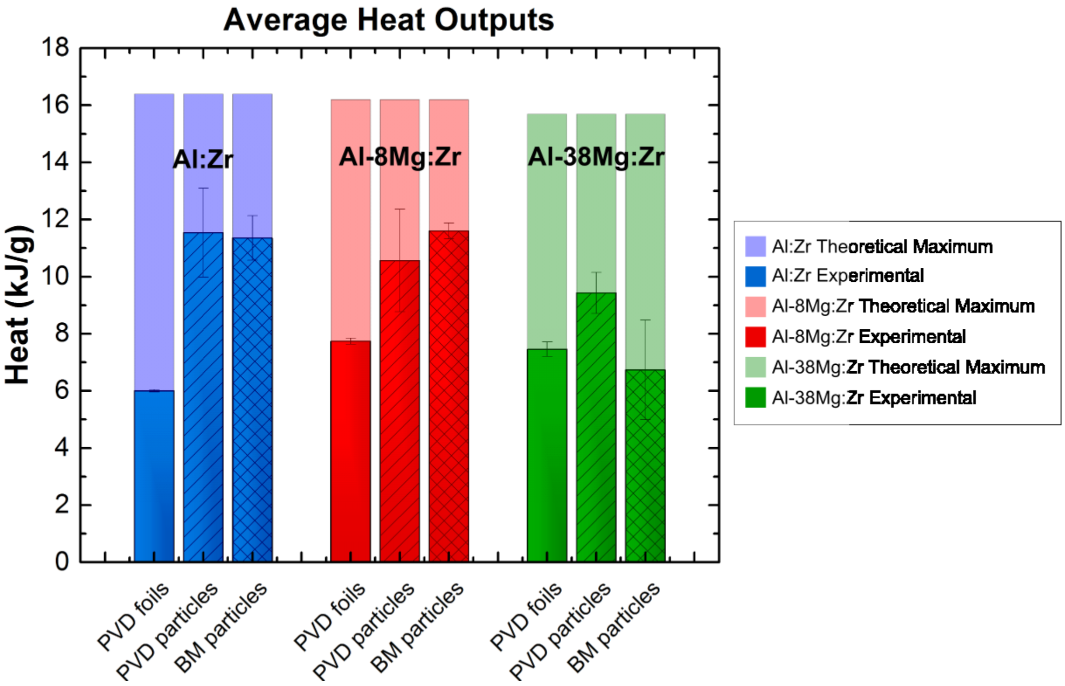

Figure 6.4: Bomb calorimetry data where PVD particles of each of the three chemistries of interest are compared with materials of the same composition but with different geometries and microstructures that result from their different fabrication methods.

Particle Size	Particle Width (µm)	Particle Thickness (µm)	SA/V	Heat (kJ/g)
Small (.5x)	25	20	0.21	10.2 ± 1.3
Standard	50	40	0.10	11.5 ± 1.6
Large (1.5x)	75	60	0.07	11.7 ± 1.0

Table 6.3: Heat production from PVD particles of varying sizes, as measured with bomb calorimetry in 1 atm of oxygen.

6.5 Discussion

The results presented in **Figure 6.4** allow us to compare the heat output from chemically similar structures that were produced by three different fabrication techniques and resulted in three different geometries: sputtered foils, sputtered particles, and ball milled particles. It also allows us to compare the heat output for each geometry for three different compositions: Al:Zr, Al-8Mg:Zr, and Al-38Mg:Zr.

Let us first assess the differences associated with fabrication techniques and material geometry. These results show that the particle samples generally combust more effectively than their foil counterparts. This is understandable when one considers that the solid-state mass transport of oxygen through the surface oxide can limit the extent of combustion, as presented in **Chapter 4**. This is expected to be less problematic for particles because they are at a higher temperature and likely molten during combustion, as will be discussed shortly. Combustion of particles is further enhanced because as particles burn in a cloud, each particle radiates its heat onto its neighbors and also is constantly traveling through the environment, thereby minimizing zones of oxygen depletion. There is no significant difference between the Al:Zr and Al-8Mg:Zr PVD particles and ball milled particles, indicating that the reduction in control over particle size, shape or average chemistry that is associate with ball milling compared to PVD, does not negatively impact combustion behavior in these tests. However, we do expect that the finer and more uniform spacing of reactants in the PVD particles will yield lower ignition temperatures for the intermetallic reactions that drive the particles to high temperature and enable combustion to begin. The results suggest that as long as ignition does occur, the initial reactant spacing or microstructure is not expected to be of great importance for combustion. In the case of Al-38Mg:Zr, however, the ball milled material does not combust as effectively. This could be attributed to the higher Mg composition causing the material to be more brittle so that Mg-rich zones fragmented into smaller particles and mix poorly with the other reactants. This may cause each individual particle to vary too much in chemistry.

Comparing the heat from particles of the three different compositions, we find that Al:Zr and Al-8Mg:Zr particles perform equally as well. The benefit of a small amount of Mg that we see for foils comes from an increase in vacancy concentration, both within the intermetallic as well as the oxide layer, which enhances diffusion and therefore the extent of combustion. Spectroscopy of burning particles, however, shows that they are combusting at approximately 3000 K (roughly double the combustion temperatures of the foils) and that a significant amount of Al is vaporizing. Still frames from a high speed video of 40 μm Al:Zr PVD particles reacting in air (**Figure 6.5**) demonstrates that particle combustion evolves a plume of vapor, even though Mg is not present in the composition shown. With these facts, we can argue that Mg may no longer boost reaction rates compared to the binary compositions. The particles are at a very high temperature and likely molten, and so diffusion is already much faster than it is for foils. Furthermore, the equilibrium vacancy concentration is very high at these temperatures and so additional vacancies from Mg are not as critical, especially when one considers that Al vaporizing will also create vacancies.

The Al-38Mg:Zr particles do not perform as well as the particles of the other two compositions, further supporting the above argument that the benefits Mg provides to foils are not as critical for particles. In fact, it seems that a high Mg content will even hinder combustion because replacing Al with Mg only lowers the theoretical heat of combustion (from 16.4 kJ/g for Al:Zr to 15.7 kJ/g for Al-38Mg:Zr).

Different size PVD Al:Zr particles were also combusted in the bomb calorimeter in order to see if size plays an important role in combustion efficiency as it does for large foils. According to the literature, combustion should improve as particle size decreases as long as particles are not so small that surface passivation significantly reduces their energy density [131–134]. **Table 6.3** shows that the particle size does not seem to have a strong influence, despite corresponding to appreciable changes in the surface area to volume ratio. The large sized particles (75 μm x 225 μm x 60 μm) perform within the deviation of the intermediate sized particles (50 μm x 150 μm x 40 μm). The small particles, theoretically 25 μm x 75 μm x 20 μm, however, perform worse than the intermediate size particles, which is contrary to what would be expected for decreasing particle size. As discussed in the Results, this could be due to the fact that the actual particles were ≈68% longer than anticipated, causing the %TMD to be lower than the

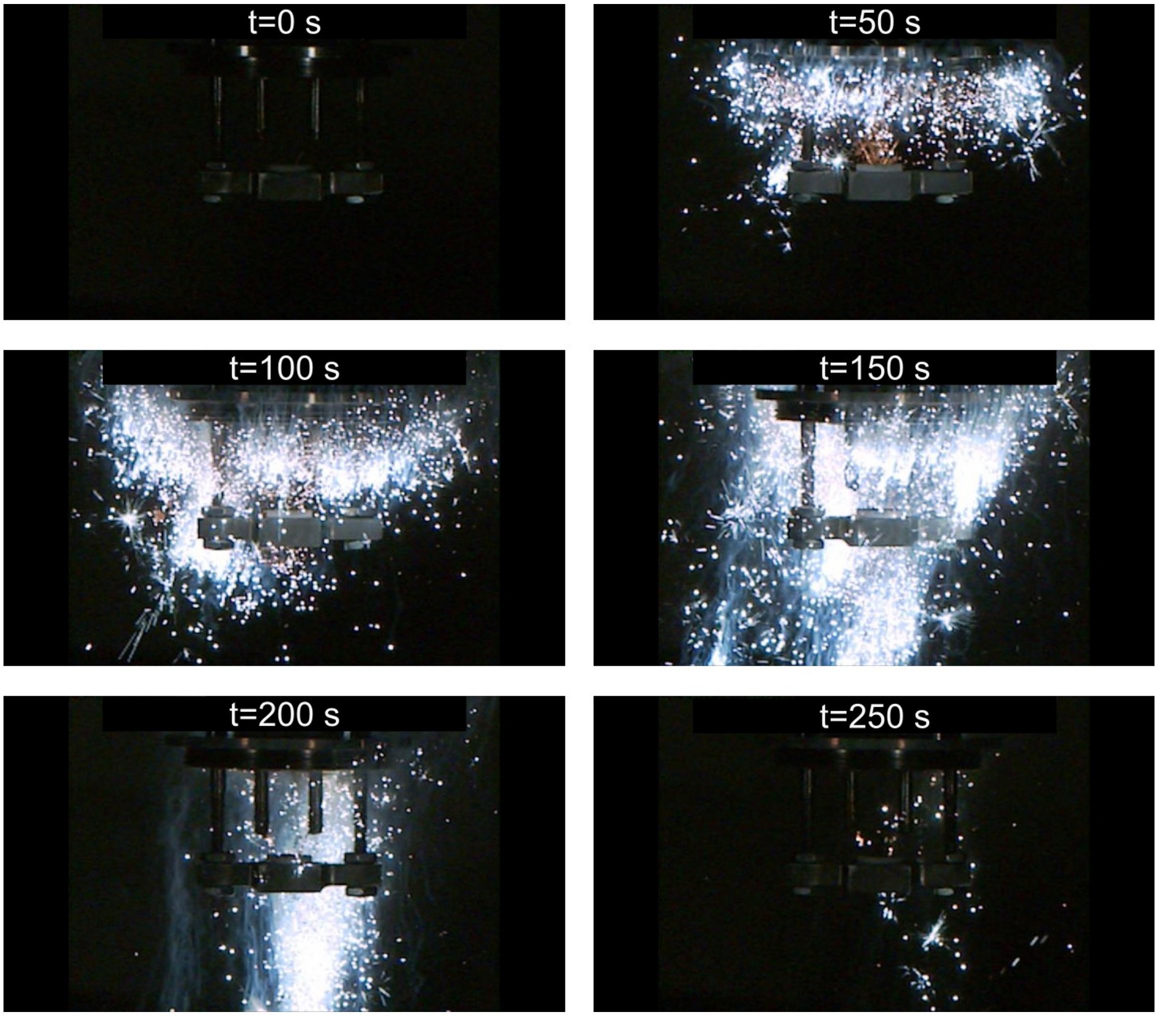

Figure 6.5: Still frames from a high speed video of 40 μm PVD particles reacting in open air, held in the assembly used within the particle bomb calorimeter (**Figure 6.3c**). Because there is no Mg in this system, the vapor must be Al.

others (**Table 6.2**). This makes it difficult to compare against the intermediate and large sized particles. It is possible that they did not perform as well because a lower %TMD implies weaker heat transfer between particles, and thus a lower extent of reaction.

Despite this argument, the combustion energy of these particles is still within 1 standard deviation of the intermediate particles, and nearly within the deviation for the large particles. This likely indicates that the particle geometry is not critical in this size regime. This is not unexpected because the theoretical SA/V values for these particles differ only by a factor of 3 between the smallest and largest particles tested. Other studies show that combustion behavior changes for smaller particles (1-10 μm in diameter) where the SA/V changes dramatically for relatively small changes in particle diameter, as is evidenced in the Introduction of **Chapter 5** [84,136].

6.6 Conclusion

Nanolaminate particles were fabricated by magnetron sputtering to bridge our understanding between well-controlled foils and less-controlled ball milled particles. We tested samples of varying compositions within each fabrication method, and also explored the effect of particle size on Al:Zr PVD particles, which were expected to have the strongest correlation between size and heat output according to previous work (**Chapter 5**). Each sample was combusted in a bomb calorimeter under 1 atm of oxygen.

The results indicate that particle size is inconsequential in this regime and the comparison of particles of different compositions shows that Mg is not helpful. Both of these conclusions differ from the trends found for foils, though this is not unexpected because the mechanisms of macroscopic foils burning for long durations (>1 s) and low temperatures (≈ 1630 K) do not necessarily apply to particles. In foils, Mg provides the benefit of vaporizing at low temperatures and is therefore the only species vaporizing. In these particles however, the Al vaporizes and so replacing a portion of that Al with Mg only lowers the energy density of the material.

Comparing the fabrication methods, we found that Al:Zr and Al-8Mg:Zr particles, whether sputtered deposited or ball milled, significantly outperform foils of the same compositions. Ball milled particles have less controlled sizes, compositions, reactant spacings, and extents of premixing, but they are much cheaper to fabricate and have the potential to be mass produced. The fact that they performed just as well as the PVD particles is very encouraging because it shows that despite a loss of control, we are still able to attain strong intermixing between reactants to ignite the particles, and efficient combustion. This study therefore demonstrates that these materials can be manufactured in large quantities via ball milling without negatively impacting the extent of combustion in our bomb calorimetry tests in 1 atm of oxygen.

7 Conclusion

Reactive metal nanolaminates offer significant control over reaction properties such as the ignition temperature, the heat of combustion, and the burn duration. The independent control of each property is not possible with simple metallic particles, but is highly desirable for energetic material applications such as bioagent defeat, in this case. We have designed materials that ignite at a lower temperature than unstructured alloys of the same overall composition, to ensure that all of the fuel will ignite during the initial detonation event. We conducted the majority of our research on sputter deposited nanolaminate foils because parameters such as reactant spacing, composition, and overall geometry, are all very well controlled in this fabrication process.

The generation of heat from these materials must be maximized for thermal destruction of anthrax spores, as well as to decompose iodine precursor compounds that provide chemical destruction as well. Therefore, combustion bomb calorimetry is a very important tool for comparing these candidate materials. We designed a bomb calorimeter specialized for measuring the heat output from reactive foils in various environments. The foils are mounted onto a frame that holds the foil in a way that minimizes heat sinking and maximizes the foil surface area exposed to the environment. Foils are ignited in this setup with a small electric spark. The heat produced by the foil diffuses throughout the calorimeter, and produces a measurable temperature change in a liquid bath that the bomb is submerged in. The calorimeter is highly sensitive, with a calorimeter constant of 279 J/K. This corresponds to measuring large rises in temperature (on the order of 1 K) from foil samples down to 10 mg. This high level of sensitivity was accomplished by reducing the heat capacity of the system by using lower heat capacity materials such as titanium for the bomb instead of steel and silicone oil for the bath instead of water, and by reducing the size of each component as much as possible.

This calorimeter was used to compare the heat generation from foils of three different compositions: Al:Zr, Al-8Mg:Zr, and Al-38Mg:Zr. Previous work has shown that the Al:Zr system combusts for extended durations, and Mg is a relatively volatile metal that is known for its utility in pyrotechnics. The purpose of this study was to determine if the addition of Mg into the Al layers could improve the combustion efficiency of Al:Zr. Results indicate that a small amount of Mg is indeed helpful because the Mg vaporizes at the temperatures reached during combustion, thereby introducing vacancies into the bulk of the foil. Furthermore, Mg can form oxygen vacancies in the ZrO_2 product layer that forms at the surface of the foils. Both of these contributions lead to improved diffusion of oxygen and nitrogen through the foil, and consequently, greater extents of reaction.

In order to better understand what limits the combustion in Al:Zr foils, we performed an in-situ X-ray Diffraction study at the Cornell High Energy Synchrotron Source (CHESS) to measure the growth of different phases throughout combustion. Reacted foil cross-sections were also investigated using Transmission Electron Microscopy (TEM) to analyze the final microstructure. By combining these in-situ and ex-situ analyses, we were able to propose a reaction mechanism that explains how Al:Zr foils combust, and why they do not burn to completion in air. Zr oxidizes preferentially over Al, and so orthorhombic ZrO_2 forms rapidly on the surface of the foil and grows linearly over time, implying that the rate of growth is interface controlled. In order to form ZrO_2 at the surface, Al must diffuse inward, causing an Al-rich zone to develop under the surface oxide. The Al-rich zone forms an Al_2Zr intermetallic which eventually grows into a continuous layer that prevents Al from diffusing away from the oxide/intermetallic interface. As a result, Al begins to oxidize alongside the Zr, forming a lamellar Al_2O_3/ZrO_2 mixed oxide layer. Oxygen diffusion through Al_2O_3 is slower than diffusion through ZrO_2 by 13 orders of magnitude, and so diffusion through this mixed oxide layer becomes rate limiting. When growth of the oxide becomes diffusion limited, the heat generation rate slows, and temperature decreases. This triggers a feedback loop: when the temperature decreases, diffusion is slower, so combustion is slower, and that causes the temperature to decrease further. This cycle results in the rapid termination of combustion.

Considering that the extent of combustion is limited by the thickness of the surface oxide layer, it is reasonable to expect that the combustion efficiency might be highly dependent upon the total thickness of the foil. This dependence arises because as a foil's thickness increases, the volume fraction of the surface oxide layer decreases. To test this theory and how it might apply to foils containing Mg, we performed bomb calorimetry on Al:Zr and Al-8Mg:Zr foils with thicknesses ranging from approximately 10 to 60 μm. We also cross-sectioned these foils and used Scanning Electron Microscopy with Energy Dispersive Spectroscopy (SEM-EDS) to determine the thickness of the oxide layers and compare the O and N contents of various foils. We found that the gravimetric heat of combustion for Al:Zr foils had an inverse relationship with thickness, with a 42% decrease in heat output occurring between the thinnest (9 μm) and thickest (59 μm) foils. There was no dependence, however, for Al-8Mg:Zr foils within the range of thicknesses tested. Also, the foil thickness had no effect on the average combustion temperature for foils of either composition, though duration did increase for both. We developed a simple geometric model for heat production that supports a mechanism in which diffusion is faster in Al-8Mg:Zr foils, enabling larger quantities of O and N to dissolve into the central intermetallic region. The heat generated by their dissolution is not thickness dependent, and dominates the net heat production within the range of thicknesses tested. For Al:Zr foils, however, diffusion into the bulk is slower and so the net heat production is dominated by the formation of the oxide shell. Therefore, the combustion efficiency of Al:Zr samples is highly dependent upon the volume fraction of the surface oxide, which decreases as foil thickness increases.

The results of these tests have all shown that we are able to control the heat generation during combustion by altering foil composition, and to control combustion duration by altering the foil geometry. Foils, however, are not easily utilized in an explosive formulation. To mix these materials into a polymer binder alongside oxide particles, we must fabricate reactive nanolaminate particles. We made reactive Al:Zr, Al-8Mg:Zr, and Al-38Mg:Zr particles by sputter depositing onto mesh substrates of various sizes, corresponding to final particles of different sizes. We performed bomb calorimetry on each sample in 1 atm of oxygen, and compared these results against foils and ball milled particles of the same compositions. The results indicated that particles of either fabrication method produced significantly more heat than the corresponding foils, but changing the size of the particles by small amounts did not have a significant influence on heat production. Perhaps the most important result was that the sputtered particles and ball milled particles generally performed equally well. This is crucial because ball milling is a more economically feasible method than sputter deposition, but the level of control is comparatively low and so variability in reactant spacing, particle size, and particle composition may arise. The fact that they performed as well as sputter deposited particles in terms of combustion energy, however, is promising because it indicates that we can apply what we have learned to materials that can be mass produced for real world applications.

8 Appendices

8.1 Intermetallic Formation Reactions

The bulk of the heat from these foils is produced during combustion, but the intermetallic formation reactions are important for ensuring ignition and bringing the material up to high temperatures where combustion is possible. The heat of the intermetallic formation reaction can be quantified using Differential Scanning Calorimetry (DSC), and ignition temperatures as a function of bilayer characterizes the sensitivity.

8.1.1 Differential Scanning Calorimetry

A Perkin Elmer DSC 8000 was used to measure the heat produced by Al:Zr, Al-8Mg:Zr, and Al-38Mg:Zr sputter deposited foils. Roughly 5 mg of sample were loaded into copper pans, and the lids were crimped closed. Temperature was ramped from 50 °C to 725 °C at a rate of 40 °C/min, then cooled back to 50 °C, all under flowing argon. The heating step was then repeated to provide a baseline that can be subtracted from the reactions that occurred during the first heating. The temperatures at which heat is released indicates the sensitivity of the reactions, and the integrated area for each curve provides the total heat output within the stated temperature range. **Figure 8.1** shows that the addition of Mg seems to lower the temperature of the reactions, most notably the second major peaks, occurring at 709 °C for Al:Zr, 595 °C for Al-8Mg:Zr, and 530 °C for Al-38Mg:Zr. This likely corresponds to the decreasing melting temperature of the Al-Mg solid solutions as more Mg is added [151]. The peaks themselves are not measurements of the endothermic melting event, but rather measurements of the exothermic mixing that is enabled by one component melting.

The heats measured from these samples are low in comparison to that of Al:Ni foils, which produce -1132 J/g [152]. Mg is expected to decrease the energy of the intermetallic formation reactions because the Al and Mg are already deposited as a solid solution and Mg and Zr are completely immiscible [90]. The data for Al-8Mg:Zr and Al-38Mg:Zr agrees with this because there is a dramatic decrease in heat between those two samples. The heat from the Al:Zr foils, however, is lower than that of the Al-8Mg:Zr foils. This is likely due to the fact that the equivalent reactions for Al:Zr foils are simply occurring at higher temperatures and are therefore not included in the measurement. For this reason, the comparison to the foils of the other two compositions is not straightforward.

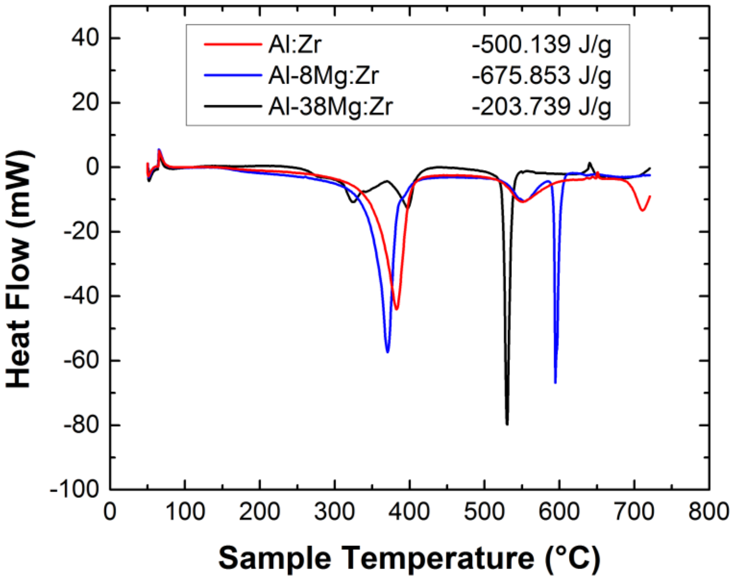

Figure 8.1: Differential Scanning Calorimetry (DSC) results for sputter deposited foils of the three compositions of interest. Endothermic reactions are positive, and exothermic reactions are negative on this scale.

8.1.2 Ignition Temperature

The ignition temperature of Al:Zr, Al-8Mg:Zr, and Al-38Mg:Zr foils were measured by dropping small fragments of each foil, roughly 2 mm x 2mm squares, onto a hotplate of known temperature. For each foil composition, the bilayer spacing was varied by using foils from different positions on the substrate because during fabrication, deposition is fastest at the center of the substrate but slower towards the extremes. This leads to larger bilayers and total foil thicknesses at the center, and a decreasing gradient towards the top and bottom. For Al-8Mg:Zr, a wider range of bilayers were obtained by combining to sputter runs with one ranging from roughly 30 to 50 nm, and the second from 50 to 90 nm.

The temperature was measured using a thermocouple on the hotplate surface, and fragments were dropped onto the surface when the temperature was stable to ±1 °C. 15 foil fragments were used for each test to ensure the results were representative of the overall foil behavior. Ignition is defined as the minimum temperature at which 100% of the fragments of a certain composition ignite immediately upon introduction to the hotplate surface.

The data presented in **Figure 8.2** demonstrates that the ignition temperatures are lower for Mg-containing foils, which supports the DSC results showing peak shifts to lower temperatures. As previously discussed, this is logical when one considers the Al-Mg phase diagram showing that melting and therefore intermixing occurs at lower temperatures as the Mg-content increases. For foils of every composition, as bilayer increases, ignition temperature increases because the mass transport between layers must occur across larger diffusion distances, therefore increasing the activation energy of the reaction.

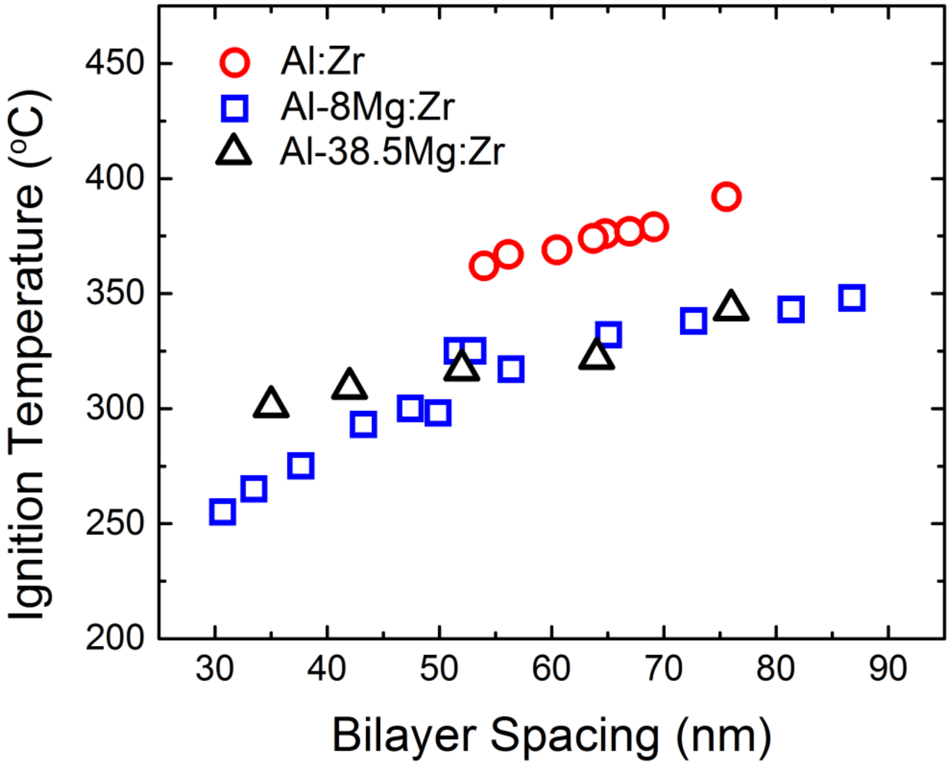

Figure 8.2: The temperatures at which 100% ignition occurs for foils of various compositions as a function of bilayer spacing.

8.2 Foil Bomb Calorimeter "Oxygen Requirement" Correction

As mentioned in **Section 5.2.2**, the fixed amount of oxygen in the combustion bomb calorimeter can cause a bias for more complete reactions of smaller foils. This influence is not applicable to reactions performed in open air, and therefore must be corrected for.

The correction method is shown in **Figure 8.3**. Correction functions were developed for foils of each composition by varying foil mass but not thickness by adjusting foil width to isolate the effect of the oxygen requirement trend. The "X" marks a theoretical point where the foil mass is such that there is exactly 100% of the required oxygen in the bomb (17.99 mg for Al:Zr samples and 18.16 mg for Al-8Mg:Zr samples). Plotting heat per mass as a function of mass should be a horizontal line, and any deviation from that is due to oxygen starvation. The correction factor is the difference between this horizontal line and the function fit to the experimental data. The correction function for Al:Zr is therefore $Q=Q'+4570-14102x^{-0.390}$ and for Al-8Mg:Zr samples is $Q=Q'+6534-19381x^{-0.375}$ where Q is the corrected heat per gram, Q' is the initial heat per gram, and x is foil mass in both cases. There are no experimental data points below 26 mg because the deviation in the measurements increased significantly for mass below this point.

Figure 8.4 shows bomb calorimetry results for samples in which the mass is held constant at 36.5 mg, despite thickness varying from approximately 10 to 60 μm. This was accomplished by adjusting the foil width to compensate for mass changes from varying the thickness. Holding mass constant is one method of removing the influence oxygen starvation because all foils are essentially equally starved. Trends are therefore valid, while actual values are lower than would be expected in environments with 100% of the required oxygen. It appears that there is no trend for Al-8Mg:Zr foils, while the energy output declines as foil thickness increases for Al:Zr foils. This trend agrees with the corrected results presented in **Figure 5.2**, verifying that our correction is valid. Aside from heats being lower than they would be in an environment of plentiful oxygen, another limitation of this method is we have only rough control over foil width and so it is very difficult to attain foils of very similar masses across a wide range of thicknesses. Therefore, this approach could only be used to verify the trend at a few data points, and could not be used for the full data set.

Further validation is provided in **Figure 8.5**, which shows that changing the width of the foil does not influence the heat of combustion. The correction for the oxygen bias was applied to data of all widths and thicknesses for a) Al:Zr and b) Al-8Mg:Zr foils. The open symbols show samples with widths varying from 2.5 to 15 mm while thickness was held constant at approximately 10 μm, 35 μm, and 55 μm. The closed symbols show the corrected data from **Figure 8.4**, for which width was held constant at 10 mm, but thickness was varied from approximately 10 to 60 μm. Again, only data for samples >26 mg were used because the deviation increases dramatically for the samples below this mass. The points where width is varied match the data where width is held constant, validating that our assumption that the width (within the range tested) has no inherent influence on combustion behavior of the foil and that the effect of the oxygen requirement bias is completely negated by the correction.

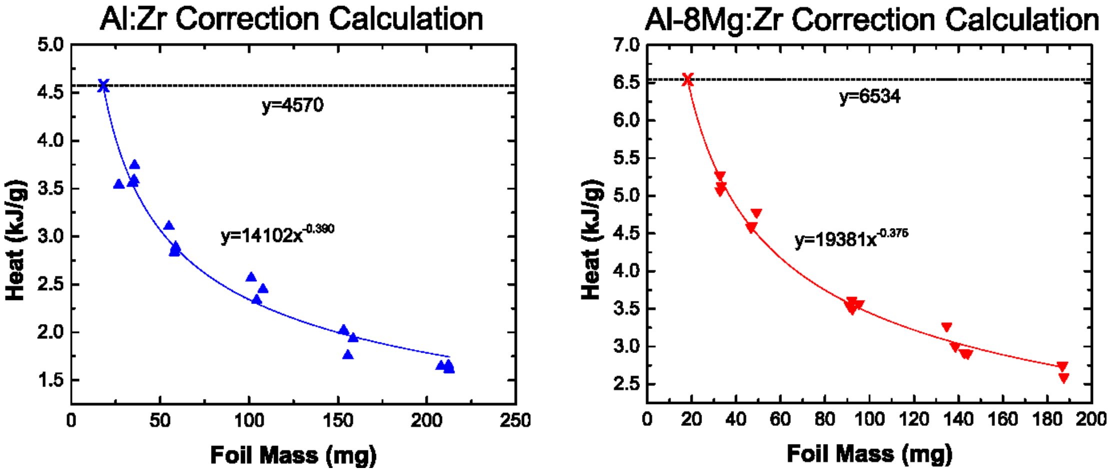

a. b.

Figure 8.3: Calculating a correction function using (a) Al:Zr and (b) Al-8Mg:Zr foil data where thickness is held constant while mass is varied via changes in width.

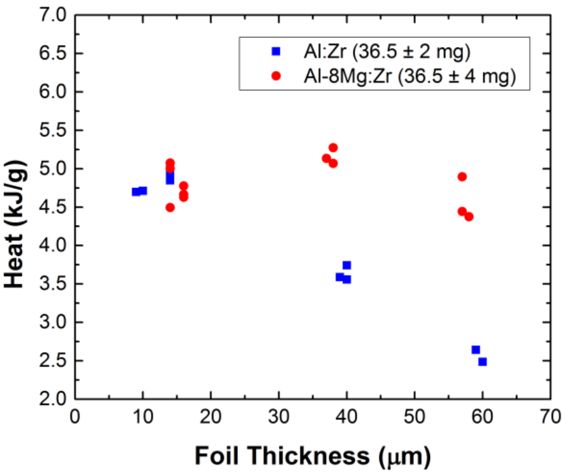

Figure 8.4: Verification of the oxygen requirement correction. There is no need for a correction if mass is fixed while thickness is varied. These trends match very well with results presented in **Figure 5.2**, demonstrating that the correction applied must be valid.

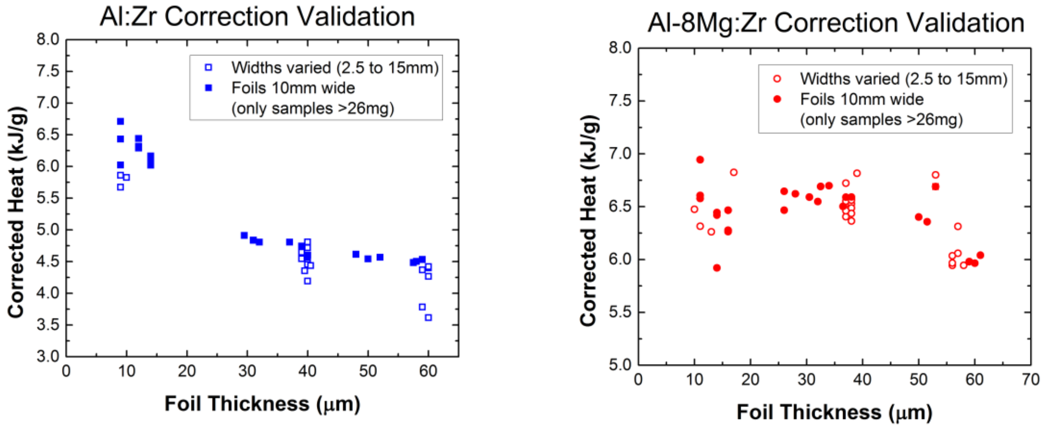

a.

b.

Figure 8.5: Validating that the correction works, but applying it to data of all widths and thicknesses for (a) Al:Zr and (b) Al-8Mg:Zr foils.

9 Bibliography

1. Dreizin EL. Metal-based reactive nanomaterials. Prog. Energy Combust. Sci. 2009;35:141–67.

2. Luca LT, Galfetti L, Severini F, Meda L, Marra G, Vorozhtsov AB, et al. Burning of Nano-Aluminized Composite Rocket Propellants. Combust. Explos. Shock Waves. 2005;41:680–92.

3. Byers LS. Nitrate Explosive Containing Aluminum. United States; 1952.

4. Markstein GH. Combustion of Metals. AIAA J. 1963;1:550–62.

5. Meda L, Marra G, Galfetti L, Severini F, De Luca L. Nano-aluminum as energetic material for rocket propellants. Mater. Sci. Eng. C. 2007;27:1393–6.

6. Xu S, Labuza TP, Diez-Gonzalez F. Thermal inactivation of Bacillus anthracis spores in cow’s milk. Appl. Environ. Microbiol. 2006;72:4479–83.

7. Juneja VK, Porto-Fett ACS, Call JE, Marks HB, Tamplin ML, Luchansky JB. Thermal inactivation of Bacillus anthracis Sterne in irradiated ground beef heated in a water bath or cooked on commercial grills. Innov. Food Sci. Emerg. Technol. Elsevier B.V.; 2010;11:123–9.

8. Busta FF. Thermal inactivation characteristics of bacterial spores at ultrahigh temperatures. Appl. Microbiol. 1967;15:640–5.

9. Montville TJ, Dengrove R, De Siano T, Bonnet M, Schaffner DW. Thermal resistance of spores from virulent strains of Bacillus anthracis and potential surrogates. J. Food Prot. 2005;68:2362–6.

10. Gorman SP, Scott EM, Hutchinson EP. Effects of aqueous and alcoholic povidone-iodine on spores of Bacillus subtilis. J. Appl. Bacteriol. 1985;59:99–105.

11. Bloomfield SF, Megid R. Interaction of iodine with Bacillus subtilis spores and spore forms. J. Appl. Bacteriol. 1994;76:492–9.

12. Gershenfeld L, Witlin B. Iodine solution as a sporicidal agent. J. Am. Pharm. Assoc. Am. Pharm. Assoc. (Baltim). 1952;41:451–2.

13. Weihs TP. Fabrication and characterization of reactive multilayer films and foils. In: Barmak K, Coffey KR, editors. Met. Film. Electron. Opt. Magn. Appl. Swaston, UK: Woodhead; 2014. p. 160–243.

14. Adams DP. Reactive multilayers fabricated by vapor deposition: A critical review. Thin Solid Films. Elsevier B.V.; 2015;576:98–128.

15. Weihs TP, Barbee TWJ, Wall MA. Measuring Enthalpies of Formation Using Thick Multilayer Foils and Differential Scanning Calorimetry. MRS Proc. 1995;382:21–6.

16. Zumdahl SS. Chemical Principles. 6th ed. Houghton Mifflin Company; 2009.

17. Joress H, Barron S, Livi KJT, Aronhime N, Weihs TP. Self-sustaining oxidation initiated by rapid formation reactions in multilayer foils. Appl. Phys. Lett. 2012;101:111908.

18. Rogachev AS. Exothermic reaction waves in multilayer nanofilms. Russ. Chem. Rev. 2008;77:21–37.

19. Prakash A, McCormick A V., Zachariah MR. Tuning the reactivity of energetic nanoparticles by creation of a core-shell nanostructure. Nano Lett. 2005;5:1357–60.

20. Sundaram DS, Yang V. Effect of packing density on flame propagation of nickel-coated aluminum particles. Combust. Flame. The Combustion Institute.; 2014;161:2916–23.

21. Feng J, Jian G, Liu Q, Zachariah MR. Passivated iodine pentoxide oxidizer for potential biocidal nanoenergetic applications. ACS Appl. Mater. Interfaces. 2013;5:8875–80.

22. Levchenko E V., Evteev A V., Riley DP, Belova I V., Murch GE. Molecular dynamics simulation of the alloying reaction in Al-coated Ni nanoparticle. Comput. Mater. Sci. Elsevier B.V.; 2010;47:712–20.

23. White JDE, Reeves R V, Son SF, Mukasyan AS. Thermal explosion in Al-Ni system: influence of mechanical activation. J. Phys. Chem. A. 2009;113:13541–7.

24. Yan S, Jian G, Zachariah MR. Electrospun Nano fi ber-Based Thermite Textiles and their Reactive Properties. ACS Appl. Mater. Interfaces. 2012;4:6432–5.

25. Sullivan KT, Piekiel NW, Chowdhury S, Wu C, Zachariah MR, Johnson CE. Ignition and Combustion Characteristics of Nanoscale Al/AgIO 3 : A Potential Energetic Biocidal System. Combust. Sci. Technol. 2010;183:285–302.

26. Dean SW, Potter JK, Yetter R a., Eden TJ, Champagne V, Trexler M. Energetic intermetallic materials formed by cold spray. Intermetallics. Elsevier Ltd; 2013;43:121–30.

27. Li HP, Sekhar J a. The influence of the reactant size on the micropyretic synthesis of NiAl intermetallic compounds. J. Mater. Res. 1995;10:2471–80.

28. Dong S, Hou P, Yang H, Zou G. Synthesis of intermetallic NiAl by SHS reaction using coarse-grained nickel and ultrafine-grained aluminum produced by wire electrical explosion. Intermetallics. 2002;10:217–23.

29. Hunt EM, Pantoya ML. Ignition dynamics and activation energies of metallic thermites: From nano- to micron-scale particulate composites. J. Appl. Phys. 2005;98:034909.

30. Benjamin JS. Mechanical alloying — A perspective. Met. Powder Rep. MPR Publishing Services Ltd.; 1990;45:122–7.

31. Lu L, Zhang YF. Influence of process control agent on interdiffusion between Al and Mg during mechanical alloying. J. Alloys Compd. 1999;290:279–83.

32. Wen CE, Kobayashi K, Sugiyama T, Nishio T, Matsumoto A. Synthesis of nanocrystallite by mechanical alloying and in situ observation of their combustion phase transformation in Al3Ti. J. Mater. Sci. 2000;35:2099–105.

33. Stover AK, Krywopusk NM, Fritz GM, Barron SC, Gibbins JD, Weihs TP. An analysis of the microstructure and properties of cold-rolled Ni:Al laminate foils. J. Mater. Sci. 2013;48:5917–29.

34. Rogachev AS, Shkodich NF, Vadchenko SG, Baras F, Kovalev DY, Rouvimov S, et al. Influence of the high energy ball milling on structure and reactivity of the Ni+Al powder mixture. J. Alloys Compd. Elsevier B.V.; 2013;577:600–5.

35. Weihs TP. Self-propagating reactions in multilayer materials. In: Glocker D, Shah S, editors. Handb. Thin Film Process Technol. Bristol, UK: IOP Publishing Ltd; 1997.

36. Ma E, Thompson C V., Clevenger LA, Tu KN. Self-propagating explosive reactions in Al/Ni multilayer thin films. Appl. Phys. Lett. 1990;57:1262–4.

37. Adams DP, Rodriguez MA, McDonald JP, Bai MM, Jones E, Brewer L, et al. Reactive Ni/Ti nanolaminates. J. Appl. Phys. 2009;106:093505.

38. Knepper R, Snyder MR, Fritz G, Fisher K, Knio OM, Weihs TP. Effect of varying bilayer spacing distribution on reaction heat and velocity in reactive Al/Ni multilayers. J. Appl. Phys. 2009;105:083504.

39. Morris CJ, Mary B, Zakar E, Barron S, Fritz G, Knio O, et al. Rapid initiation of reactions in Al/Ni multilayers with nanoscale layering. J. Phys. Chem. Solids. Elsevier; 2010;71:84–9.

40. Barron S, Knepper R, Walker N, Weihs TP. Characterization of self-propagating formation reactions in Ni/Zr multilayered foils using reaction heats, velocities, and temperature-time profiles. J. Appl. Phys. 2011;109:013519.

41. Fisher K, Barron SC, Bonds M a., Knepper R, Livi KJT, Campbell GH, et al. Phase transformations, heat evolution, and atomic diffusion during slow heating of Al-rich Al/Zr multilayered foils. J. Appl. Phys. 2013;114:243509.

42. Barron SC, Kelly ST, Kirchhoff J, Knepper R, Fisher K, Livi KJT, et al. Self-propagating reactions in Al/Zr multilayers: Anomalous dependence of reaction velocity on bilayer thickness. J. Appl. Phys. 2013;114:223517.

43. Overdeep KR, Livi KJT, Allen DJ, Glumac NG, Weihs TP. Using Magnesium to Maximize Heat Generated by Reactive Al/Zr Nanolaminates. Combust. Flame. 2015;162:2855–65.

44. Overdeep KR, Weihs TP. Design and functionality of a high-sensitivity bomb calorimeter specialized for reactive metallic foils. J. Therm. Anal. Calorim. Springer Netherlands; 2015;122:787–94.

45. Overdeep KR, Joress H, Zhou L, Livi KJT, Barron SC, Grapes MD, et al. Mechanisms of Oxide Growth During the Combustion of Al:Zr Nanolaminate Foils. To be Submitt. 2016;

46. Overdeep K, Schmauss T, Panigrahi A, Weihs TP. Combustion of reactive Al/Zr nanolaminates: the influence of foil geometry. To be Submitt. 2016;

47. Jiang X, Overdeep KR, Weihs TP, Mao H-Q. Effect of Humidity on Sporicidal Activity of Iodine Vapor on Bacillus Thuringiensis. To be Submitt. 2016;

48. Vohra M, Winokur J, Overdeep KR, Marcello P, Weihs TP, Knio OM. Development of a reduced model of formation reactions in Zr-Al nanolaminates. J. Appl. Phys. 2014;116:233501.

49. Korchagina EN, Ermakova EV, Belyakov VI. A comparative analysis of the technical and metrological characteristics of bomb calorimeters used in Russia. Meas. Tech. 2011;54:186–93.

50. Nagano Y, Sugimoto T. MICRO-COMBUSTION CALORIMETRY AIMING AT 1 mg SAMPLES. J. Therm. Anal. Calorim. 1999;57:867–74.

51. McEwan WS, Anderson CM. Miniature Bomb Calorimeter for the Determination of Heats of Combustion of Samples of the Order of 50 mg Mass. Rev. Sci. Instrum. 1955;26:280.

52. Ribeiro da Silva MAV, Pilcher G, Santos LMNBF, Lima LMSS. Calibration and test of an aneroid mini-bomb combustion calorimeter. J. Chem. Thermodyn. 2007;39:689–97.

53. Mentado J, Mendoza E. Calibration and testing of an isoperibolic micro-combustion calorimeter developed to measure the enthalpy of combustion of

organic compounds containing C, H, O and N. J. Chem. Thermodyn. 2013;59:209–13.

54. Rojas-Aguilar A. An isoperibol micro-bomb combustion calorimeter for measurement of the enthalpy of combustion. Application to the study of fullerene C60. J. Chem. Thermodyn. 2002;34:1729–43.

55. Sakiyama M, Kiyobayashi T. Micro-bomb combustion calorimeter equipped with an electric heater for aiding complete combustion. J. Chem. Thermodyn. 2000;32:269–79.

56. Camarillo EA, Flores H. Construction, calibration and testing of a micro-combustion calorimeter. J. Chem. Thermodyn. 2006;38:1269–73.

57. Diogo HP, Minas ME. A micro-combustion calorimeter suitable for samples of mass 10 mg to 50 mg. Application to solid compounds of C , H , and O , and of C , H , O , and N. J. Chem. Thermodyn. 1995;27:197–206.

58. Månsson M. A 4 . 5 cm 3 bomb combustion calorimeter and an ampoule technique for 5 to 10 mg samples with vapour pressures below approximately 3 kPa (20 Torr). J. Chem. Thermodyn. 1973;5:721–32.

59. Metzger RM, Kuo CS, Arafat ES. A semi-micro rotating-bomb combustion calorimeter. J. Chem. Thermodyn. 1983;15:841–51.

60. Parker W, Steele W V, Stirling W. A high-precision aneroid static-born combustion calorimeter for samples about 20 mg . The standard enthalpy formation of bicylco[3.3.3]undecane. J. Chem. Thermodyn. 1975;7:795–802.

61. Byrne PG, Dempsey T, Marchandise H, Vandendriessche S. Report EUR 14439 E.N. Determination of the Gross Calorific Value of natural gas: Results of a BCR Intercomparison. Brussels: Commission on the European Communities; 1993.

62. Korchagina EN. Thermal measurements- Present State and Trends in the Development of Combustion Calorimetry. Meas. Tech. 1999;41:49–54.

63. Nathani H, Wang J, Weihs TP. Long-term stability of nanostructured systems with negative heats of mixing. J. Appl. Phys. 2007;101:104315.

64. Washburn EW. Standard States for bomb Calorimetry. Bur. Stand. J. Res. National Bureau of Standards; 1933;10:525–58.

65. Wen J. Heat Capacities of Polymers. In: Mark JE, editor. Phys. Prop. Polym. Handb. 2nd ed. Springer; 2007. p. 152.

66. Wagner W, Pruß A. The IAPWS Formulation 1995 for the Thermodynamic Properties of Ordinary Water Substance for General and Scientific Use. J. Phys. Chem. Ref. Data. 2002;31:387.

67. Hajiev SN. A Highly Sensitive Dynamic Bomb Calorimeter. Rev. Sci. Instrum. 1970;41:68.

68. Recknagel RO, Glende E a, Dolak J a, Waller RL. Mechanisms of carbon tetrachloride toxicity. Pharmacol. Ther. 1989;43:139–54.

69. Benjamin D. Metals Handbook Volume 2: Properties and Selection: Nonferrous Alloys and Pure Metals. 9th ed. ASM Handbook Committee, editor. Metals Park, Ohio: American Society for Metals; 1980.

70. Benjamin D. Metals Handbook Volume 3: Properties and Selection: Stainless Steels, Tool Materials and Special-Purpose Metals. 9th ed. Committee AH, editor. Metals Park, Ohio: American Society for Metals; 1980.

71. Schweitzer PA. Corrosion Resistance Tables. 3rd ed. New York, NY: Marcel Dekker, Inc.; 1991.

72. Dickinson HJ. Combustion Bomb Calorimetry and the Heats of Combustion of Cane Sugar, Benzoic Acid, and Napthalene. Bull. Bur. Stand. 1914;11:244.

73. Wang J, Besnoin E, Knio OM, Weihs TP. Effects of physical properties of components on reactive nanolayer joining. J. Appl. Phys. 2005;97:114307.

74. Kuk SW, Ryu HJ, Yu J. Effects of the Al/Ni ratio on the reactions in the compression-bonded Ni-sputtered Al foil multilayer. J. Alloys Compd. Elsevier B.V.; 2013;589:455–61.

75. Fritz GM. Thesis. Johns Hopkins University; 2011.

76. Gavens AJ, Van Heerden D, Mann AB, Reiss ME, Weihs TP. Effect of intermixing on self-propagating exothermic reactions in Al/Ni nanolaminate foils. J. Appl. Phys. 2000;87:1255.

77. Swaminathan P, Grapes MD, Woll K, Barron SC, LaVan D a., Weihs TP. Studying exothermic reactions in the Ni-Al system at rapid heating rates using a nanocalorimeter. J. Appl. Phys. 2013;113:143509.

78. Santos LMNBF, Silva MT, Schröder B, Gomes L. Labtermo: Methodologies for the calculation of the corrected temperature rise in isoperibol calorimetry. J. Therm. Anal. Calorim. 2007;89:175–80.

79. Conkling JA. Chemistry of Pyrotechnics: Basic Principles and Theory. New York, NY: Marcel Dekker, Inc.; 1985.

80. Schoenitz M, Dreizin EL. Oxidation Processes and Phase Changes in Metastable Al-Mg Alloys. J. Propuls. Power. 2004;20:1064–8.

81. Haynes WM. CRC Handbook of Chemistry and Physics. 92nd ed. Boca Raton, FL: CRC Press; 2011.

82. Popov EI, Kashporov LY, Mal'tsev VM, Breiter AL. Combustion mechanism of aluminum-magnesium alloy particles. Combust. Explos. Shock Waves. 1973;9:204–8.

83. Aly Y, Schoenitz M, Dreizin EL. Ignition and combustion of mechanically alloyed Al–Mg powders with customized particle sizes. Combust. Flame. 2013;160:835–42.

84. Aly Y, Hoffman VK, Schoenitz M, Dreizin EL. Reactive, Mechanically Alloyed Al·Mg Powders with Customized Particle Sizes and Compositions. J. Propuls. Power. 2014;30:96–104.

85. Aly Y, Dreizin EL. Ignition and combustion of Al·Mg alloy powders prepared by different techniques. Combust. Flame. The Combustion Institute; 2015;162:1440–7.

86. Corcoran AL, Wang S, Aly Y, Dreizin EL. Combustion of Mechanically Alloyed Al·Mg Powders in Products of a Hydrocarbon Flame. Combust. Sci. Technol. 2014;187:807–25.

87. Müller B, Renz U. Development of a fast fiber-optic two-color pyrometer for the temperature measurement of surfaces with varying emissivities. Rev. Sci. Instrum. 2001;72:3366–74.

88. Zhong Y, Yang M, Liu Z-K. Contribution of first-principles energetics to Al–Mg thermodynamic modeling. Calphad Comput. Coupling Phase Diagrams Thermochem. 2005;29:303–11.

89. Okamoto H. Al-Zr (Aluminum-Zirconium). J. Phase Equilibria. 2002;23:455–6.

90. Okamoto H. Mg-Zr (Magnesium-Zirconium). J. Phase Equilibria Diffus. 2007;28:305–6.

91. Linstrom PJ, Mallard WG. NIST Chemistry WebBook [Internet]. NIST Stand. Ref. Database 69. 2011.

92. de Boer FR, Boom R, Mattens WCM, Miedema AR, Niessen AK. Cohesion in Metals: Transition Metal Alloys. Amsterdam: Elsevier Science Publishers B.V.; 1989.

93. Pickering JC, Thorne AP, Webb JK. Precise laboratory wavelengths of the Mg I and Mg II resonance transitions at 2853, 2803 and 2796 A. Mon. Not. R. Astron. Soc. 1998;300:131–4.

94. Mahanti PC. The Band Syectra of MgO, CaO and SrO. Phys. Rev. 1932;42:609–24.

95. Brewer L, Trajmar S. Ultraviolet Bands of Magnesium Hydroxide and Oxide. J. Chem. Phys. 1962;36:1585–7.

96. Pomeroy WC. The Quantum Analysis of the Band Spectrum of Aluminum Oxide. Phys. Rev. 1927;29:59–79.

97. Kunz M, Klingshirn C, Kretschmann H, Assmus W. Absorption and Emission Spectra of Magnesium Oxide Single Crystals. Mater. Chem. Phys. 1990;25:27–41.

98. Lowater F. The band spectrum of zirconium oxide. Proc. Phys. Soc. 1932;44:51–66.

99. Honig RE. Vapor Pressure Data for the More Common Elements. RCA Rev. 1957;18:195.

100. Nelson LS. Nature of the Spearpoints observed during the Combustion of Zirconium Droplets. Nature. 1965;207:741.

101. Meyer RT, Nelson LS. The Role of Nitrogen in the Formation of Microbubbles During the Explosive Combustion of Zirconium Droplets in N2/O2 Mixtures. High Temp. Sci. 1970;2:35–57.

102. Molodetsky IE, Dreizin EL, Law CK. Evolution of particle temperature and internal composition for zirconium burning in air. Symp. Combust. 1996;26:1919–27.

103. Dreizin EL. Phase changes in metal combustion. Prog. Energy Combust. Sci. 2000;26:57–78.

104. Fischer GR, Manfredo LJ, McNally RN, Doman RC. The eutectic and liquidus in the Al2O3-Zr02 system. J. Mater. Sci. 1981;16:3447–51.

105. Zavodinsky VG. The mechanism of ionic conductivity in stabilized cubic zirconia. Phys. Solid State. 2004;46:453–7.

106. Kwak H, Chaudhuri S. Role of vacancy and metal doping on combustive oxidation of Zr/ZrO2 core-shell particles. Surf. Sci. Elsevier B.V.; 2010;604:2116–28.

107. Czerwinski F. The oxidation behaviour of an AZ91D magnesium alloy at high temperatures. Acta Mater. 2002;50:2639–54.

108. Paljevic M. High-temperature oxidation behaviour in the Zr-A1 system. J. Alloys Compd. 1994;204:119–26.

109. Mackenzie FT. Our Changing Planet. Upper Saddle River, NJ: Prentice-Hall; 1995.

110. Williams GP. A general review of synchrotron radiation, its uses and special technologies. Vacuum. 1982;32:333–45.

111. Bilderback DH, Elleaume P, Weckert E. Review of third and next generation synchrotron light sources. J. Phys. B At. Mol. Opt. Phys. 2005;38:S773–97.

112. Kelly ST, Trenkle JC, Koerner LJ, Barron SC, Walker N, Pouliquen PO, et al. Fast X-ray microdiffraction techniques for studying irreversible transformations in materials. J. Synchrotron Radiat. International Union of Crystallography; 2011;18:464–74.

113. Vohra M, Weihs TP, Knio OM. A simplified computational model of the oxidation of Zr/Al multilayers. Combust. Flame. The Combustion Institute; 2014;162:249–57.

114. Paljevic M. High-temperature oxidation behaviour in the Zr-Al system. J. Alloys Compd. 1994;204:119–26.

115. Fritz GM, Grzyb J a., Knio OM, Grapes MD, Weihs TP. Characterizing solid-state ignition of runaway chemical reactions in Ni-Al nanoscale multilayers under uniform heating. J. Appl. Phys. 2015;118:135101.

116. Santos PS, Santos HS, Toledo SP. Standard transition aluminas. Electron microscopy studies. Mater. Res. 2000;3:104–14.

117. Shirai T, Watanabe H, Fuji M, Takahashi M. Structural properties and surface characteristics on aluminium oxide powders. Annu. Rep. Ceram. Res. Lab. Nagoya Inst. Technol. 2009;9:23–31.

118. Wilson CG, Spooner FJ. The crystal structure of Zr3Al2. Acta Crystallogr. 1960;13:358–9.

119. Nandedkar R, Delavignette P. On the Formation of a New Superstructure in the Zirconium-Aluminium System. Phys. Status Solidi. 1982;73:K157–60.

120. Paljevic M. Non-selective oxidation of ZrAl3. J. Less-Common Met. 1991;175:289–94.

121. Paljevic M. CHANGE OF OXIDATION KINETICS IN THE Zr-Al SYSTEM. J. Less-Common Met. 1990;157:289–93.

122. Paljevic M. High-Temperature Oxidation of ZrAl. J. Less-Common Met. 1988;138:107–11.

123. Paljevic M. Interaction of Zr2Al with oxygen at high temperatures. J. Less-Common Met. 1986;120:293–9.

124. Paljevic M, Ban Z. Selective oxidation of zirconium in Zr3Al. J. Less-Common Met. 1985;105:83–6.

125. Paljevic M, Ban Z. Comparison of the oxidation behaviour of α-Zr-Al and Zr3Al. J. Less-Common Met. 1983;95:105–13.

126. Paljevic M, Ban Z. Oxidation of stoichiometric Zr3Al-based alloy. J. Nucl. Mater. 1980;95:253–8.

127. Pawel RE, Campbell JJ. The Oxidation of Pure Zirconium in Steam from 1000° to 1416°C. J. Electrochem. Soc. 1981;128:1999–2005.

128. Arimondi M. Chemical Mechanism of the Zr+ O2→ ZrO2 Combustion Synthesis Reaction. J. …. 1997;5647:8059–68.

129. Wang T. Thermodynamic assessment of the ZrO 2-AlO 1.5 system. J. Cent. South Univ. Technol. 1997;4:8–12.

130. Heuer AH. Oxygen and aluminum diffusion in α-Al2O3: How much do we really understand? J. Eur. Ceram. Soc. 2008;28:1495–507.

131. Friedman R, Maček a. Ignition and combustion of aluminium particles in hot ambient gases. Combust. Flame. 1962;6:9–19.

132. Huang Y, Risha G a., Yang V, Yetter R a. Effect of particle size on combustion of aluminum particle dust in air. Combust. Flame. Elsevier Inc.; 2009;156:5–13.

133. Beckstead MW. Correlating aluminum burning times. Combust. Explos. Shock Waves. 2005;41:533–46.

134. Gill RJ, Mohan S, Dreizin EL. Sizing and burn time measurements of micron-sized metal powders. Rev. Sci. Instrum. 2009;80.

135. Wei H, Yoo CS. Kinetics of small single particle combustion of zirconium alloy. J. Appl. Phys. 2012;111.

136. Ermoline A, Yildiz D, Dreizin EL. Model of heterogeneous combustion of small particles. Combust. Flame. The Combustion Institute.; 2013;160:2982–9.

137. De Gonzalez CO, Garcia EA. Determination of the diffusion coefficients of oxygen in zirconium by means of XPS. Appl. Surf. Sci. 1990;44:211–9.

138. Anttila A, Raisanen J, Keinonen J. Diffusion of nitrogen in alpha-Zr and alpha-Hf. J. Less-Common Met. 1984;96:257–62.

139. Ruiz DH, Gribaudo LM, Monti AM. Self-diffusion in the hexagonal structure of Zirconium and Hafnium: computer simulation studies. Mater. Res. 2005;8:431–4.

140. Antonini M, Bortolani V. The vacancy formation energy for zirconium. J. Nucl. Mater. 1974;54:259–64.

141. Tzanetakis P, Hillairet J, Revel G. The formation energy of vacancies in aluminum and magnesium. Phys. Status Solidi. 1976;75:433–9.

142. Kidson GV. On the anomalous self-diffusion in body-centered cubic zirconium. Can. J. Phys. 1963;41:1563–70.

143. Yanagida H, Kroger FA. The system Al-O. J. Am. Chem. Soc. 1968;54:700–6.

144. Hillert M, Jonsson S. An Assessment of the Al-Fe-N System. Metall. Trans. A. 1992;23:3141–9.

145. Wang C, Zinkevich M, Aldinger F. On the thermodynamic modeling of the Zr-O system. Calphad Comput. Coupling Phase Diagrams Thermochem. 2004;28:281–92.

146. Wang WE, Olander DR. Computational thermodynamics of the ZrN system. J. Alloys Compd. 1995;224:153–8.

147. Molodetsky IE. High-Temperature Oxygen Dissolution in Liquid Zirconium. Mat. Res. Soc. Symp. Proc. 1996;418:195–200.

148. Gal'braikh EI, Kulik OP, Kuznetsov AA, Lyutaya MD. Enthalpy of formation of the nitrogen solid solution in α-zirconium and of zirconium nitride in their homogeneity regions. Sov. Powder Metall. Met. Ceram. 1970;9:748–51.

149. Yetter RA, Risha GA, Son SF. Metal particle combustion and nanotechnology. Proc. Combust. Inst. The Combustion Institute; 2009;32 II:1819–38.

150. Fritz G, Joress H, Weihs TP. Enabling and controlling slow reaction velocities in low-density compacts of multilayer reactive particles. Combust. Flame. The Combustion Institute.; 2011;158:1084–8.

151. Saunders N. A Review and Thermodynamic Assessment of the Al-Mg and Mg-Li systems. Calphad. 1990;14:61–70.

152. Overdeep KR, Weihs TP. Designing a High-Sensitivity Bomb Calorimeter Specialized for Reactive Foils. J. Therm. Anal. Calorimetry- To be Submitt. 2015.

10 Curriculum Vitae

Kyle Overdeep was born in Providence, Rhode Island on September 25, 1989. He conducted his undergraduate studies at the College of William and Mary in Williamsburg, VA. While there, he majored in Chemistry and minored in Applied Science. He worked in polymer lab during his Junior and Senior years, and wrote a Senior Honors Thesis on his research, specifically on the accelerated aging of polyamides in environments that this material is exposed to during off-shore oil pumping. He received his Bachelor's degree with Honors in Chemistry in 2011, and moved directly into the PhD program in Materials Science and Engineering at Johns Hopkins University. There he conducted research on reactive metal nanocomposites under his advisor, Timothy Weihs.